Visual Neuroanatomy of Large-Brained Primates and Carnivores

By

Emily C. Turner

Dissertation
Submitted to the Faculty of the
Graduate School of Vanderbilt University
in partial fulfillment of the requirements
for the degree of

DOCTOR OF PHILOSOPHY
in

Psychology
May, 2017
Nashville, Tennessee

Approved:

Jon H. Kaas, Ph.D.

Troy A. Hackett, Ph.D.

Anita A. Disney, Ph.D.

Isabel Gauthier, Ph.D.

To my husband, Ryan, and my best canine pals, Darwin and Marlee

ACKNOWLEDGMENTS

I am especially grateful to Dr. Jon H. Kaas, Distinguished Centennial Professor of Psychology, who has been consistently supportive of my career goals across the past five years. I first met Jon during my graduate school interview on February 14th, 2012, and my first impression of him at the Mellow Mushroom was him frantically leaving within an hour in order to take Barbara out to dinner because he forgot it was Valentine's Day. As my mentor, he has taught me what good science is, and how rare it sometimes is. As a friend, he has taught me to never put an anesthetized lion in a car trunk. I'm very thankful for the freedom Jon has given me to pursue my own research interests, and trusting me to stay productive even though I've been hidden away on the 4th floor of Wilson Hall for five years in a private office.

I am indebted to each of the members of my dissertation committee, Dr. Troy Hackett, Dr. Anita Disney, and Dr. Isabel Gauthier, for guiding my research at our yearly checkpoints and allowing me the opportunity to stay true to my scientific passions. I also want to thank Dr. Vivien Casagrande for her two years of service on my committee, and for co-sponsoring me as a graduate student when I first came to Vanderbilt even though I ultimately decided to join the Kaas lab. I admit I did not join her lab only because she kept excitedly talking about the pulvinar like it was the greatest thing in the world and I had no idea what that was – I will be sure to include architectonic features of the pulvinar in my upcoming galago development paper in her honor. I'd also like to thank Dr. Ram Ramachandran who served on my committee during my qualifying exam. I thank each of them very much for all their insightful efforts to make me a better researcher.

I would like to thank the current and former members of the Kaas lab for their assistance and great friendships. Firstly, I would not exist at Vanderbilt without our lab manager Laura Trice, even though after a few decades here she refuses to give herself that title. She has kept me on my toes, and helped me cut and process thousands and thousands of brain sections, most of which ultimately end up unused and discarded. I have dropped dozens of glass beakers and spilled dangerous chemicals, and Laura always knows what to do. Pooja Balaram took me under her wing during my first year of graduate school, and taught me everything she knows about neuroscience and immunohistochemistry. With her help, I managed to get out my first publication in less than a year at Vanderbilt. I appreciate her endless help, as I can recall sending her frantic e-mails, texts, and phone calls at all hours of the day asking her questions I'd already asked ten times over. Yet, she remained patient. Nicole Young was also a fantastic mentor in the two years we overlapped, and I still enjoy our conversations, as she always has a great opinion about everything going on in the lab. I thank her for her career guidance especially in the past few years. Jamie Reed is a statistical goddess and my papers would have less content without her knowledge. Thanks to Jamie I have not touched a statistical software program in five years, but I'll learn someday. Iwona Stepniewska and Hui-Xin Qi have taught me many things about electrophysiology, and I have learned so much from each of them individually. Lastly, even though our research projects only overlapped slightly over the course of several years, Mariana Gabi and Chia-Chi Liao have been amazing friends and wine pals. I'm also indebted to Mary Feurtado, who has helped immensely in the coordination and planning of my developmental galago project, and Dr. Troy Apple for his veterinary advice and wisdom, and for keeping me calm when I had a Herpes B exposure (I turned out fine).

This work would not have taken place without the financial support of the Vanderbilt University Department of Psychological Sciences, for supporting me with a graduate teaching assistantship for four years. I enjoyed learning from Dr. Elisabeth Sandberg and Dr. Isabel Gauthier among many others in the five combined semesters I've spent working with each, and watching their exceptional teaching styles has improved my public speaking and science communication.

Lastly, my husband, Ryan, deserves a special mention. I never had doubts or regrets about graduate school like many of my peers because moving to Nashville led me to meet my better half. Graduate school has been a breeze with him by my side, and I appreciate the happiness he brings me every single moment of every single day.

TABLE OF CONTENTS

Page

LIST OF TABLES

LIST OF FIGURES

LIST OF ABBREVIATIONS

A-P	Anterior to Posterior
Area 1	Caudal Cutaneous Somatosensory Area in Anterior Parietal Cortex
Area 2	Caudal Proprioceptive Area in Anterior Parietal Cortex
Area 3a	Rostral Proprioceptive Area in Anterior Parietal Cortex
Area 3b	Primary Somatosensory Area in Anterior Parietal Cortex (S1)
Area 17	Primary Visual Cortex (V1)
Area 18	Secondary Visual Cortex (V2)
AS	Ansate Sulcus
CBP	Calcium-Binding Protein
CO	Cytochrome Oxidase
CoS	Coronal Sulcus
CrS	Cruciate Sulcus
CSL	California Sea Lion
EcS	Ectolateral Sulcus
EsS	Ectosylvian Sulcus
EnS	Entolateral Sulcus
G/N	Glial Cell to Neuron Ratio
K	Koniocellular Pathway
lSGS	Lower Superficial Gray Layer
LGN	Lateral Geniculate Nucleus
LH	Left Hemisphere
LS	Lateral Sulcus
M	Magnocellular Class
M1	Primary Motor Cortex
MIN	Medial Interlaminar Layer
MT	Middle Temporal Area
N	Nissl
NES	Northern Elephant Seal
NeuN	Neuronal Nuclear Antigen
P	Parvocellular Class
PAG	Periaqueductal Gray
PB	Phosphate-Buffered
PGN	Perigeniculate Nucleus
PLS	Posterior Lateral Sulcus
PS	Pseudosylvian Sulcus
RH	Right Hemisphere
RS	Rhinal Sulcus
S1	Primary Somatosensory Cortex
SAI	Intermediate White Layer
SAP	Deep White Layer
SC	Superior Colliculus
SEM	Standard Error of the Mean
SGI	Intermediate Gray Layer
SGP	Deep Gray Layer

SGS	Superficial Gray Layer
SO	Optic Layer
SP	Splenial Sulcus
SuS	Suprasplenial Sulcus
SS	Suprasylvian Sulcus
SZ	Zonal Layer
uSGS	Upper Superficial Gray Layer
V1	Primary Visual Cortex
V2	Secondary Visual Cortex
VGluT1	Vesicular Glutamate Transporter 1
VGluT2	Vesicular Glutamate Transporter

CHAPTER 1

INTRODUCTION

Thesis objectives

This research is part of a larger effort to understand the evolution of the mammalian brain. The studies in Chapters 2 – 4 address questions regarding the evolution of the visual system in primates and other non-primate large-brained mammals. Pinnipeds are an ideal subject for comparison, as pinnipeds are a diverse clade of carnivorous animals and consist of three families: Odobenidae (walrus), Otariidae (eared seals: sea lions and fur seals), and Phocidae (earless seals: true seals). In this research, we examined the cortical and subcortical visual components of two pinniped species with large brains, the California sea lion (*Zalophus californianus*) and the northern elephant seal (*Mirounga angustirostris*).

To best examine how these species gained and require such large brains, it is important to simultaneously look to primate species that, independently of the pinniped lineage, came to also evolve large brains. As such, we examined the structure and components of the visual system in select primate species: a chimpanzee (*Pan troglodytes*) and macaques (*Macaca nemestrina, Macaca mulatta, and Macaca radiata*). Primates are notable for their large brains, and every primate species has an average brain size larger than then 0.4 g mouse brain, the animal model most commonly used in laboratory studies. Primate brains range considerably in size from 1.7 grams (mouse lemur) to over 1,300 grams (human), and share many common brain features despite species-specific specializations that develop across evolutionary history. These species

are chosen for two important reasons: 1) Each has a highly developed visual system, and 2) All are members of the same phylogenetic mammalian radiation known as the Euarchontoglires.

The primary goal of this research was to expand on our extensive knowledge of the primate visual system while also extending out to explore the visual system of under-studied species that similarly have large, complexly folded brains. A secondary goal of this research was to compare non-primates with large brains to primate brains, to ultimately emerge with a better understanding of how the visual system can evolve and function differently or similarly in the context of a large brain. The specific aims were to:

Aim 1) To use the isotropic and flow fractionator techniques to understand the basic neuron and cell content of various primate species (Chapters 2 and 3).

> Neurons are the building blocks of neocortex, and an accurate estimate of the total number of neurons in a brain can reveal information concerning the specializations of cortex. In this collaborative effort, we determined the total numbers of cells and neurons within the neocortex of the adult chimpanzee and macaque brains. These are species that have relatively large brains compared to most mammals, and to the proposed brain size of our earliest mammalian ancestors. This data was compared to previously reported results in similarly prepared species, such as the baboon and New World monkeys. We found the same pattern of overall neuronal density described in all other primate species, in which primary visual cortex and primary somatosensory cortex contain higher-than-average neuron densities and primary motor cortex contains lower-than-average neuron densities.

Aim 2) To describe the basic components of the visual systems of large-brained non-primate mammals (the California sea lion and northern elephant seal) (Chapter 4).

Given their highly gyrified neocortex, similar studies of cell and neuron counts are not possible in seals and sea lion brains easily using the same methodologies as per Aim 1. We previously described the neuroanatomy of the somatosensory system at the level of the midbrain, thalamus, and cortex in pinnipeds (Sawyer et al., 2016), and this represents the first effort to describe the neuroanatomy of the lateral geniculate nucleus, superior colliculus, and primary visual cortex in the northern elephant seal and California sea lion. We examined the visual neuroanatomy in these two species using immunohistochemistry in coronal sections and other reconstruction methods. We found that the visual neuroanatomy is more similar in structure to other carnivores, such as cats, as opposed to primates, which is expected given these species' phylogenetic position within the Carnivora order. This research will contribute to the small amount of neuroscientific research in pinnipeds, and we seek to encourage similar research in other pinniped species for comparative studies related to brain evolution.

The phylogeny of mammals

Efforts to understand the evolution of modern mammalian brains are undertaken through comparative studies of cortical organization. Here, we have used a comparative approach in studying multiple species to understand more about the organization of the visual system across different mammalian orders. More closely related species, that are within the same phylogenetic order or family, are expected to share more common brain features and consequently share more

behavioral and physiological properties (Kaas, 2002; Kaas, 2005; 2012). When a visual structure or specialization is present in a clade of related species, it can be assumed that an earlier distant common ancestor also had said characteristic. However, when only select members of a clade contain a specific visual characteristic it is more likely that said characteristic results from independent convergent evolution, as opposed to a feature of a common ancestor. By studying the brains of different mammals, both distantly and closely related, we can learn about the features of mammalian ancestors, as well as deduce features which evolved independently of that common ancestor. This comparative approach, in which here we examined the architectonic structure and neurochemical content of the visual system in different species, is useful for learning about the importance of brain features necessary for a behavior or function (Kaas, 2002; Kaas, 2012).

Mammals emerged as a distinct radiation approximately 200 million years ago, and there are over 3,500 extant species (Murphy et al., 2001; Springer and de Jong, 2001). These species are divided into six different superorders: Monotremes, Afrotheria, Laurasiatheria, Euarchontoglires, Xenarthra, and Marsupials (see Fig. 1.1 for overview). The species within these six major mammalian branches are thought to be descended from one common mammalian ancestor. Comparative studies of brain evolution often examine the primate lineage which emerged as a distinct evolutionary branch within the Euarchontoglires superorder approximately 80 million years ago. The most closely related mammals to humans are New World monkeys (e.g., squirrel monkeys, owl monkeys, marmosets), Old World monkeys (e.g., macaques and baboons), and apes (e.g., gorillas and chimpanzees). Primates are some of the most diverse mammals in terms of body size, ranging from the mouse lemur at a tiny 40 g to the male gorilla which can weigh up to 200,000 g. Comparative studies can be difficult given the variability in

body and brain size, but research in non-human primates has revealed partly how human brains have come to evolve such a remarkable brain.

Figure 1.1 **Phylogeny of living mammals**. Blue boxes indicate branching of the primate and carnivore clades. Red stars indicate lineages examined in Chapters 2-4. Adapted from Kaas (2004).

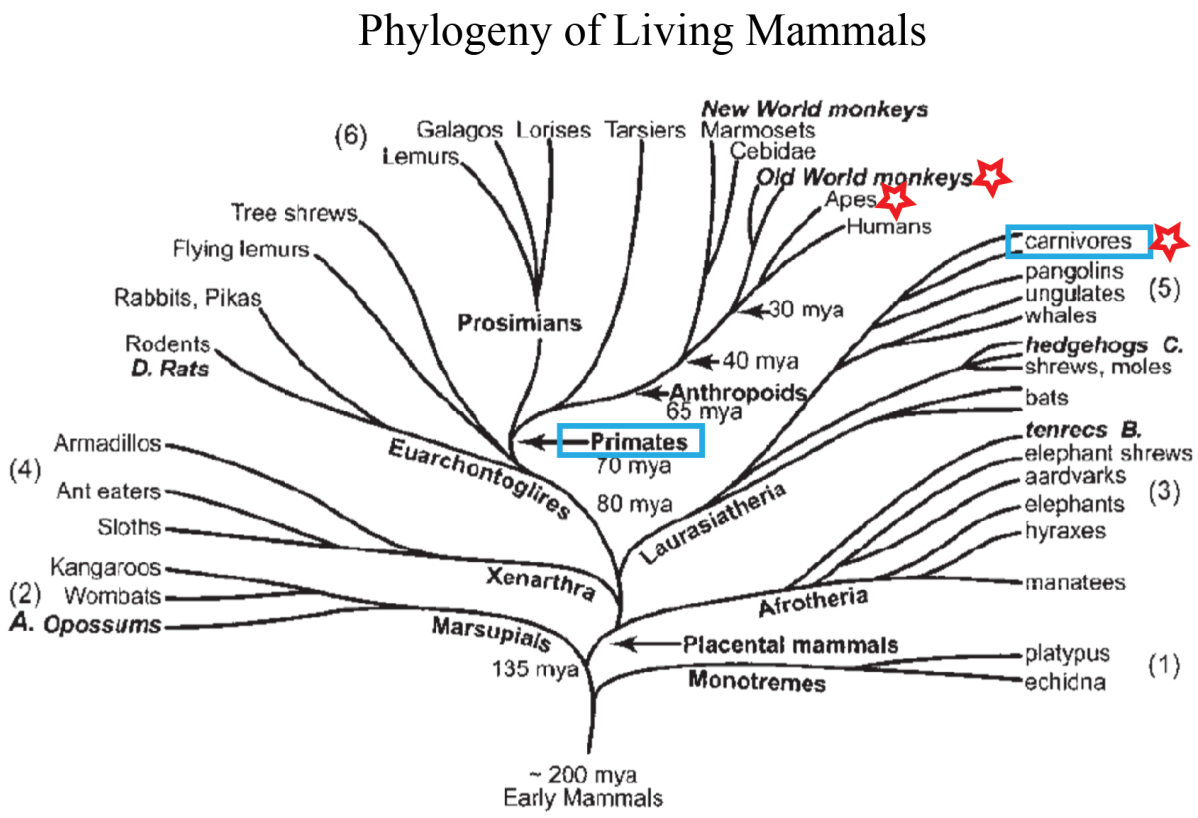

In 2010, there were at least 70,000 different non-human primates housed for use in biomedical research (Lankau et al., 2014). Chimpanzees are the best candidate in the pursuit of neuroscience research given their close phylogenetic relationship to humans, which is why in

Chapter 2 we focused on analyzing the neurochemical content of the chimpanzee brain. However, even our most closely related primate relative has an average brain weight over three times smaller (384 g) than that of a human (1,352 g) (Robson and Wood, 2008). Apart from differences in physical brain size, other considerations, such as behavioral and cognitive differences, present significant hurdles in finding a valid model of the human brain. Despite these differences, chimpanzees have the most neural similarities to humans, but current federal guidelines from the U.S. National Institutes of Health effectively prevent invasive research on chimpanzees. Therefore, any limited information that we can still gain from chimpanzees, such as determining the number of neurons and cells in their brains, can contribute to our understanding of our own human brain.

Macaque monkeys are a primate species commonly used in neuroscientific research, especially in areas related to neuropathology. For over 80 years these species have been used in research studying the neural mechanisms of cognition, in the hope of furthering our understanding of the cognitive mechanisms in the human brain (Jacobsen, 1936). The genus *Macaca* is separated from humans by over 30 million years of independent evolution, which raises the question of how applicable the scientific advances from macaque research are to humans (Passingham, 2009). In addition to an overall larger brain, humans have an increased number of specialized areas, in addition to differing proportions of neocortex dedicated to specialized regions. For example, humans have more visual areas than macaque monkeys, and our prefrontal cortex or granular frontal cortex occupies 28.5% of the human brain as opposed to 11.3% in macaques (Elston, 2007). In general, humans are also known to be more vulnerable than great apes in their susceptibility to aging diseases such as Alzheimer's and Parkinson disease, despite similar lifespans (Erwin and Hof, 2002).

However, despite significant differences between humans and macaques, these monkeys represent the most federally accessible and relatable primate species to humans available to researchers, thus explaining their widespread use in neuroscientific research. To maximize the clinical translatability of data gained through macaque research, a more thorough understanding of the differences and similarities between macaque species is necessary, which we addressed by analyzing the neurochemical content of different macaque species described in Chapter 3. There are arguably 20 to 23 extant macaque species, with very diverse ecological niches, and they are thought to have separated from other members of the Old World primate family, such as baboons, approximately 9 to 10 million years ago. Different ecological niches and diets contribute to differences in adaptive behaviors that emerge in response to specific environments, and these differences are often reflected in changes in brain structures that play a role in such behaviors (Krubitzer et al., 1995; Catania, 2011). Therefore, it is likely that we might see modifications even in the brains of closely related species that thrive in ever-so-slightly different environments. While there remains considerable debate regarding the classification of macaque species, Fooden (1976) was the first to classify macaques into four distinct species groups: fascicularis, silenus-sylvanus, sinica, and arctoides (Fig. 1.2). The three macaque species most commonly used in research as revealed through acquisition data are the crab-eating macaque (*Macaca fasicicularis*), rhesus macaque (*Macaca mulatta*), and the pig-tailed macaque *(Macaca nemestrina*) (Lankau et al., 2014). Yet, research often does not specify why a specific macaque species was used in research. It can be assumed that these choices are related to institutional housing capabilities or global guidelines related to the export and import of certain species, among other possible reasons. However, any insight regarding differences in the neocortical

structure of macaques will be useful in deciphering the applicability of research in these different species.

Figure 1.2 **Macaque phylogenetic relationships**. The phylogenetic relationship of the genus *Macaca* inferred using SINE-based methods reveals four distinct monophyletic species groups. Adapted from Li et al. (2009).

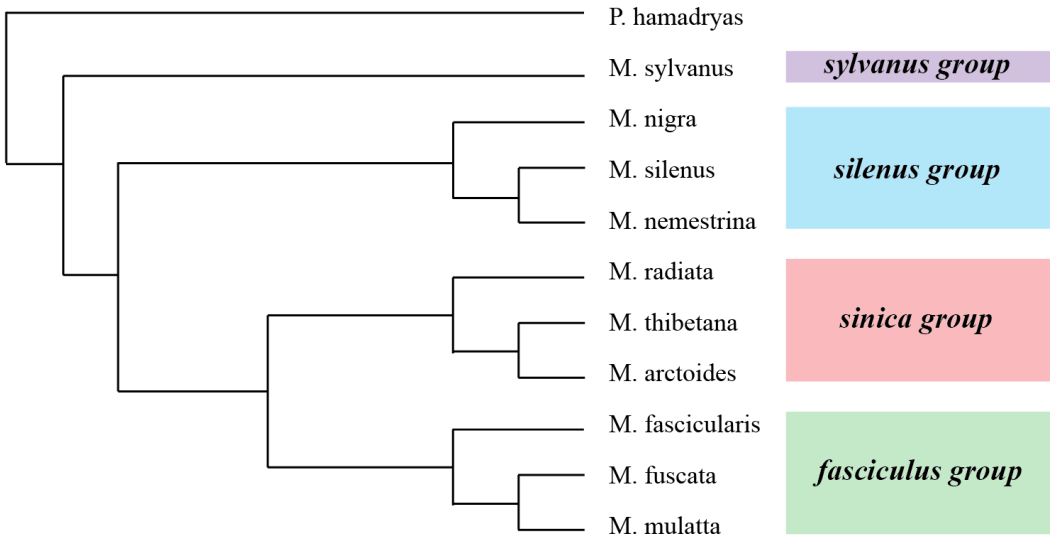

It is common to find mammals with brains larger than humans; the African bush elephant is one prominent example from the Afrotheria superorder, as this species' brain weighs over 2,800 g (Herculano-Houzel et al., 2014a). However, one superorder that contains many mammalian species with brains of notable size is Laurasiatheria, which diverged from Euarchontoglires approximately 90 to 100 million years ago. The Laurasiatheria superorder consists of diverse species, ranging from terrestrial lions and bears to aquatic whales, and many

of these mammals have, independently of the primate lineage, come to evolve brains equal to in size or larger than some primates. For example, within the Cetacean order, the sperm whale, gray whale and bowhead whale have brains weighing 7,800, 4,317 g, and 4,317 g, respectively (Berta et al., 2015). Within the Laurasiatheria superorder is the Carnivora order, whose members are known as "carnivorans," but may follow an omnivorous or carnivorous diet. The Carnivora order is perhaps the most diverse mammalian order in terms of brain and body size; the smallest mammal in this order is the least weasel, weighing in at 25 g, while the largest mammal is the southern elephant seal, whose weight has been recorded at over 5,000,000 g (Geptner et al., 1988; Hindell, 2002). There are approximately 270 extant species in Carnivora, and these species are diverse in that they occupy all seven continents and all types of habitats (Fig. 1.3). The mammals of interest for our specific research aims include a group of carnivorans known as pinnipeds, which consist of seals, sea lions, and walruses. There is only one extant species of walrus, in contrast to 18 seal species and 16 sea lion species. However, many of these seal and sea lion species, such as the Hawaiian monk seal, are on the brink of extinction; the Japanese sea lion is thought to become extinct in the 1970s when this species was last sighted (http://www.iucnredlist.org/). Other pinnipeds, such as the Mediterranean monk seal, are experiencing a critically dangerous population decline.

Carnivora is unofficially divided into two superfamilies, Caniformia (dog-like) and Feliformia (cat-like), and pinnipeds fall under the former category. Despite the diverse species types within this superfamily, most carnivoran vision research in this superfamily stems from dogs, ferrets, and raccoons. The closest living relatives of pinnipeds are members of the Ursidae or bear family, and while there are some reports on the visual pigments and capabilities of polar bears, black bears, and pandas (e.g., Levenson and Dizon (2003), Kelling et al. (2006)), most of

this research is limited and behaviorally-based, with few neuroanatomical studies. Domestic cats within the Caniformia superfamily represent our greatest source of knowledge regarding carnivoran vision, and while they are not particularly closely related to pinnipeds, it is likely that features of the carnivoran visual system are conserved across the Carnivora order.

Figure 1.3 **Phylogeny of carnivorans**. The order Carnivora tree was based on Agnarsson et al. (2010) and simplified to highlight relevant species that are most closely related to pinnipeds. The branching pattern indicates clades, but the branch length does not indicate phylogenetic distance. The three families (*Odobenidate, Otariidae,* and *Phocidae*) inside the blue box represent the Pinnipedia clade, and the species within each family listed underneath. The families inside the red boxes represent the families of carnivorans that are closely related to pinnipeds and have a well-studied visual system. The star represents the location of other carnivoran families in the cladogram, but they are not shown here since their visual systems are understudied.

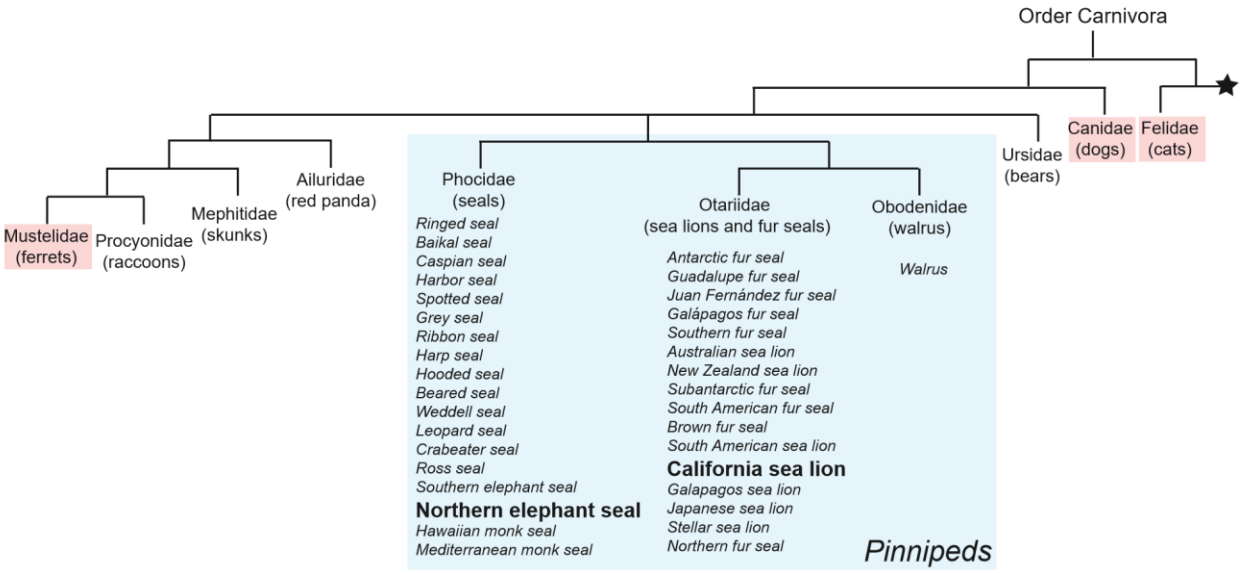

In the remaining sections of this chapter, I will provide a brief overview of two different methods that can be used to study the functional architecture and cortical connections of primary visual cortex.

Cell and neuronal density patterns in the mammalian brain

The cellular composition of the mammalian brain is critical to our understanding of the structures and function of neocortex. Nonuniformity in cell and neuron density suggests that different brain regions have different specialized functions, and as such there have been efforts over the past decade to quantify the absolute numbers of cells and neurons in dozens of species. These studies have been part of an ongoing effort to characterize how human brains are similar and different from non-human primates and other mammals. Similarly, this quantifiable approach of studying cells and neurons allows for a simple comparative measurement between species, a feat that is not easily accomplished given the large differences in brain structure across mammals.

The preferred method to quantify cells and neurons is with the isotropic fractionator method as described by Herculano-Houzel and Lent (2005). The isotropic fractionator is a simple and reliable method that works by homogenizing suspensions of cell nuclei which can then be counted immunocytochemically as a neuron or non-neuron. Alternatively, the flow fractionator method is a similar alternative which uses flow cytometry instead of microscopy to quantify the number of cells and neurons (Collins et al., 2010). Both techniques have been shown to produce results consistent with each other and with stereology (Bahney and von Bartheld, 2014; Miller et al., 2014), and thus have been used interchangeably over the past decade in cell counts research.

The diversity seen in the brain and body sizes of mammals begs the question of how the cellular content of the brain relates to a species' brain size. Brain size is not a proxy for the total number of neurons in the brain, as one might expect (Herculano-Houzel, 2011a; 2011b; 2012; Herculano-Houzel et al., 2014b). For example, the capybara and the macaque monkey have brains similar in size (76 g and 87 g, respectively), yet the number of neurons in the entire brain of the capybara is 1.6 million and the number of neurons in the macaque monkey is approximately 6.4 million (Herculano-Houzel et al., 2007). The scaling rules which guide brain growth and development can reveal how the numbers of neurons and non-neurons contribute to brain structure and size. The neuronal scaling rule of primates is different from that of non-primates, yet the relationship between brain mass and number of non-neuronal cells, such as glial cells, is shared across all mammalian orders (Herculano-Houzel et al., 2014b). Thus, determining the total number of neurons and non-neurons in mammalian species with similarly-sized brains to humans is a critical step towards understanding how certain brains came to be so large. If we can learn more about the cellular scaling rules which contribute to structure size, and the contributions of these cells within brains of different sizes, we might have a better understanding of what makes the human brain so special. The human brain is a linearly scaled up primate brain in many regards, such as in number of neurons and overall size (Azevedo et al., 2009; Herculano-Houzel, 2012). By making comparisons with other species with similarly-sized brains, it might be possible to explain how humans have a cognitive advantage. The cellular content and corresponding scaling rules in large pinniped brains have not yet been described, as the total number of cells and neurons in pinniped brains is still unknown.

In a comparison of non-human primates and pinnipeds, it would be most ideal to obtain the number of neurons and non-neurons in each species for a direct comparison. However,

certain obstacles exist for quantifying these number in pinniped brains. The preferred method of quantifying cells and neurons in neocortex, to maintain the boundaries of cortical regions, is by manually flattening the brain. The flattening of the cortical sheet preserves cortical regions in whole, and it is then possible to identify, separate, and quantify the neurochemical content of different regions to learn more about their functions. Cortical areas can be identified using electrophysiology or sulcal landmarks, in addition to primary sensory areas being easily identifiable by their myelin content. For example, primary sensory areas appear darker relative to surrounding tissue when placed on a light box because of their myelin-dense configuration. In species with less fissures, such as rodents or the prosimian galago, cortex is easily flattenable with forceps. But in species with larger brains that likely contain more fissures, such as macaques and chimpanzees, the flattening process is more difficult and more cuts are necessary to produce a flattened brain. This often results in a distorted brain, but it can still be useful in species such as primates where cortical areas have been well-documented so that regions can still be accurately identified. The brain weight of a chimpanzee is approximately 344 g, which is similar to that of the northern elephant seal (485 g) or California sea lion brain (284 g), so theoretically it is possible to flatten a pinniped brain if a chimpanzee brain can be flattened. Yet, the greater problem is that very little is known about the location of any brain regions in pinnipeds, as only a few studies have examined the brain architecture of any pinniped (Murie, 1874; Montie et al., 2009; Sawyer et al., 2016). It would be a difficult challenge to flatten such a brain without any knowledge of its structure or architecture, as the dissection should be performed along the boundaries of known cortical areas. Thus, our efforts in Chapter 4 are focused on identifying the cortical and subcortical architecture of pinniped brains. There exist simultaneous efforts to quantify the number of neurons and non-neurons in pinniped brains by

using coronal slices (Herculano-Houzel, unpublished), which will supplement the results of this research in the future.

Vesicular glutamate transporters: their role in feedforward visual projections

The mammalian visual system is a complex network of brains structures which continually process and relay visual information (Krubitzer and Kaas, 1989; Casagrande, 1994; Van Essen, 2005), and it is necessary to use markers to characterize the different types of cells in these pathways that might be morphologically identical and otherwise indistinguishable. The primary mode of excitatory neurotransmission in the central nervous system of mammals is through the release of glutamate, and vesicular glutamate transporters (VGluTs) are a family of transmembrane transport proteins that regulate the release of glutamate from synaptic vesicles in the axon terminals of glutamatergic neurons (Aihara et al., 2000; Bellocchio et al., 2000; Herzog et al., 2001; Kaneko et al., 2002; Hackett and de la Mothe, 2009). There are three known isoforms of VGluTs: VGluT1, VGluT2 and VGluT3. Two of these isoforms, VGluT1 and VGluT2, are widely expressed in the mammalian central nervous system and distinguish between distinct types of projections within the visual system, with largely complementary patterns (Herzog et al., 2001; Fremeau et al., 2004a).

Studies of VGluT1 and VGluT2 in different primate species show that each characterizes distinct types of glutamatergic synapses and regulates the glutamate release rate from synapses differently (Fremeau et al., 2004a; Fremeau et al., 2004b). Aside from their neurochemical differences, VGluT1 and VGluT2 are also characterized in different neuronal circuits; the evidence suggests that VGluT1 is predominantly distributed in feedback or modulatory

glutamatergic projections, in contrast to VGluT2 which is distributed in feedforward or driving projections in the visual system (Hackett and de la Mothe, 2009; Balaram et al., 2011a; Balaram et al., 2011b; Hackett et al., 2011; Balaram et al., 2013; Baldwin et al., 2013; Balaram et al., 2015). Most relevant to how these markers are used in the context of this research, the presence of VGluT1 and VGluT2 in different connections between visual structures may distinguish between thalamocortical and corticothalamic projections. VGluT2 is primarily used for thalamocortical projections, and thus is strongly expressed in primary sensory nuclei, such as the dorsal lateral geniculate nucleus (LGN). In galagos, for example, VGluT2 is strongly expressed in all six layers of the LGN and in the superficial layers of the superior colliculus (SC), which suggests that the retinogeniculate pathway utilizes VGluT2 for modulation of glutamatergic transmission since both the LGN and superficial layers of the SC are primary targets for retinal projections (Balaram et al., 2011b). Similarly, in the macaque monkey, the dense terminal labeling of VGluT2 in the four magnocellular (M) and two parvocellular (P) layers, but not the interlaminar layers, matches the pattern of retinogeniculate terminations described in macaques (Kaas et al., 1978). This consistent expression of VGluT2 described in all primates and rodents examined to date indicates that the retinogeniculate pathway primarily utilizes VGluT2 in its modulation of glutamatergic transmission.

There is also considerable evidence that the geniculocortical pathway to primary visual cortex similarly uses VGluT2 to modulate glutamatergic transmission. VGluT2 is strongly expressed in layer 4 of primary sensory areas in mice (Liguz-Lecznar and Skangiel-Kramska, 2007), primates (Balaram et al., 2011b; Balaram et al., 2013; Balaram et al., 2015), and ferrets (Nahmani and Erisir, 2005). More specifically, in macaques, there are dense VGluT2 terminations in layers 4A, 4B, and 3Bb which reflect the M and P inputs from the LGN, since

those layers of the LGN also contain strong *VGluT2* mRNA expression (Balaram et al., 2013). Ferrets, members of the Carnivora order, also express dense VGluT2 immunoreactivity in layer 4 primary visual cortex and less densely in layers 1 and 6 as early as postnatal day 27, suggesting that these thalamic projections to cortex use VGluT2 as a glutamate transporters in both early development and adulthood.

The LGN, SC, and primary visual cortex of pinnipeds have never been described. Using VGluT2 immunohistochemistry, the neuroanatomy of the visual system in two pinniped species is described in Chapter 4. Since both the retinogeniculate and geniculocortical pathways in rodents and primates primarily use VGluT2 in its modulation of glutamatergic transmission, we speculate that the same is true for pinnipeds. Therefore, we can use VGluT2 expression to identify the visual structures in the pinniped brain and use its distribution to speculate on their connections. More specifically, cortical areas which show a dense expression of VGluT2 protein in thalamocortical recipient layer 4 are likely to be part of visual cortex.

REFERENCES

Aihara Y, Mashima H, Onda H, Hisano S, Kasuya H, Hori T, Yamada S, Tomura H, Yamada Y, Inoue I, Kojima I, Takeda J (2000) Molecular cloning of a novel brain-type Na(+)-dependent inorganic phosphate cotransporter. J Neurochem 74:2622-2625.

Azevedo FA, Carvalho LR, Grinberg LT, Farfel JM, Ferretti RE, Leite RE, Jacob Filho W, Lent R, Herculano-Houzel S (2009) Equal numbers of neuronal and nonneuronal cells make the human brain an isometrically scaled-up primate brain. J Comp Neurol 513:532-541.

Bahney J, von Bartheld CS (2014) Validation of the isotropic fractionator: comparison with unbiased stereology and DNA extraction for quantification of glial cells. J Neurosci Methods 222:165-174.

Balaram P, Hackett TA, Kaas JH (2011a) VGLUT1 mRNA and protein expression in the visual system of prosimian galagos (Otolemur garnetti). Eye Brain 2011:81-98.

Balaram P, Hackett TA, Kaas JH (2013) Differential expression of vesicular glutamate transporters 1 and 2 may identify distinct modes of glutamatergic transmission in the macaque visual system. J Chem Neuroanat 50-51:21-38.

Balaram P, Isaamullah M, Petry HM, Bickford ME, Kaas JH (2015) Distributions of vesicular glutamate transporters 1 and 2 in the visual system of tree shrews (Tupaia belangeri). J Comp Neurol 523:1792-1808.

Balaram P, Takahata T, Kaas JH (2011b) VGLUT2 mRNA and protein expression in the visual thalamus and midbrain of prosimian galagos (Otolemur garnetti). Eye Brain 2011:5-15.

Baldwin MK, Balaram P, Kaas JH (2013) Projections of the superior colliculus to the pulvinar in prosimian galagos (Otolemur garnettii) and VGLUT2 staining of the visual pulvinar. J Comp Neurol 521:1664-1682.

Bellocchio EE, Reimer RJ, Fremeau RT, Jr., Edwards RH (2000) Uptake of glutamate into synaptic vesicles by an inorganic phosphate transporter. Science 289:957-960.

Berta A, Sumich JL, Kovacs KM (2015) Marine mammals : evolutionary biology. Boston, MA: Elsevier.

Casagrande VA (1994) The afferent, intrinsic, and efferent connections of primary visual cortex in primates. In: Cerebral Cortex (Peters, A. and Rockland, K. S., eds), pp 201-259 New York: Plenum.

Catania KC (2011) The sense of touch in the star-nosed mole: from mechanoreceptors to the brain. Philos Trans R Soc Lond B Biol Sci 366:3016-3025.

Collins CE, Young NA, Flaherty DK, Airey DC, Kaas JH (2010) A rapid and reliable method of counting neurons and other cells in brain tissue: a comparison of flow cytometry and manual counting methods. Front Neuroanat 4:5.

Elston GN (2007) Specialization of the neocortical pyramidal cell during primate evolution. Evolution of Nervous Systems 4:191-242.

Erwin J, Hof PR (2002) Aging in nonhuman primates. Basel ; New York: Karger.

Fooden J (1976) Provisional classification and key to living species of macaques (Primates: Macaca). Folia primatol 25:225-236.

Fremeau RT, Jr., Kam K, Qureshi T, Johnson J, Copenhagen DR, Storm-Mathisen J, Chaudhry FA, Nicoll RA, Edwards RH (2004a) Vesicular glutamate transporters 1 and 2 target to functionally distinct synaptic release sites. Science 304:1815-1819.

Fremeau RT, Jr., Voglmaier S, Seal RP, Edwards RH (2004b) VGLUTs define subsets of excitatory neurons and suggest novel roles for glutamate. Trends Neurosci 27:98-103.

Geptner VG, Nasimovich AA, Bannikov AG, Hoffmann RS, Sludskiĭ AA (1988) Mammals of the Soviet Union. Washington, D.C.: Smithsonian Institution Libraries and National Science Foundation.

Hackett TA, de la Mothe LA (2009) Regional and laminar distribution of the vesicular glutamate transporter, VGluT2, in the macaque monkey auditory cortex. J Chem Neuroanat 38:106-116.

Hackett TA, Takahata T, Balaram P (2011) VGLUT1 and VGLUT2 mRNA expression in the primate auditory pathway. Hear Res 274:129-141.

Herculano-Houzel S (2011a) Brains matter, bodies maybe not: the case for examining neuron numbers irrespective of body size. Ann N Y Acad Sci 1225:191-199.

Herculano-Houzel S (2011b) Not all brains are made the same: new views on brain scaling in evolution. Brain Behav Evol 78:22-36.

Herculano-Houzel S (2012) The remarkable, yet not extraordinary, human brain as a scaled-up primate brain and its associated cost. Proc Natl Acad Sci U S A 109 Suppl 1:10661-10668.

Herculano-Houzel S, Avelino-de-Souza K, Neves K, Porfirio J, Messeder D, Mattos Feijo L, Maldonado J, Manger PR (2014a) The elephant brain in numbers. Front Neuroanat 8:46.

Herculano-Houzel S, Collins CE, Wong P, Kaas JH (2007) Cellular scaling rules for primate brains. Proc Natl Acad Sci U S A 104:3562-3567.

Herculano-Houzel S, Lent R (2005) Isotropic fractionator: a simple, rapid method for the quantification of total cell and neuron numbers in the brain. J Neurosci 25:2518-2521.

Herculano-Houzel S, Manger PR, Kaas JH (2014b) Brain scaling in mammalian evolution as a consequence of concerted and mosaic changes in numbers of neurons and average neuronal cell size. Front Neuroanat 8:77.

Herzog E, Bellenchi GC, Gras C, Bernard V, Ravassard P, Bedet C, Gasnier B, Giros B, El Mestikawy S (2001) The existence of a second vesicular glutamate transporter specifies subpopulations of glutamatergic neurons. J Neurosci 21:RC181.

Hindell M (2002) Elephant seals. In: Encyclopedia of Marine Mammals (Perrin, W. et al., eds) London: Academic Press.

Jacobsen CF (1936) The functions of the frontal association areas in monkeys. Comp Psychol Mon 13:3-60.

Kaas JH (2002) Convergences in the modular and areal organization of the forebrain of mammals: implications for the reconstruction of forebrain evolution. Brain Behav Evol 59:262-272.

Kaas JH (2004) Evolution of somatosensory and motor cortex in primates. Anat Rec A Discov Mol Cell Evol Biol 281:1148-1156.

Kaas JH (2005) From mice to men: the evolution of the large, complex human brain. J Biosci 30:155-165.

Kaas JH (2012) Evolution of columns, modules, and domains in the neocortex of primates. Proc Natl Acad Sci U S A 109 Suppl 1:10655-10660.

Kaas JH, Huerta MF, Weber JT, Harting JK (1978) Patterns of retinal terminations and laminar organization of the lateral geniculate nucleus of primates. J Comp Neurol 182:517-553.

Kaneko T, Fujiyama F, Hioki H (2002) Immunohistochemical localization of candidates for vesicular glutamate transporters in the rat brain. J Comp Neurol 444:39-62.

Kelling AS, Snyder RJ, Marr MJ, Bloomsmith MA, Gardner W, Maple TL (2006) Color vision in the giant panda (Ailuropoda melanoleuca). Learn Behav 34:154-161.

Krubitzer L, Manger P, Pettigrew J, Calford M (1995) Organization of somatosensory cortex in monotremes: in search of the prototypical plan. J Comp Neurol 351:261-306.

Krubitzer LA, Kaas JH (1989) Cortical integration of parallel pathways in the visual system of primates. Brain Res 478:161-165.

Lankau EW, Turner PV, Mullan RJ, Galland GG (2014) Use of nonhuman primates in research in North America. J Am Assoc Lab Anim Sci 53:278-282.

Levenson DH, Dizon A (2003) Genetic evidence for the ancestral loss of short-wavelength-sensitive cone pigments in mysticete and odontocete cetaceans. Proc Biol Sci 270:673-679.

Li J, Han K, Xing J, Kim HS, Rogers J, Ryder OA, Disotell T, Yue B, Batzer MA (2009) Phylogeny of the macaques (Cercopithecidae: Macaca) based on Alu elements. Gene 448:242-249.

Liguz-Lecznar M, Skangiel-Kramska J (2007) Vesicular glutamate transporters VGLUT1 and VGLUT2 in the developing mouse barrel cortex. Int J Dev Neurosci 25:107-114.

Miller DJ, Balaram P, Young NA, Kaas JH (2014) Three counting methods agree on cell and neuron number in chimpanzee primary visual cortex. Front Neuroanat 8:36.

Montie EW, Pussini N, Schneider GE, Battey TW, Dennison S, Barakos J, Gulland F (2009) Neuroanatomy and volumes of brain structures of a live California sea lion (Zalophus californianus) from magnetic resonance images. Anat Rec (Hoboken) 292:1523-1547.

Murie J (1874) Researches upon the anatomy of the Pinnipedia-Part III. Descriptive anatomy of the sea-lion (Otaria jubata). Transact Zool Soc Lond 8:501-582.

Murphy WJ, Eizirik E, O'Brien SJ, Madsen O, Scally M, Douady CJ, Teeling E, Ryder OA, Stanhope MJ, de Jong WW, Springer MS (2001) Resolution of the early placental mammal radiation using Bayesian phylogenetics. Science 294:2348-2351.

Nahmani M, Erisir A (2005) VGluT2 immunochemistry identifies thalamocortical terminals in layer 4 of adult and developing visual cortex. J Comp Neurol 484:458-473.

Passingham R (2009) How good is the macaque monkey model of the human brain? Curr Opin Neurobiol 19:6-11.

Robson SL, Wood B (2008) Hominin life history: reconstruction and evolution. J Anat 212:394-425.

Sawyer EK, Turner EC, Kaas JH (2016) Somatosensory brainstem, thalamus, and cortex of the California sea lion (Zalophus californianus). J Comp Neurol 524:1957-1975.

Springer MS, de Jong WW (2001) Phylogenetics. Which mammalian supertree to bark up? Science 291:1709-1711.

Van Essen DC (2005) Corticocortical and thalamocortical information flow in the primate visual system. Prog Brain Res 149:173-185.

CHAPTER 2

Cortical cell and neuron density estimates in one chimpanzee hemisphere

The following chapter was published under the same title in the Proceedings of the National Academy of Science USA by Christine Collins, Emily Turner, Eva Sawyer, Jamie Reed, Nicole Young, David Flaherty, and Jon Kaas; January 2016.

Abstract

The density of cells and neurons in the neocortex of many mammals varies across cortical areas and regions. This variability is, perhaps, most pronounced in primates. Nonuniformity in the composition of cortex suggests regions of the cortex have different specializations. Specifically, regions with densely packed neurons contain smaller neurons that are activated by relatively few inputs, thereby preserving information, whereas regions that are less densely packed have larger neurons that have more integrative functions. Here we present the numbers of cells and neurons for 742 discrete locations across the neocortex in a chimpanzee. Using isotropic fractionation and flow fractionation methods for cell and neuron counts, we estimate that neocortex of one hemisphere contains 9.5 billion cells and 3.7 billion neurons. Primary visual cortex occupies 35 cm^2 of surface, 10% of the total, and contains 737 million densely packed neurons, 20% of the total neurons contained within the hemisphere. Other areas of high neuron packing include secondary visual areas, somatosensory cortex, and prefrontal granular

cortex. Areas of low levels of neuron packing density include motor and premotor cortex. These values reflect those obtained from more limited samples of cortex in humans and other primates.

Introduction

The present study is part of our ongoing effort to determine how human brains are both similar and different from the brains of our closest living primate relatives. Present-day chimpanzees and bonobos diverged from the line of hominins that led to modern humans some 6 million years ago (Goodman et al., 1989). The modern chimpanzee brain is similar in size to our earliest hominin ancestors (Le Gros Clark, 1959). In contrast, the brains of later hominins rapidly increased in size about 1.5 million years ago, resulting in modern humans having brains about three times the size of early hominins and present-day chimpanzees. Similarly, the neocortical sheet of one cerebral hemisphere is almost three times larger in humans (average, ~975 cm^2 in humans) (Tramo et al., 1995; Van Essen et al., 2012) than in chimpanzees (~341 cm^2). This increase also appears to be reflected in an increase in the number of areas that are architectonically and physiologically modified for different specialized functions. Such specializations are reflected in a wide range of neuron types and laminar and sublaminar patterns of regional and areal organization in larger primate brains, especially those of humans (Sherwood and Hof, 2007). It would be surprising if average neuron size and neuron packing densities did not vary across areas, especially in large-brained primates. However, the claim has been made that neuron densities are uniform across cortical areas and mammalian species, except for a twofold increase in primary visual cortex (V1) in some primates (Rockel et al., 1980; Carlo and Stevens, 2013). This conclusion is contrary to the results of several previous studies

(Beaulieu and Colonnier, 1989), especially those of our recent reports on neuron densities across the cortical sheet in several primate species (Collins et al., 2010a; Young et al., 2013a). The primates examined to date (baboons, macaques, and galagos) had much higher neuron densities in V1. Neuron densities were also higher than average in other sensory areas, and considerably lower in primary motor cortex (M1), with more pronounced differences appearing in larger-brained primates. As there is a relationship between neuron density in cortex and average neuron size (Collins et al., 2010a; Cahalane et al., 2012), and larger neurons have larger dendritic arbors with more synaptic contacts (Elston et al., 2006), larger neurons are more suitable for integrative functions, whereas smaller neurons preserve information and more faithfully reflect the sources of their activation (Kaas, 2000; Elston, 2007; Collins, 2011).

Here, we extend our observations on areal neuron densities in strepsirrhine galagos and anthropoid monkeys to the full neocortical sheet of a chimpanzee (*Pan troglodytes*). We provide the most detailed assessment of cortical neuron densities across the cortical sheet for any species, having dissected the chimpanzee cortex into 742 tissue pieces, providing roughly six times more detail than has ever been reported for the cortex of any primate species (Collins et al., 2010a) and nearly 100 times more evaluations than a typical quantitative study (Beaulieu and Colonnier, 1989). This comprehensive approach allows us to demonstrate significant regional differences in neuron densities that may be small enough to be lost in the noise of more limited studies. Although this has not yet been attempted for a human brain, direct comparisons will be possible in future studies.

Materials and Methods

Experimental procedures were all approved by the Vanderbilt Institutional Animal Care and Use Committee. One adult female chimpanzee brain was obtained for this study from the Texas Biomedical Research Institute. The age of the chimpanzee was estimated to be 53 years old. The animal was humanely killed because of myocarditis (heart failure). The neocortex is expected to have few age-related changes in a chimpanzee of this age (Sherwood et al., 2011; Autrey et al., 2014). Shortly before death, her body weight was 34.8 kg. The brain was flushed with 0.9% PBS, removed from the skull, and shipped overnight in the same solution. On arrival, the brain weight was 344 g. The brain was bisected into right and left hemispheres. The right neocortex was flattened and used in this report, and the left hemisphere was sectioned and histologically processed for other studies.

To determine neuron and cell number per unit of cortical surface area across all parts of the cortical surface, we first manually flattened the neocortex into a sheet. The unfixed cortex of the right hemisphere was separated from the underlying structures and most of the white matter. A cut was made in the depth of the central sulcus to separate the most anterior region, and another cut was made to separate primary visual cortex from the rest of the caudal cortex, creating three separate cortical pieces for flattening. This was done to preserve the integrity of the tissue during flattening. Sulci were carefully opened, and the cortical sheet was then unfolded under gentle pressure (Fig. 2.1A). Excess white matter was removed. After post-fixing in 4% (wt/vol) paraformaldehyde for two weeks, each sheet was cut into small pieces, $\sim$5 mm^2 in surface area, resulting in 742 pieces that were photographed, weighed, numbered, and assigned to a cortical area when possible (Fig. 2.1 B and C). Pieces were assigned to cortical areas based on their expected relation to sulcal landmarks and their myelin content, as primary sensory areas

appear dark relative to the surrounding cortex when viewed on a light box because of their myelin-dense composition. The surface area of each piece of cortex was measured from the photograph, using ImageJ (NIH). Each piece of cortex was individually disassociated to a solution, where cell membranes were ruptured but cell nuclei remained intact, as previously described (Herculano-Houzel and Lent, 2005; Collins et al., 2010b). We determined the number of cells in each tissue piece, using the isotropic fractionator method (Herculano-Houzel and Lent, 2005). The flow fractionator method was used to estimate of the total number of neuron nuclei labeled with the anti-NeuN antibody and DAPI in each tissue piece, as previously described in detail (Collins et al., 2010a; Collins et al., 2010b; Young et al., 2012; Young et al., 2013a; Young et al., 2013b).

IBM-SPSS software (version 22) was used to test for deviations from the normal distribution (Kolmogorov-Smirnov test), to test for nonlinearities (linear regression), and to compare cell and neuron densities between selected cortical areas (generalized linear modeling). Significance was considered for $P < 0.05$. Statistical analysis included using Huber-White robust SEs through the generalized linear modeling procedures specifying "robust" covariance matrix estimators (also called Huber-White or sandwich estimators) in SPSS software. Robust SEs are corrections to help account for violations of the assumption of independence between cell counts on tissue pieces from a single chimpanzee brain. The resulting P values can be used to help describe differences within the one brain, but they do not directly allow inferences about the population of chimpanzees.

Cell and neuron numbers per square centimeter of cortical surface were obtained for each piece of cortex and color coded for cells (Fig. 2.1B) or neurons (Fig. 2.1C). In addition, each dissected piece of tissue was assigned coordinates along the A-P axis by generating centroid

measures for each piece, using NIH ImageJ software. Cell and neuron numbers per square centimeter of surface area versus the A-P locations were plotted and used in linear regression curve-fitting estimations to assess whether cell and neuron densities were uniform or increased or decreased in the A-P dimension with linear, quadratic, and cubic regression models.

The results were tested for deviations from the normal distribution (Kolmogorov-Smirnov test), and generalized linear regression modeling was then used to compare cell and neuron densities between selected cortical areas. Selected cortical areas defined by experts were the components of one fixed factor (see Fig. 2.1C for regional bin map), and A-P coordinates (x-value from the centroid calculation) were binned for use as the components of the second fixed factor. Model main effects were tested and evaluated for the relative contribution of each factor to the variance in mean density. Multiple comparisons were adjusted by the Bonferroni method, and robust estimators, as addressed earlier, were used in this analysis to account for violations of independence between the samples from a single chimpanzee

Results

The total surface area of the cerebral cortex of the right hemisphere of this chimpanzee was 341 cm^2, although that could be a slight underestimate resulting from a loss of some neocortex along the outer margins of the cortical sheet. The neocortex contained an estimated 9.51 billion cells (count includes all cell types identified by DAPI; e.g., glial, neuronal, etc.), of which about 3.71 billion, or 39%, were neurons (only cells that stain positive for neuronal nuclear antigen). The cell and neuron counts for individual pieces of tissue varied considerably (Fig. 2.1). Some of this variation may be random, possibly reflecting biases based on tissue

distortions during flattening or other processing factors. Nevertheless, there were large, statistically significant regional and areal differences that were reflected by the comparisons of mean counts (see Fig. 2.2 A and B for statistics).

Visual areas of cortex

The estimated surface area of V1 from the right hemisphere of the present chimpanzee was 35.04 cm^2, about 10% of the total neocortical surface. This estimate was based on the piece of cortex that was separated along the margin of the lunate fissure, which marks the rostral border of V1 (Bailey et al., 1950; Holloway et al., 2003). We compensated for a slight error in that cut by adding a narrow margin of tissue from the larger main piece, as shown in red in Fig. 2.1 B and C. The estimated volume of V1 (5.30 cm^3) is close to previous estimates of 5.52 cm^3 (Bush and Allman, 2004) and 4.64 cm^3 (de Sousa et al., 2010), as well as those from the other hemisphere of our chimpanzee based on measures from serial brain sections (4.8 cm^3) (Miller et al., 2014). Cell and neuron packing densities were greatest in V1. At only 10% of the neocortical

Fig. 2.1 **Distribution of cells and neurons across a flattened chimpanzee hemisphere.** **(A)** Lateral view of intact, adult female chimpanzee brain. **(B)** Complete dissection map, illustrating the 742 pieces of tissue dissected from the chimpanzee cortex. Total cell density in millions of cells per square centimeter of cortical surface is illustrated on the cortex flat map, with the darkest shading indicated areas of high cell density and lighter shading indicating low cell density. The total cell density includes all types of cells in cortex; that is, neurons, glial cells, and epithelial cells. Areal boundaries are estimated for V1, V2, somatosensory (areas 3b, 3a, 1, and 2), motor (areas 4 and 6), and premotor cortex. **(C)** Complete dissection map illustrating the 742 pieces of tissue dissected from the chimpanzee cortex. Total neuron density in millions of cells per square centimeter of cortical surface is illustrated on the cortex flat map, with the darkest shading indicating areas of high neuron density and lighter shading indicating low neuron density.

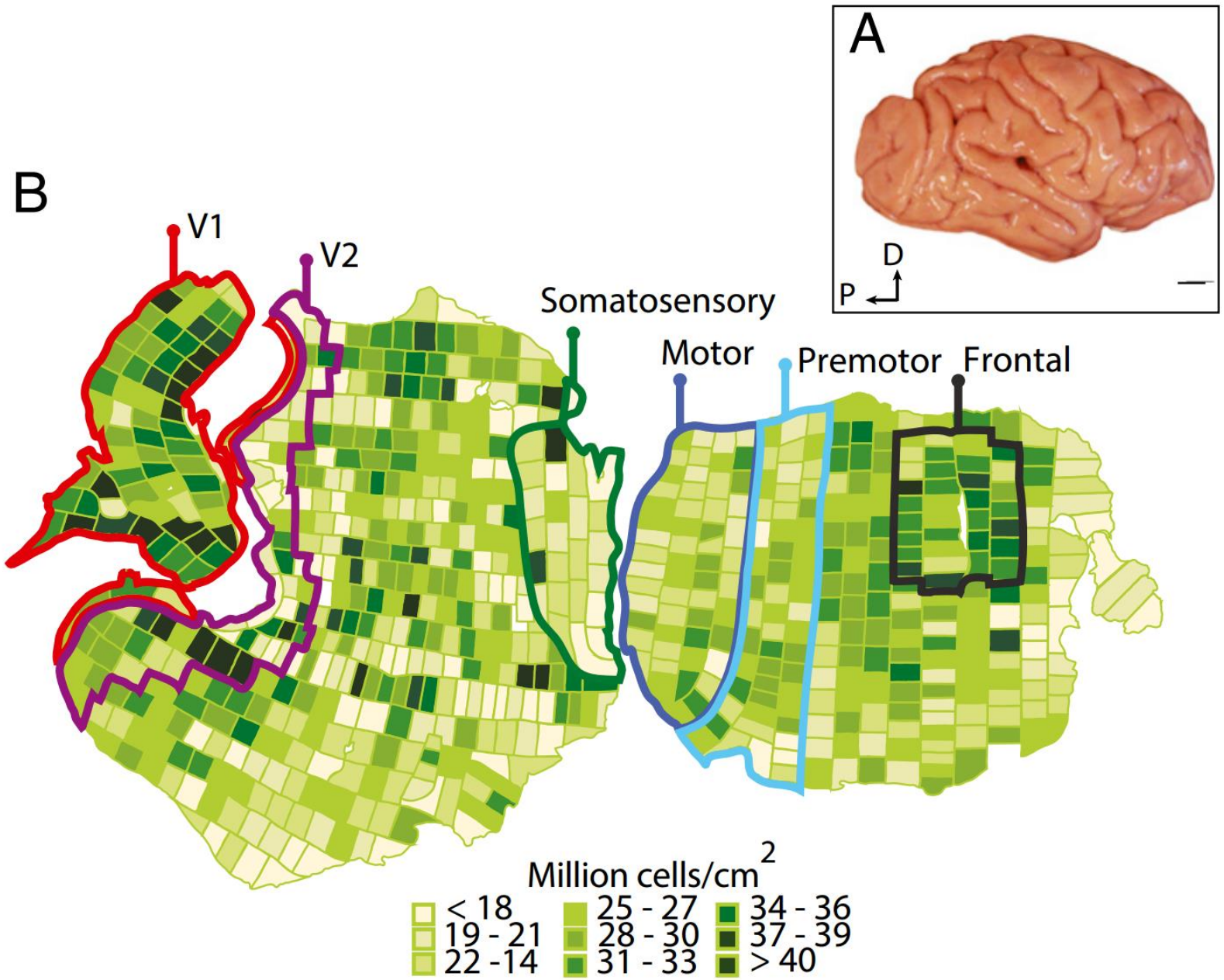
A
D
P
B
V1
V2
Somatosensory
Motor
Premotor
Frontal
Million cells/cm 2
< 18
19 - 21
22 -14
25 - 27
28 - 30
31 - 33
34 - 36
37 - 39
> 40

C

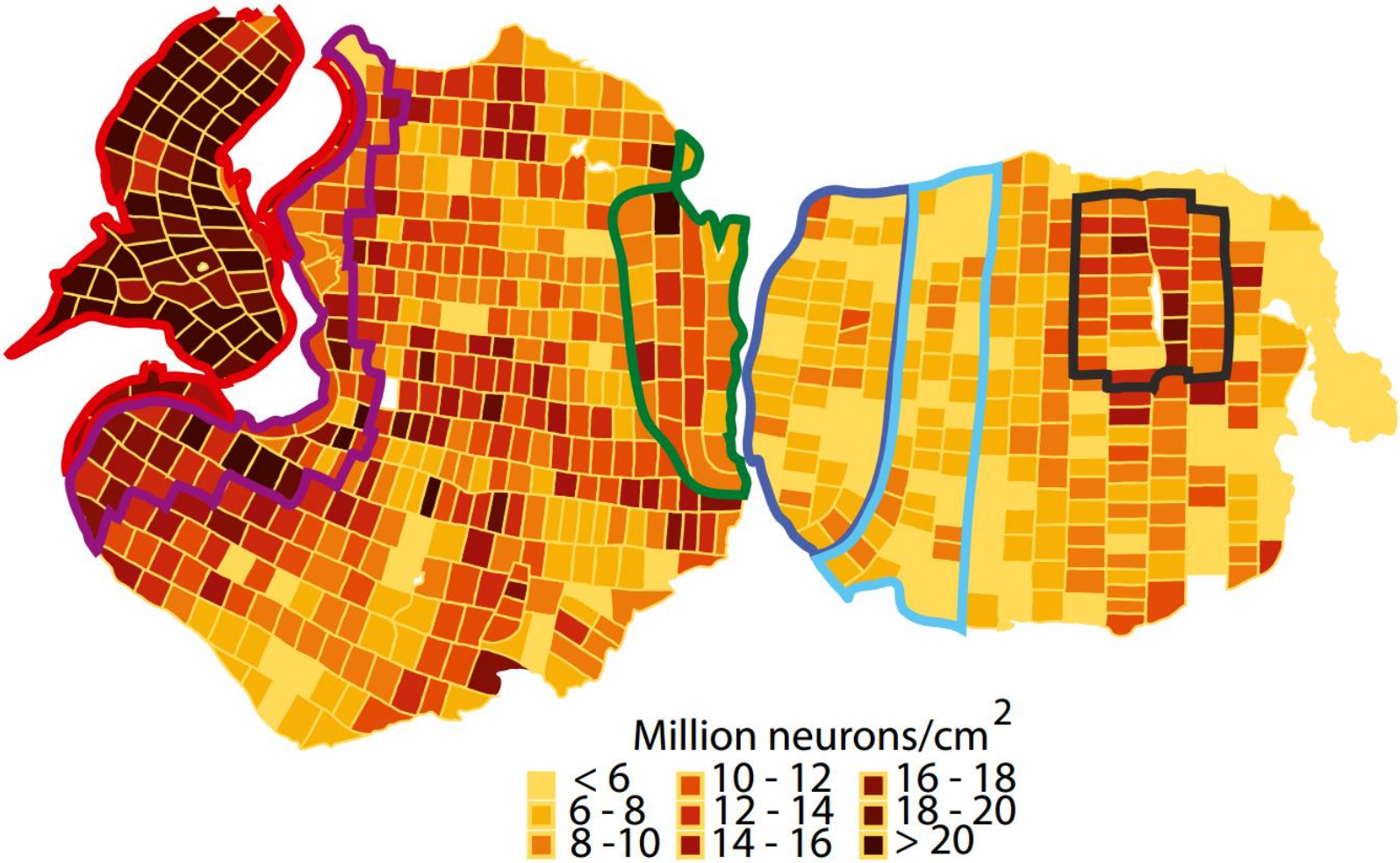

surface, V1 contained just more than 1.13 billion cells, of which 737 million, or 65%, were neurons. Cell densities in V1 averaged about 32 million cells per square centimeter of surface (see Fig. 2.2B, which shows estimated means) or 138 million cells per gram of tissue. The average neuron density was 21 million neurons per square centimeter of cortical surface (Fig. 2.2A), or 89 million neurons per gram of cortical tissue. Cell and neuron densities varied across the 77 pieces of V1, but most had neuron densities near or higher than 20 million per square centimeter. The packing densities of neurons in V1 were 1.2, 2.1, 3.3, and 3.5 times greater than neuron densities in secondary visual cortex (V2) and somatosensory, motor, and premotor cortices, respectively. Total cell densities were less variable across cortex, but were still 1.3, 1.5, 1.3, and 1.4 times greater than in V2, somatosensory, motor, and premotor areas, respectively.

The higher cell and neuron packing densities distinguished V1 from all other areas of cortex. Although the full extent of V2 in chimpanzees is somewhat uncertain, the location shown in Fig. 2.1 conforms to expectations. This estimate of V2 comprises 28.69 cm^2 of cortical surface, or 8% of the total neocortical surface. The total cells in V2 were just more than 788 million, of which 396 million, or 50%, were neurons. The average cell densities in V2 were 27 million per square centimeter of surface (Fig. 2.2B), or 115 million cells per gram of tissue. The average neuron density in V2 was 14 million neurons per square centimeter of cortical surface (Fig. 2.2A), or 59 million neurons per gram of cortical tissue, a drop of 7 million neurons per square centimeter or 30 million neurons per gram from V1, but still higher than other cortical regions. Neuron densities in V2 were 1.2, 2.1, and 2.2 times greater than those in somatosensory, motor, and premotor cortices, respectively.

Cortex just rostral to V2 is expected to contain a number of visual areas that have been identified in macaque monkeys and other primates, including visual areas V3 and V4 and

dorsomedial visual area (Lyon and Kaas, 2002a; 2002b). These and other caudal visual areas would all have higher than average cell, and especially neuron, packing densities, although not as high as V1 and V2. These data support the conclusion that retinotopically organized visual areas in chimpanzees have high neuron packing densities.

Fig. 2.2 **Cell and neuron density estimated regional means.** Pairwise comparison results of estimated marginal means based on the original scale of the dependent variable, either neuron **(A)** or cell **(B)** density in square centimeter, with mean differences significant at $P < 0.05$ and robust SE bars shown. All significant pairwise comparisons are highlighted by the significance bars. **(A)** V1 estimated marginal means of neuron density are significantly higher than all other cortical regions, whereas V2 is significantly higher than motor, premotor, and somatosensory blocks. Somatosensory predicted values are also significantly higher than motor and premotor blocks. Motor and premotor cortices do not significantly differ from one another, but are both significantly lower than all other areas of cortex. **(B)** V1 and the frontal region estimates show no significant differences in cell density, but each region independently contains higher means than every other area. Somatosensory, premotor, and motor cortex do not significantly differ from one another.

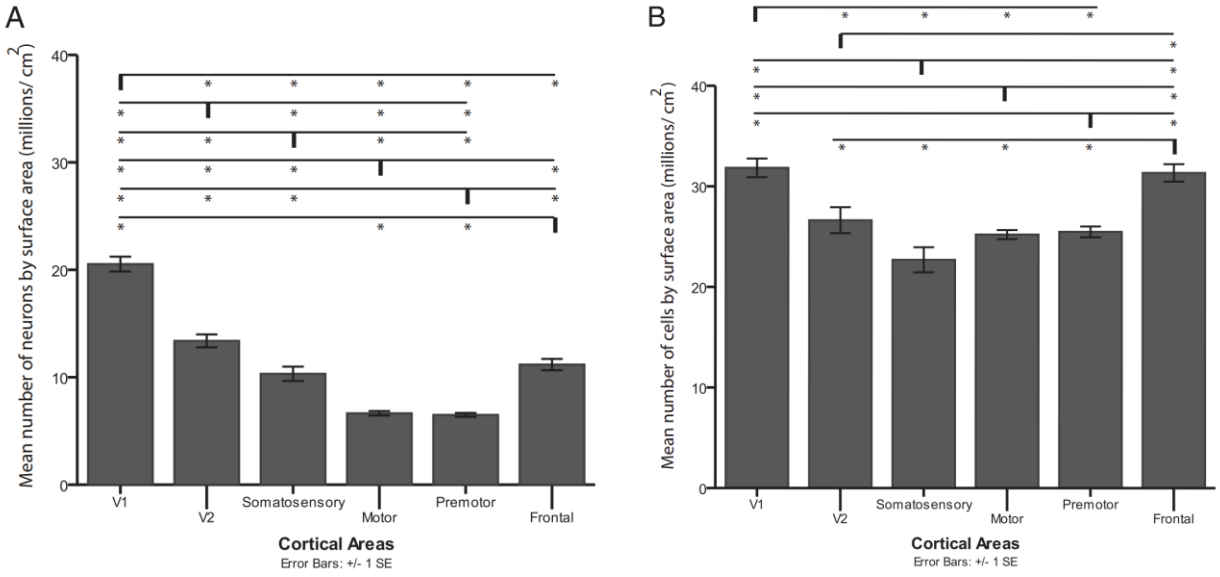

Somatosensory areas

Somatosensory areas had higher than average neuron packing densities relative to nonprimary sensory areas. Anterior parietal cortex of chimpanzees and other anthropoid primates includes areas 3a, 3b, 1, and 2 (Qi et al., 2008), with area 3b being the primary tactile area. The region designated as somatosensory cortex in Fig. 2.1 likely contains most of areas 3b, 1, and 2. As we separated rostral from caudal cortex along the depth of the central sulcus, our "somatosensory cortex" likely includes the caudal half of area 3a, with the rostral half included in motor cortex. The most lateral part of somatosensory cortex may have been excluded from our designated block, which was 16.6 cm^2 of surface, or 4.86% of neocortex. Cell densities in the somatosensory block averaged 22 million cells per square centimeter of surface (Fig. 2.2B), or 91 million cells per gram of tissue. Neuron numbers averaged 10 million per square centimeter (Fig. 2.2A), or 41 million neurons per gram of tissue. The somatosensory section of cortex contained 362 million cells, of which 164 million, or 45%, were neurons.

Motor and premotor areas

Our block of tissue pieces designated as motor in Fig. 2.1 likely contains most of M1, including the cortex of the rostral bank of the central sulcus and cortex of the caudal half of the precentral gyrus (Leyton and Sherrington, 1917; Hines, 1940; Bailey et al., 1950; Qi et al., 2008). The more rostral block of pieces likely includes dorsal and ventral divisions of premotor cortex. Our motor cortex block consisted of 24.97 cm^2 of cortical surface with 625 million cells, of which 163 million, or 27%, were neurons. Cell packing densities averaged 25 million cells per square centimeter of cortical surface (Fig. 2.2B), or 91 million cells per gram of tissue. Neuron packing densities averaged 7 million neurons per square centimeter of surface (Fig. 2.2A), or 24

million neurons per gram. Nearly all of the individual pieces of M1 had low neuron densities, in the 6–7 million range. Thus, M1 was characterized by low neuron packing densities and moderate cell packing densities.

Our premotor block included 24.46 cm^2 of cortical surface, with 636 million cells and 172 million neurons, for a composition of 26% neurons. Cell densities in premotor cortex averaged 25 million per square centimeter of cortical surface (Fig. 2.2B), or 88 million per gram of tissue. The average neuron packing density was 6 million neurons per square centimeter of cortical surface (Fig. 2.2A), or 23 million neurons per gram of cortical tissue. Thus, cortex in the premotor block had low levels of neuron packing, with little variability across tissue pieces, and closely matched the low neuron packing densities across motor areas.

Prefrontal cortex

Prefrontal cortex generally consists of the cortex rostral to premotor cortex, and it has several subdivisions including a large dorsolateral region of granular frontal cortex and adjoining regions of orbital frontal and medial frontal cortex (Preuss and Goldman-Rakic, 1991; Semendeferi et al., 2001; Passingham and Wise, 2012). Areal variations in neuron densities across prefrontal cortex have previously been shown in macaques (Dombrowski et al., 2001). Overall, the prefrontal block of tissue denoted in Fig. 2.1B and C has pieces of tissue with higher cell packing densities and neuron packing densities than those in either motor or premotor cortex. Most of this cortex with higher cell and neuron packing densities would be considered granular frontal cortex. Pieces of cortex with lower values were located along the margins of frontal cortex, including medial frontal and orbital frontal regions. However, we distinguished a dorsomedial block of cortex within the presumptive region of granular frontal cortex (Fig. 2.1C)

as having higher neuron densities than other prefrontal regions. Pieces of cortex in this block had average neuron packing densities of 11 million per square centimeter. Total cell densities averaged 30 million per square centimeter, or 106 million per gram, with 36% neurons. This high-density block of tissue covered 13.11 cm^2 with 515 cells and 181 million neurons.

The anterior to posterior pattern

To examine whether the chimpanzee brain showed uniform cell and neuron packing densities across cortex (or a linear decrease in density beyond V1 from posterior to anterior), we examined densities in pieces of cortex across the anterior-to-posterior (A-P) dimension, using linear regression and curve estimation, testing multiple model functions. Recently, there have been a number of descriptions of neuron packing densities across the cortical sheet in monkeys and other mammals that revealed a trend from low packing densities to high neuron packing densities from anterior to posterior cortex (Cahalane et al., 2012; Ribeiro et al., 2013; Cahalane et al., 2014; Charvet and Finlay, 2014; Charvet et al., 2015). When we assessed how cell and neuron densities varied in the selected cortical regions across the A-P dimension, using generalized linear modeling with robust estimators, most cortical areas showed significant differences in estimated means of neuron and cell density (Fig. 2.2 A and B). In addition, the locations of samples within cortical regions were better predictors than A-P coordinates alone of cell density (cortical area, $P = 6.4 \times 10^{-10}$; A-P, $P = 0.818$) and of neuron density (cortical area, $P = 1.0 \times 10^{-4}$; A-P, $P = 0.835$). When the density values for individual pieces were plotted by A-P location and color-coded for tissue block of origin, the average curve for neuron density had higher values in posterior cortex and a downward slope to lower values in anterior cortex (Fig. 2.3A). Although an A-P gradient is apparent in the array of values for individual pieces, it clearly does not correspond to a simple linear A-P gradient. This type of plotting allows V2 values to

mix with V1 values to contribute to a steep rise in the posterior slope that obscures the clear difference between V1 and V2. In addition, the prefrontal granular region contains high neuron packing values with a fringe of lower values. However, motor and premotor regions contain low values, the somatosensory region has moderate values, and much of temporal and posterior parietal regions have moderate values. A similar pattern, with less variation, is apparent for all cells (Fig. 2.3B). For the densities of cells and neurons, we found that cubic models provided the best correlations (Fig. 2.3 A and B), all with *P* values <0.0001. These results, including increased densities in frontal regions of cortex, support deviations from linear or uniform patterns across the A-P dimension.

Discussion

In the present study, we flattened the neocortex of one cerebral hemisphere of a chimpanzee into a sheet, divided the sheet into three main parts, and then further divided the large pieces into 742 small pieces of tissue. Tissue blocks were individually processed for estimates of total neuron numbers using the rapid and accurate flow fractionation method (Collins et al., 2010b; Young et al., 2012), and estimates of total cell number were obtained using the isotropic fractionation method (Herculano-Houzel and Lent, 2005). The results are shown in cell or neuron number per square centimeter of cortical surface because the number of neurons in the vertically defined cortical columns that extend across the depth of the cortex has been considered basic to cortical function (Kaas, 2012). The results indicate that areas of neocortex in chimpanzees differ greatly in packing density, such that visual areas V1 and V2 have the highest neuron density, and the motor and premotor areas are among those that have the

lowest densities. Perhaps surprisingly, a region of granular prefrontal cortex had higher neuron densities than surrounding cortical regions. These clear differences in cell and neuron densities,

Fig. 2.3 **Anterior to posterior plot of cell and neuron densities.** The cell and neuron densities of all 742 pieces are plotted based on their anterior–posterior position in the flattened cortex, and designated to a cortical area (shown in small map). Neuron **(A)** and cell **(B)** packing densities follow the same pattern, in which densities are highest in the most posterior positions and lower in more anterior positions, with the exception of a block of frontal cortex that contains higher densities. For both cell and neurons, although the correlation is low, cubic models provide a better correlation (neurons: $R^2 = 0.424$; cells: $R^2 = 0.066$) compared with linear (neurons: $R^2 = 0.303$; cells: $R^2 = 0.011$) or quadratic (neurons: $R^2 = 0.414$; cells: $R^2 = 0.035$) models. Most outliers are cell- or neuron-dense pieces in the posterior part of the brain.

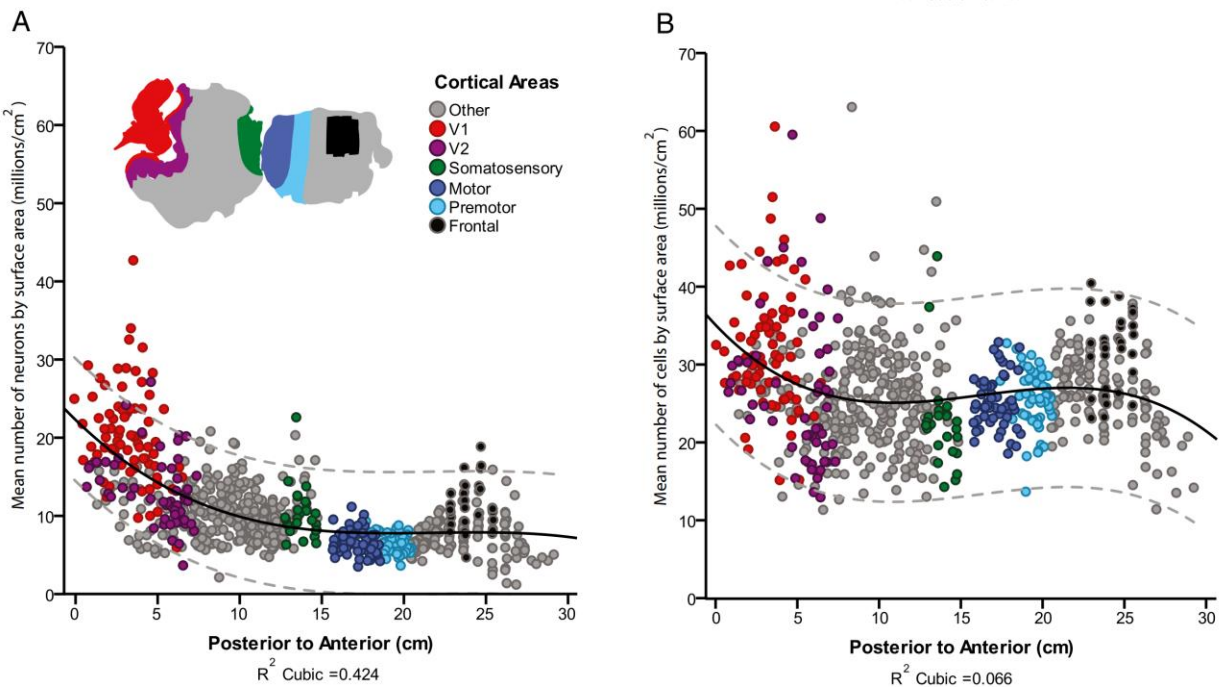

when considered together with the rapidly accumulating evidence from other primates, and even non-primate species (Campi et al., 2011; Herculano-Houzel et al., 2013), should dispel any notion that the neocortex is uniform in this respect. The present results have functional implications for the neocortex in chimpanzees and invite comparisons with the neocortex of other primates, especially with humans, as the closest biological extant relative of chimpanzees and bonobos.

Comparisons with other primates

Our results allow detailed comparisons with similar maps of flattened neocortex in macaques and baboons (Collins et al., 2010a; Young et al., 2013a; Young et al., 2013b). In these primates, V1 had the highest neuron densities, as much as three to six times that of most cortical regions. This is unsurprising, as larger numbers of neurons per cortical column have been previously reported in V1 of monkeys (Rockel et al., 1980), and more recently reproduced (Carlo and Stevens, 2013). However, those authors argued for the "basic uniformity" in neuron numbers across the depth of cortex for other areas of cortex, and across mammalian species. Here, we show that neuron numbers vary across the chimpanzee cortical sheet, with high values also in V2, somatosensory cortex, and part of frontal granular cortex, and low values in motor and premotor cortex. Most notably, neocortex in macaques and baboons also reflects this general pattern. In a more limited study of flattened cortex of a galago, V1 also had much higher neuron densities than other areas (Collins et al., 2010a), and M1 of owl monkeys, squirrel monkeys, and galagos has been shown to have low neuron densities in comparison with other cortical regions when studied with our current methods (Young et al., 2013a). Such a detailed comparison with neocortex of humans is not yet possible, but meaningful comparisons of neuron densities using another approach indicate impressive similarities with our present results. By using thick frontal

sections of a human brain and comparing neuronal densities across anterior to posterior slices of cortex, Ribeiro et al. (2013) reported very high neuron densities for posterior slices including V1, and very low values for anterior slices in frontal and prefrontal cortex. It is not clear yet from these results whether V1 and V2 differ, whether M1 and premotor cortex are specifically low in neuron number, or whether a granular region of prefrontal cortex with higher neuron densities exists. It is also uncertain whether primary somatosensory cortex is higher in primates in general, as expected from its well-developed layer of granular cells, or whether granular primary auditory cortex values are higher in any primate. As for the non-primates that have been studied, areal differences in mean densities may be less pronounced, but they vary considerably across cortical areas with high densities in V1 and primary somatosensory cortex (S1) in mice (Herculano-Houzel et al., 2013) and rats (Campi et al., 2011). Others have reported higher neuron densities in S1 than M1 and V2 in rats (Skoglund et al., 1996), and higher values in visual areas and S1 than M1 in cats (Beaulieu and Colonnier, 1989).

Evidence for a developmental pattern of cortical neurogenesis

In a series of publications, Finlay and colleagues have presented evidence that an anterior to posterior pattern of cortical development that is seen in primates and other mammals results in a matching gradient of neuron densities from low to high across the cortex (Cahalane et al., 2012; 2014; Charvet and Finlay, 2014; Charvet et al., 2015). Our chimpanzee results roughly reflect such a pattern, with at least four exceptions. These exceptions include the sharp increase in neuron densities in V1 from V2 at the V1–V2 border, the very low densities in motor and premotor cortex, the increased neuron densities in anterior somatosensory cortex, and the higher than expected neuron densities in dorsofrontal cortex of "granular" frontal cortex. These exceptions do not argue against the developmental gradient having an important role in creating

neuron density differences across the cortex, but the exceptions do indicate that other factors are also involved.

Such additional factors may include areal differences in neuron death during development (Cahalane et al., 2014). Direct evidence for this possibility comes from V1 of macaques after loss of visual inputs to the brain during fetal development. In such monkeys, parts of V1 fail to develop normally histologically (Rakic et al., 1991; Dehay et al., 2001), and these abnormal parts had cell densities reduced by about 25%. In view of the developmental gradient theory of regional differences in neuron densities, it may just be a fortunate circumstance for primates that V1 evolved in caudal neocortex. Higher neuron densities in V1 function to precisely preserve visual information, whereas motor and premotor cortex, as well as parts of prefrontal cortex, evolved within more anterior cortex to contain extremely low neuron densities as a result of larger neurons. This makes neurons in these anterior regions better suited to integrate information from many sources of activation. Alternatively, more modular features of cortical development could have played a prominent role in the evolution of such striking differences in neuron densities across cortex.

Functional implications

Differences across cortical areas in neuron packing densities imply there is an inverse relationship with average neuron size (Herculano-Houzel et al., 2014). Larger neurons take up more space and require more glial and other support cells that vary in size. Smaller neurons have smaller dendritic arbors and are connected by fewer inputs (Elston, 2002). Overall, small cortical neurons are better designed for preserving information from a small number of activating inputs, whereas large neurons are better suited for integrating information from a larger number of

activating inputs (Elston et al., 1996; Kaas, 2002). Thus, V1 has densely packed small neurons (granular cells) in layer 4 that are activated by just a few neurons in the dorsal lateral geniculate nucleus, and they activate other neurons in V1 that are, with few exceptions, small pyramidal neurons with small apical arbors contacted by relatively few inputs (Elston et al., 1996; Elston, 2002). The high neuron densities for V1 of primates have been postulated as a mechanism for preserving the high visual acuity of primates (Srinivasan et al., 2015). Motor cortex is known for its large pyramidal cells and lack of small layer 4 granular cells, which promotes integration from more sources of information. Primary sensory areas generally have smaller neurons with smaller dendritic arbors, whereas higher order sensory areas have larger neurons with larger arbors. The neuron density values in cortex illuminate this hypothesis in detail by indicating average levels of information preservation and integration for areas across the cortical sheet for chimpanzee. However, neurons of quite different sizes may occur in the same area and play different functional roles. For example, V1 contains both small granular cells in layer 4 and large Meynert cells in layers 5 and 6. However, the average neuron size should suggest a dominant role for a region or area.

One of the important findings of the present study was that a dorsal part of granular prefrontal cortex in the chimpanzee had a region of higher neuron density. As the term "granular frontal cortex" implies, this cortex contains small neurons in layer 4. However, large pyramidal neurons have also been described in prefrontal cortex, suggesting such neurons receive and sum many inputs (Elston et al., 2006). Although all parts of granular prefrontal cortex would seem suitable for preserving information, the dorsomedial part seems more specialized for this function. Notably, granular frontal cortex is thought to be a specialization of the primate brain (Preuss and Goldman-Rakic, 1991) that appears to be important in working memory (Funahashi

et al., 1989). Our present results are consistent with the conclusion that granular frontal cortex is not uniform in function (Passingham and Wise, 2012), and the region of particularly dense neuron packing in frontal cortex may be a specialization of primates that occurs to a lesser extent in Old World macaques (Collins et al., 2010a) and baboons (Young et al., 2013b), is especially marked in chimpanzees, and is likely in humans.

Significance

Chimpanzees are our closest relatives, and understanding the organization of their brains can help us understand our own evolution. Here we present a detailed examination of cell and neuron densities across the chimpanzee cortex. We found similarities to other mammals, including primary sensory areas with high neuron densities and a trend of decreasing neuron densities across the posterior to anterior axis of the cortex. However, we also found a prefrontal region with anomalously high neuron density that disrupts the trend of decreased neuron densities in frontal brain regions. The data reported here allow valuable comparisons among the brains of our close relative and those of humans and other primates.

REFERENCES

Autrey MM, Reamer LA, Mareno MC, Sherwood CC, Herndon JG, Preuss T, Schapiro SJ, Hopkins WD (2014) Age-related effects in the neocortical organization of chimpanzees: gray and white matter volume, cortical thickness, and gyrification. Neuroimage 101:59-67.

Bailey P, Von Bonin G, McCulloch WS (1950) The isocortex of the chimpanzee. Urbana: University of Illinois Press.

Beaulieu C, Colonnier M (1989) Number of neurons in individual laminae of areas 3B, 4 gamma, and 6a alpha of the cat cerebral cortex: a comparison with major visual areas. J Comp Neurol 279:228-234.

Bush EC, Allman JM (2004) The scaling of frontal cortex in primates and carnivores. Proc Natl Acad Sci U S A 101:3962-3966.

Cahalane DJ, Charvet CJ, Finlay BL (2012) Systematic, balancing gradients in neuron density and number across the primate isocortex. Front Neuroanat 6:28.

Cahalane DJ, Charvet CJ, Finlay BL (2014) Modeling local and cross-species neuron number variations in the cerebral cortex as arising from a common mechanism. Proc Natl Acad Sci U S A 111:17642-17647.

Campi KL, Collins CE, Todd WD, Kaas J, Krubitzer L (2011) Comparison of area 17 cellular composition in laboratory and wild-caught rats including diurnal and nocturnal species. Brain Behav Evol 77:116-130.

Carlo CN, Stevens CF (2013) Structural uniformity of neocortex, revisited. Proc Natl Acad Sci U S A 110:1488-1493.

Charvet CJ, Cahalane DJ, Finlay BL (2015) Systematic, cross-cortex variation in neuron numbers in rodents and primates. Cereb Cortex 25:147-160.

Charvet CJ, Finlay BL (2014) Evo-devo and the primate isocortex: the central organizing role of intrinsic gradients of neurogenesis. Brain Behav Evol 84:81-92.

Collins CE (2011) Variability in neuron densities across the cortical sheet in primates. Brain Behav Evol 78:37-50.

Collins CE, Airey DC, Young NA, Leitch DB, Kaas JH (2010a) Neuron densities vary across and within cortical areas in primates. Proc Natl Acad Sci U S A 107:15927-15932.

Collins CE, Young NA, Flaherty DK, Airey DC, Kaas JH (2010b) A rapid and reliable method of counting neurons and other cells in brain tissue: a comparison of flow cytometry and manual counting methods. Front Neuroanat 4:5.

de Sousa AA, Sherwood CC, Schleicher A, Amunts K, MacLeod CE, Hof PR, Zilles K (2010) Comparative cytoarchitectural analyses of striate and extrastriate areas in hominoids. Cereb Cortex 20:966-981.

Dehay C, Savatier P, Cortay V, Kennedy H (2001) Cell-cycle kinetics of neocortical precursors are influenced by embryonic thalamic axons. J Neurosci 21:201-214.

Dombrowski SM, Hilgetag CC, Barbas H (2001) Quantitative architecture distinguishes prefrontal cortical systems in the rhesus monkey. Cereb Cortex 11:975-988.

Elston GN (2002) Cortical heterogeneity: implications for visual processing and polysensory integration. J Neurocytol 31:317-335.

Elston GN (2007) Specialization of the neocortical pyramidal cell during primate evolution. Evolution of Nervous Systems 4:191-242.

Elston GN, Benavides-Piccione R, Elston A, Zietsch B, Defelipe J, Manger P, Casagrande V, Kaas JH (2006) Specializations of the granular prefrontal cortex of primates: implications for cognitive processing. Anat Rec A Discov Mol Cell Evol Biol 288:26-35.

Elston GN, Rosa MG, Calford MB (1996) Comparison of dendritic fields of layer III pyramidal neurons in striate and extrastriate visual areas of the marmoset: a Lucifer yellow intracellular injection. Cereb Cortex 6:807-813.

Funahashi S, Bruce CJ, Goldman-Rakic PS (1989) Mnemonic coding of visual space in the monkey's dorsolateral prefrontal cortex. J Neurophysiol 61:331-349.

Goodman M, Koop BF, Czelusniak J, Fitch DH, Tagle DA, Slightom JL (1989) Molecular phylogeny of the family of apes and humans. Genome 31:316-335.

Herculano-Houzel S, Lent R (2005) Isotropic fractionator: a simple, rapid method for the quantification of total cell and neuron numbers in the brain. J Neurosci 25:2518-2521.

Herculano-Houzel S, Manger PR, Kaas JH (2014) Brain scaling in mammalian evolution as a consequence of concerted and mosaic changes in numbers of neurons and average neuronal cell size. Front Neuroanat 8:77.

Herculano-Houzel S, Watson C, Paxinos G (2013) Distribution of neurons in functional areas of the mouse cerebral cortex reveals quantitatively different cortical zones. Front Neuroanat 7:35.

Hines M (1940) Movements elicited from the precentral gyrus of adult chimpanzees by stimulation with sine wave currents. J Neurophysiol 3:442-466.

Holloway RL, Broadfield DC, Yuan MS (2003) Morphology and histology of chimpanzee primary visual striate cortex indicate that brain reorganization predated brain expansion in early hominid evolution. Anat Rec A Discov Mol Cell Evol Biol 273:594-602.

Kaas JH (2000) Why is brain size so important: Design problems and solutions as neocortex gets bigger or smaller. Brain and Mind 1.

Kaas JH (2002) Convergences in the modular and areal organization of the forebrain of mammals: implications for the reconstruction of forebrain evolution. Brain Behav Evol 59:262-272.

Kaas JH (2012) Evolution of columns, modules, and domains in the neocortex of primates. Proc Natl Acad Sci U S A 109 Suppl 1:10655-10660.

Le Gros Clark WE (1959) The antecedents of man. Edinburgh: Edinburgh University Press.

Leyton SSF, Sherrington CS (1917) Observations on the excitable cortex of the chimpanzee, orangutan and gorilla. Q J Exp Physiol 11:135-222.

Lyon DC, Kaas JH (2002a) Evidence for a modified V3 with dorsal and ventral halves in macaque monkeys. Neuron 33:453-461.

Lyon DC, Kaas JH (2002b) Evidence from V1 connections for both dorsal and ventral subdivisions of V3 in three species of New World monkeys. J Comp Neurol 449:281-297.

Miller DJ, Balaram P, Young NA, Kaas JH (2014) Three counting methods agree on cell and neuron number in chimpanzee primary visual cortex. Front Neuroanat 8:36.

Passingham RE, Wise SP (2012) The Neurobiology of the Prefrontal Cortex. Anatomy, Evolution, and the Origin of Insight. Oxford: Oxford University Press.

Preuss TM, Goldman-Rakic PS (1991) Myelo- and cytoarchitecture of the granular frontal cortex and surrounding regions in the strepsirhine primate Galago and the anthropoid primate Macaca. J Comp Neurol 310:429-474.

Qi HX, Preuss TM, Kaas JH (2008) Somatosensory areas of the cerebral cortex: Architectonic characteristics and modular organization. In: The Senses: A Comprehensive Reference, vol. 6, Somatosensation (Gardner, E. P. and Kaas, J. H., eds), pp 143-170 London: Elsevier.

Rakic P, Suner I, Williams RW (1991) A novel cytoarchitectonic area induced experimentally within the primate visual cortex. Proc Natl Acad Sci U S A 88:2083-2087.

Ribeiro PF, Ventura-Antunes L, Gabi M, Mota B, Grinberg LT, Farfel JM, Ferretti-Rebustini RE, Leite RE, Filho WJ, Herculano-Houzel S (2013) The human cerebral cortex is neither one nor many: neuronal distribution reveals two quantitatively different zones in the gray matter, three in the white matter, and explains local variations in cortical folding. Front Neuroanat 7:28.

Rockel AJ, Hiorns RW, Powell TP (1980) The basic uniformity in structure of the neocortex. Brain 103:221-244.

Semendeferi K, Armstrong E, Schleicher A, Zilles K, Van Hoesen GW (2001) Prefrontal cortex in humans and apes: a comparative study of area 10. Am J Phys Anthropol 114:224-241.

Sherwood CC, Gordon AD, Allen JS, Phillips KA, Erwin JM, Hof PR, Hopkins WD (2011) Aging of the cerebral cortex differs between humans and chimpanzees. Proc Natl Acad Sci U S A 108:13029-13034.

Sherwood CC, Hof PR (2007) The evolution of neuron types and cortical histology in apes and humans. In: The Evolution of Nervous Systems, vol. 4 (Preuss, T. M. and Kaas, J. H., eds), pp 355-378 Oxford: Academic Press.

Skoglund TS, Pascher R, Berthold CH (1996) Heterogeneity in the columnar number of neurons in different neocortical areas in the rat. Neurosci Lett 208:97-100.

Srinivasan S, Carlo CN, Stevens CF (2015) Predicting visual acuity from the structure of visual cortex. Proc Natl Acad Sci U S A 112:7815-7820.

Tramo MJ, Loftus WC, Thomas CE, Green RL, Mott LA, Gazzaniga MS (1995) Surface area of human cerebral cortex and its gross morphological subdivisions: in vivo measurements in monozygotic twins suggest differential hemisphere effects of genetic factors. J Cogn Neurosci 7:292-302.

Van Essen DC, Glasser MF, Dierker DL, Harwell J (2012) Cortical parcellations of the macaque monkey analyzed on surface-based atlases. Cereb Cortex 22:2227-2240.

Young NA, Collins CE, Kaas JH (2013a) Cell and neuron densities in the primary motor cortex of primates. Front Neural Circuits 7:30.

Young NA, Flaherty DK, Airey DC, Varlan P, Aworunse F, Kaas JH, Collins CE (2012) Use of flow cytometry for high-throughput cell population estimates in brain tissue. Front Neuroanat 6:27.

Young NA, Szabo CA, Phelix CF, Flaherty DK, Balaram P, Foust-Yeoman KB, Collins CE, Kaas JH (2013b) Epileptic baboons have lower numbers of neurons in specific areas of cortex. Proc Natl Acad Sci U S A 110:19107-19112.

CHAPTER 3

Distributions of cells and neurons across the cortical sheet in Old World macaques

The following chapter was published under the same title in Brain, Behavior, and Evolution by Emily Turner, Nicole Young, Jamie Reed, Christine Collins, David Flaherty, Mariana Gabi, and Jon Kaas; August 2016.

Abstract

According to previous research, cell and neuron densities vary across neocortex in a similar manner across primate taxa. Here, we provide a more extensive examination of this effect in macaque monkeys. We separated neocortex from the underlying white matter in four macaque monkey hemispheres (one *Macaca nemestrina*, two *Macaca radiata*, and one *Macaca mulatta),* manually flattened the neocortex, and divided it into smaller tissue pieces for analysis. The number of cells and neurons were determined for each piece across the cortical sheet using flow cytometry. Primary visual cortex had the most densely packed neurons and primary motor cortex had the least densely packed neurons. With respect to differences in brain size between cases, there was little variability in the total cell and neuron numbers within specific areas, and overall trends were similar to what has been previously described in Old World baboons and other primates. The average hemispheric total cell number per hemisphere ranged from 2.9 to 3.7 billion, while the average total neuron number ranged from 1.3 to 1.7 billion neurons. The visual

cortex neuron densities were predictably higher, ranging from 18.2 to 34.7 million neurons/cm^2 in macaques, in comparison to a range of 9.3–17.7 million neurons/cm^2 across cortex as a whole. The results support other evidence that neuron surface densities vary across the cortical sheet in a predictable pattern within and across primate taxa.

Introduction

This study is part of our ongoing efforts to characterize regional cell and neuron populations in primate neocortex. The primate cortex is divided into a large number of functionally specialized areas, which vary by neuron types, laminar patterns, and physiological properties (Sherwood and Hof, 2007; de Sousa et al., 2010). The adult cortex of non-hominin primates has a characteristic uneven distribution of cells and neurons across its extent that has been recently detailed in a small number of individuals across a range of primate taxa (one macaque, three baboons, and one galago) (Collins et al., 2010a; Young et al., 2013a; Young et al., 2013b). The uneven cell and neuron distribution is indicative of the variable processing roles and capabilities of different areas of the cerebral cortex. Typically, studies of cell and neuron numbers in cortex only report the total numbers in the cerebral cortex (Pakkenberg and Gundersen, 1997; Christensen et al., 2007; Herculano-Houzel et al., 2008). Other studies have provided counts for a few locations across the cortical sheet, in support of the conclusion that cell densities are rather uniform across cortex, with the exception of a twofold increase in primary visual cortex of primates (Rockel et al., 1980; Carlo and Stevens, 2013). In contrast, studies in rodents (Skoglund et al., 1996; Herculano-Houzel et al., 2013), cats (Beaulieu and Colonnier, 1989), and primates (Collins et al., 2010a; Young et al., 2013a; Young et al., 2013b;

Collins et al., 2016) have revealed consistent quantitative differences between cortical areas. Previous efforts in primates have confirmed that primary visual cortex (V1) and other secondary visual areas contain higher than average neuron numbers under a fixed amount of cortical surface area, while primary motor cortex (M1) contains lower than average neuron numbers. Such areal differences likely reflect differences in laminar composition, as motor areas have more widely distributed, large pyramidal cells in layers 3 and 5 and a minimal layer 4, while primary sensory areas such as V1 tend to contain a wide, neuron-dense layer 4 packed with small granule cells.

The most detailed studies of the densities of neurons across the cortical sheet involve estimates made from many locations, most recently 742 pieces of cortex from a hemisphere of a chimpanzee (Collins et al., 2016), and previous counts from a single macaque, three baboons (and two epileptic baboons), one New World squirrel monkey, and two galagos (Collins et al., 2010a; Young et al., 2013b). We extend these observations here to examine neuron surface density in detail across three species of Old World macaque monkeys. The genus *Macaca* is extremely diverse, with an estimated 22 different species currently recognized, and the earliest fossil records and molecular data point to their divergence from other *Papionini* species around 10 million years ago, which suggests a relatively fast-paced spread within the *Macaca* radiation [Delson et al., 2000; Raaum et al., 2005]. The genus *Macaca* is traditionally further subdivided into four species groups (silenus-sylvanus, fascicularis, sinica, and arctoides), and while all share a common ancestor, it has been reported that there are differences in brain volume between these species groups, between species in the same species group, and between individuals of the same species (Stephan et al., 1981; Allman et al., 1993; Allman, 1994; Hakeem et al., 1996). The average body weights for *Macaca nemestrina* (males: 11.2 kg, females: 6.5 kg) (Fooden, 1975) and *Macaca mulatta* (males: 11 kg, females: 8.8 kg) (Fooden, 1981) are considerably higher than

the average body weight for *Macaca radiata* (males: 6.7 kg, females: 3.9 kg) (Schwartz and Kemnitz, 1992). It is then likely that there are corresponding differences in brain size, the size of the cortical sheet, and, perhaps, numbers and distributions of cortical neurons. The present study serves as a further introduction to the discussion of individual and species differences in cell and neuron neocortical densities.

Materials and Methods

To evaluate the areal and regional differences in the distributions of cell and neuron numbers in cortex, neocortex from four hemispheres of three adult macaques [one *M. nemestrina*, two *M. radiata* (same animal), and one *M. mulatta*] was separated from underlying structures, manually flattened, dissected into small pieces, and processed for their neuronal and nonneuronal cellular content using the flow fractionator method (Collins et al., 2010b).

Tissue and cortex dissection

Experimental procedures were all approved by the Vanderbilt Institutional Animal Care and Use Committee. Cortex samples from four adult macaques were used in this study. Case 11-47 was purchased from the tissue program at the University of Washington National Primate Research Center. Cases 10-50 and 12-58 were obtained after unrelated experiments at Vanderbilt University. Young et al. (2013b) reported data for baboon cases 09-27 and 11-31, and those cell and neuron numbers are referenced and displayed in figures here for comparison. Table 3.1 summarizes specific details on the species, age, sex, hemisphere, and size specifications of each case. All brains were perfused with 0.9% phosphate-buffered saline (PBS) and 2% paraformaldehyde. Brains that were obtained outside the Vanderbilt University were shipped

overnight in PBS. All brains were bisected into the right (RH) and the left hemisphere (LH); the RH of case 10-50 was used in other studies, the LH of case 11-47 was processed in sections (as described below), and both hemispheres of case 12-58 were used in this study. The cortex was separated from the underlying subcortical structures, the pia mater was removed, and the sulci were opened with forceps to allow for manual flattening, as previously described (Gharbawie et al., 2011; Collins et al., 2016). Each hemisphere was then placed in a glass dish with PBS, covered with a weighted glass slide, and left for a minimum of 12 h to completely flatten (Gharbawie et al., 2011).

Table 3.1 Summary of experimental cases

Case	Species	Age, years	Sex	Hemi-sphere	Brain weight, g	Brain surface area, cm^2
12-58 LH	*M. radiata*	7.5	M	LH	25.0	100.6
12-58 RH	*M. radiata*	7.5	M	RH	24.8	103.4
11-47	*M. nemestrina*	11	F	RH	36.4	151.8
10-50	*M. mulatta*	14.2	M	LH	33.2	152.3
9-27	PHX	12.6	F	RH	56.3	186.0
11-31	PHA	13	F	RH	50.0	234.0

PHA = *P. hamadryas anubis*; PHX = *P. hamadryas anubis/cynocephalus* hybrid. In case 12-58, the frontal eye field and surrounding areas are missing, and in case 10-50, the A-P coordinates could not be obtained.

Cortical areas were dissected from the cortical sheet with a scalpel when possible, including primary visual cortex (V1), secondary visual cortex (V2), primary somatosensory

cortex (S1), and primary motor cortex (M1). These areas are readily identified when the flat cortex is viewed on a light box to visualize myelin-dense sensory areas that appear darker relative to surrounding cortical areas (Collins et al., 2010a; Campi et al., 2011; Young et al., 2013a). Areas V2, S1, and M1 could not be confidently obtained from case 10-50 due to lack of photographic documentation during the dissection. Once removed, cortical areas were further dissected into smaller pieces that measured approximately 5 × 5 mm, or smaller, and each piece was assigned to an internal representation (e.g., V1, M1) when possible. With the exception of case 10-50, whose flattened cortex could not be reconstructed, the exact locations of dissection cuts were indicated on a high-resolution photograph of the flattened cortex. Each piece was assigned a number and weighed. The surface area was measured for each piece using ImageJ software (National Institutes of Health). This software was also used to assign an anterior-posterior (A-P) coordinate by generating a centroid measure for the location of each tissue piece. Neuron numbers per square centimeter of surface area versus the A-P locations were plotted, and the data were used in curve estimation regression models to assess the relationships of neuron densities across the A-P dimension with linear, quadratic, cubic, and exponential models. The glial cell/neuron (G/N) ratios versus the A-P locations were also plotted and used in curve-fitting estimations.

Tissue homogenization for flow fractionator

Each piece was homogenized using a glass Tenbroeck tissue grinder in a solution of sodium citrate and Triton X-100 in distilled water. This method of tissue homogenization produces cells that are completely dissociated with the nuclei remaining intact (Herculano-Houzel and Lent, 2005; Collins et al., 2010b). Resulting suspensions were stored in 15-ml

conical tubes and left to settle for 24–72 h at 4°C. The volume of each sample was adjusted such that they all had the same appearance in terms of their clarity.

Total number of cells

The flow fractionator method was used to estimate the total number of cells per piece from complete counts of samples from the homogenized suspensions, as previously described (Young et al., 2012). In brief, the suspended samples were well mixed, and a 50-µl aliquot was removed and suspended in a 250-µl solution of PBS and DAPI (4′,6-diamidino-2-phenylindole; 0.5 mg/200 ml). All samples were prepared in duplicate to assess the reliability of each estimate. A 50-µl aliquot of CountBright absolute counting beads (Invitrogen) was added to each sample prior to evaluation with the flow cytometer. All samples were evaluated on a Becton Dickinson LSRII 5-laser flow cytometer using an Xcyte 355-nm laser for DAPI excitation. Samples were well mixed to assure a homogeneous distribution of beads and nuclei, and the flow cytometer evaluated the number of nuclear events that occur coincident with 1,000 CountBright bead events using the flow cytometer. As all samples were prepared in duplicate, a coefficient of variation was calculated for such pairs to detect variation between them that would affect the data. Samples with a coefficient of variation greater than 0.20 were rerun to determine the cell population estimate with greater accuracy. The side scatter (SSC-A) and DAPI parameters were used to selectively place the gate for counting. The flow cytometry expert (D.K.F.) placed the nuclear selection gate and was blind to the sample location in the cortex. All flow cytometry experiments were conducted in the Vanderbilt University Medical Center (VUMC) Flow Cytometry Shared Resource. The isotropic fractionator method (Herculano-Houzel and Lent, 2005) was used on 10% of samples to verify data obtained from the flow fractionator method (2.0 mg DAPI in 200 ml PBS).

Total number of neurons

The flow fractionator method was also used to determine the total number of neurons per cortical piece, as previously described [Collins et al., 2010b]. In brief, the suspension samples were homogenized and a 0.5-ml aliquot was removed and immunolabeled for the neuronal nuclear antigen (NeuN) that is present in neuronal nuclei. All aliquots were antigen retrieved in boric acid (0.2 M, pH = 9.0) at 70°C for 30 min. Samples were washed with PBS and re-suspended overnight in PBS and anti-NeuN antibody (1:600; Millipore) at room temperature on a shaker. The following day, samples were washed twice in PBS and re-suspended in secondary antibody solution of goat, anti-mouse IgG tagged with Alexa Fluor 647 (AF647; Invitrogen, Inc.) for 1 hour. Samples were then washed two more times, stained with DAPI (0.5 mg/200 ml), and then forced through a 35-μm mesh filter to remove debris from myelin and cell membranes. All samples were homogenized and evaluated on a Becton Dickinson LSRII 5-laser flow cytometer using the 640- nm laser. The proportion of AF647+ nuclei was determined for 1,000 DAPI+ events. The total number of neurons in each piece was then calculated by multiplying the proportion of neurons by the total cell estimate for that specific sample. The isotropic fractionator method (Herculano-Houzel and Lent, 2005) was again used on 10% of samples to verify data obtained from the flow fractionator method. The NeuN-immunoreactivity (IR) nuclei in suspension in these samples were instead brightly labeled with Alexa Fluor 594 goat anti-mouse IgG secondary antibody (AF594; Invitrogen, Inc.) and not filtered.

The number of other cells in cortex, the majority of which are glial cells (Azevedo et al., 2009; Herculano-Houzel, 2014), was obtained by subtracting the number of neurons from the total number of cells. The G/N ratio (Friede, 1954; Bass et al., 1971; Herculano-Houzel, 2014) was used as a measure to compare cortical areas. A nonparametric Kruskal-Wallis independent-

sample test with adjustments for multiple comparisons was used to compare the G/N ratio distributions in V1, V2, S1, and M1. Two additional Kruskal-Wallis independent-sample tests were used to compare the distribution of (1) neuron and (2) cell surface densities in V1, V2, S1, and M1. Statistical significance was set at $p < 0.05$ for a two-sided test. Data were analyzed using IBM-SPSS software (IBMSPSS 23).

NeuN-IR in tissue sections

The intact RH of case 11-47 (*M. nemestrina*) was sectioned into ten series of 50-μm-thick frozen sections. One series of sections was processed for Nissl substance (with thionin) and another series was immunostained for NeuN (1:5,000; Millipore) to verify the tissue and staining quality in this study. Immunohistochemical procedures used have been described in detail previously (Balaram et al., 2014). Figure 3.1A shows Nissl-stained intact V1 and M1 sections that exemplify the typical laminar patterns of these cortical areas. Figure 3.1 B and C shows NeuN-IR in the same cortical areas and further confirms the typical laminar distribution of neurons in V1 and M1. The NeuN antibody darkly stained a variety of neuron types that can be verified by their structure, including the small granule neurons in V1 layer 4 (Fig. 3.1B) and large pyramidal neurons in M1 layer 5 (Fig. 3.1C). Figure 3.1 A and C show that the laminar organization of cortical areas is normal, and there is minimal-to-no evidence of background or staining artifact. This indicates that tissue conditions and preparation in this study were ideal for counting cells. Figure 3.1D visually confirms anti-NeuN immunolabeling of neuronal nuclei in homogenized neural tissue suspensions of V1 and M1 in the opposite hemisphere of the same individual (case 11-47, LH). The lack of background or artifact staining shows that the homogenization process did not result in broken or damaged nuclei that would interfere with

flow cytometry cell and neuron population estimates, and that NeuN-IR nuclei were specifically stained and easily distinguishable from nonneuronal nuclei.

Results

Cell and neuron numbers and densities by case

The total numbers of cells and neurons in the cerebral cortex of macaque monkeys varied minimally between the individuals of the macaque species examined. The total number of cells per cortical hemisphere ranged from 2.9 to 3.7 billion, while the total number of neurons narrowly varied with a range of 1.3–1.7 billion (summarized in Table 3.2). The cell and neuron densities of individual pieces, as well as the boundaries used to define V1, V2, S1, and M1 in each case, are shown in Figure 3.2 for cases where illustration was possible. The S1 region largely corresponds to area 3b, but some of areas 3a, 1, and 2 are likely within the region, and similarly some of area 3a may be in the M1 region. The V2 region does not include all of area V2, but is rather a more conservative estimate; tissue pieces anterior to the V2 boundary line are likely other secondary or tertiary visual areas. The average neuron and cell densities within each cortical area by case are represented in Figure 3.3 A and B, respectively, and include available data from two baboon cases (Young et al., 2013b) for comparison. Table 3.2 summarizes the average and regional densities within cases.

The LH of case 12-58 (excluding the frontal eye field used for another study) had a total surface area of 100.6 cm^2, a total gray matter mass of 25 g, and contained 3.7 billion cells, of which 1.7 billion were neurons (46%). The cortical cell and neuron densities were 37.6 million

Fig. 3.1 **Nissl- and NeuN-stained tissue in V1 and M1.** High-magnification images of NeuN-IR in areas V1 and M1 in *M. nemestrina* (case 11-47). Sections from V1 and M1 were stained for Nissl substance (with thionin) **(A)** to verify the quality of tissue used in this study. Sections from V1 **(B)** and M1 **(C)** were stained with NeuN to verify consistent labeling of neurons with the anti-NeuN antibody. Both the Nissl and NeuN labeling in tissue sections illustrate the typical laminar distribution characteristic of these two cortical areas. A comparison of the NeuN-IR sections in V1 and M1 clearly demonstrate that multiple neuron types are darkly stained and readily identifiable at high magnification, as V1 has a large layer 4 with densely packed granule cells, layer 4 in M1 is minimal but less densely packed, but large pyramidal cells are found throughout M1 layer 5. V1 and M1 tissue from the LH of the same individual was processed for the flow fractionator with the same anti-NeuN primary antibody **(D).** Nuclei were strongly and brightly labeled with both DAPI and NeuN. There is absence of background or debris in the samples, suggesting that our flow cytometry estimates contain minimal errors.

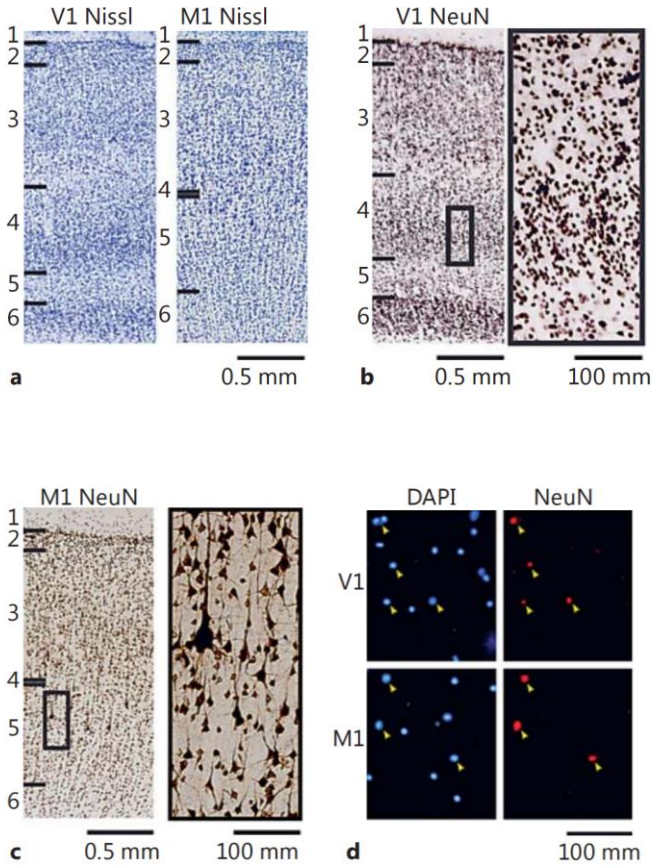

cells/cm^2 and 17.7 million neurons/cm^2. V1 was estimated to contain 629 million cells, of which 412 million were neurons (65%). The cell and neuron densities in V1 were 52.6 million cells/cm^2 and 34.7 million neurons/cm^2. Anterior to V1, V2 was estimated to contain 141 million cells, of which 97 million were neurons (69%). V2 contained cell and neuron densities of 41.1 million cells/cm^2 and 28 million neurons/cm^2. S1 was estimated to contain 184 million cells, of which 78 million were neurons (42%). S1 contained cell and neuron densities of 40.2 million cells/cm^2 and 17.1 million neurons/cm^2. Anterior to S1, M1 was estimated to contain a total of 202 million cells, of which 65 million were neurons (32%). M1 had cell and neuron densities of 32.9 million cells/cm^2 and 10.6 million neurons/cm^2.

Case 12-58 (RH) had a total surface area of 103.4 cm^2 and a total weight of 24.8 g. The RH was 2.7 cm^2 larger than LH, and weighed 0.8 g more, likely in part due to the removal of tissue including the frontal eye field from the LH for another study. As listed in Table 3.2, there are slight differences in cell and neuron numbers between the LH and the RH of case 12-58; despite having the slightly higher surface area, the RH contained approximately 365 million less cells and 138 million less neurons than the LH. This may reflect a loss of some of V1 of the RH during the dissection. The RH contained approximately 3.3 billion cells, of which nearly 1.6 billion were neurons (47%). The cell and neuron densities across cortex were approximately 32 million cells/cm^2 and 14.5 million neurons/cm^2, respectively. V1 was estimated to contain 641 million cells, of which 426 million (67%) were neurons. The cell and neuron densities in V1 were calculated to be 40.2 million cells/cm^2 and 26.9 million neurons/cm^2. V2 was estimated to contain 78 million cells, of which 52 million were neurons (67%). V2 contained cell and neuron densities of 32.1 million cells/cm^2 and 21.3 million neurons/cm^2. We estimated that there were a total of 133 million cells and 61 million neurons (46%) in S1. S1 had cell and neuron densities of

Fig. 3.2 **Distribution of neurons and cells across cortex in three macaque hemispheres.** Distribution of neurons **(A, C, E)** and cells **(B, D, F)**. Conservative boundaries for V1, V2, S1, and M1 cortical regions are outlined within each hemisphere. The dashed lines correspond to tissue pieces that are not part of the neocortex and are likely a part of piriform cortex. Thin white lines represent cuts in the tissue, while larger white spaces within the flattened cortex represent holes in the tissue that were necessary for the flattening process. In some cases, V1 was separated from the rest of cortex to prevent damage during the unfolding process.

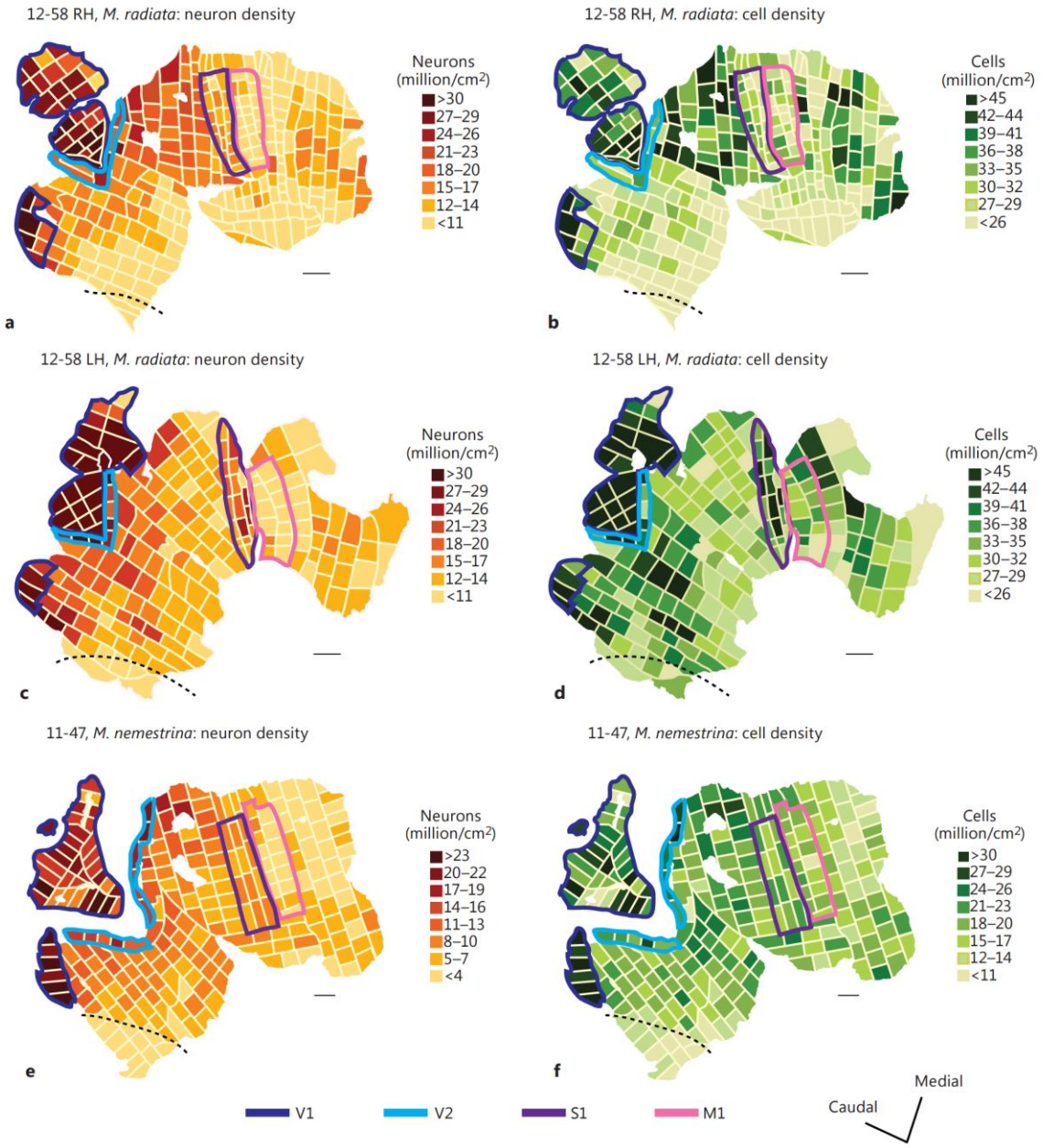

31.2 million cells/cm^2 and 14.3 million neurons/cm^2. M1 was estimated to contain a total of 146 million cells and 50 million neurons (34%). The M1 cell and neuron densities were 29.4 million cells/cm^2 and 10.1 million neurons/cm^2.

Case 11-47 had a total surface area of 151.8 cm^2 and a total weight of 33.2 g. The hemisphere contained approximately 3 billion cells, of which 1.3 billion were neurons (45%). There was an average of approximately 19.9 million cells/cm^2 and 9.3 million neurons/cm^2 across cortex. V1 was estimated to contain 506 million cells, of which 368 million (73%) were neurons. The cell and neuron densities in V1 were 25.2 million cells/cm^2 and 18.3 million neurons/cm^2. V2 was estimated to contain 114 million cells, of which 78 million were neurons (68%). V2 contained cell and neuron densities of 24.7 million cells/cm^2 and 16.8 million neurons/cm^2. We estimated that there were a total of 129 million cells in S1, of which 57 million were neurons (44%). S1 had cell and neuron densities of 19.6 million cells/cm^2 and 8.7 million neurons/cm^2. M1 was estimated to contain a total 180 million cells, of which 50 million were neurons (28%). The M1 cell and neuron densities were 18.2 million cells/cm^2 and 5.1 million neurons/cm^2.

Case 10-50 had a total surface area of 152.3 cm^2 and a total weight of 36.4 g. Cell and neuron estimates for this hemisphere are only available for V1, as the rest of the brain was not properly photographed during the dissection. The hemisphere contained 2.9 billion cells, of which 1.4 billion were neurons (48%). There was an average of 19.2 million cells/cm^2 and 9.4 million neurons/cm^2. V1 was estimated to contain 384 million cells, of which 263 million (68%) were neurons. The cell and neuron densities in V1 were 26.6 million cells/cm^2 and 18.2 million neurons/cm^2.

Table 3.2 Summary of cell and neuron data (averaged across all areas and regions of the cortex)

Case	Total cells in millions	Total neurons in millions	Total nonneurons in millions	G/N ratio	Mean cell density in million cells/cm^2	Mean neuron density in million neurons/cm^2
Summary of data averaged across all areas and regions of cortex						
12-58 LH	3,684 (8.11)	1,704 (5.08)	1,980 (4.94)	1.40 (0.79)	37.6 (9.88)	17.7 (8.99)
12-58 RH	3,319 (5.27)	1,566 (3.52)	1,753 (2.92)	1.44 (1.00)	32.0 (8.42)	14.9 (6.84)
11-47	2,960 (3.67)	1,344 (3.20)	1,616 (2.56)	1.64 (1.16)	19.9 (5.23)	9.26 (5.45)
10-50	2,887 (8.75)	1,400 (6.24)	1,487 (4.72)	1.29 (0.69)	19.2 (5.09)	9.37 (4.34)
Summary of data averaged across V1						
12-58 LH	629 (10.66)	412 (7.09)	217 (4.23)	0.61 (0.46)	52.6 (10.87)	34.7 (9.48)
12-58 RH	641 (5.92)	426 (4.04)	215 (2.27)	0.54 (0.24)	40.2 (6.71)	26.9 (6.21)
11-47	506 (5.39)	368 (4.11)	138 (1.56)	0.38 (0.12)	25.2 (7.39)	18.3 (5.56)
10-50	384 (10.63)	263 (6.76)	121 (4.08)	0.46 (0.07)	26.6 (2.25)	18.2 (1.21)
Summary of data averaged across V2						
12-58 LH	141 (5.73)	96.9 (4.18)	44.1 (1.67)	0.46 (0.07)	41.1 (7.82)	28.0 (5.13)
12-58 RH	78.3 (1.69)	52.1 (1.45)	26.2 (0.37)	0.51 (0.05)	32.1 (5.02)	21.3 (3.85)
11-47	114 (3.08)	77.8 (2.26)	36.2 (0.99)	0.48 (0.08)	24.7 (4.43)	16.8 (3.15)
Summary of data averaged across S1						
12-58 LH	184 (3.19)	78.1 (1.26)	105.9 (2.13)	1.39 (0.37)	40.2 (10.52)	17.1 (4.80)
12-58 RH	133 (2.53)	61.0 (1.11)	72.0 (1.49)	1.19 (0.29)	31.2 (4.88)	14.3 (2.11)
11-47	129 (1.91)	57.2 (0.95)	71.8 (1.18)	1.27 (0.23)	19.6 (2.30)	8.73 (1.35)
Summary of data averaged across M1						
12-58 LH	202 (4.45)	64.9 (1.55)	137.1 (3.64)	2.25 (0.86)	32.9 (7.04)	10.6 (3.23)
12-58 RH	146 (1.80)	50.2 (0.69)	95.8 (1.35)	1.99 (0.65)	29.4 (4.75)	10.1 (2.36)
11-47	180 (2.66)	49.7 (0.79)	130.3 (2.16)	2.71 (0.73)	18.2 (2.60)	5.06 (1.28)

Neuron density varies by cortical area

The Kruskal-Wallis test comparing the distributions of both neuron and cell densities in our sample revealed significant differences between different cortical areas (neurons: $\chi^2 = 121.3$, d.f. = 3, $p < 0.0001$, n = 241; cells: $\chi^2 = 16.3$, d.f. = 3, $p = 0.001$, n = 241). Most cortical areas were similar in cell density, and the only statistical difference detected was between V1 and M1 ($Z = 3.94$, $p < 0.001$). For neuron density, statistical differences were detected between all cortical areas, with the exception of V1 and V2 ($Z = 0.35$, $p = 0.728$). V1 is the most cell- and neuron-dense area of the cerebral cortex, and the total area ranged between 9.4 and 15% of cortex. Average V1 cell density ranged from 25.2 to 52.6 million cells/cm^2 in comparison to the

overall average range of 19.2–37.6 million cells/cm^2. V1 neuron density ranged from 18.2 to 34.7 million cells/cm^2 in comparison to the overall neuron density range of 9.3–17.7 million cells/cm^2. V2 neuron densities did not have as many extremely high values as V1, but most values were distributed among V1 values. V2 cell density ranged from 24.7 to 41.1 million cells/cm^2, and neuron density ranged from 16.8 to 28 million cells/cm^2. Area S1 contained moderate cell and neuron densities, as S1 is more cell and neuron dense than M1, but less densely packed than V1. S1 cell density ranged from 19.6 to 40.2 million cells/cm^2, while neuron density ranged from 8.7 to 17.1 million cells/cm^2. Primary motor cortex is the least neuron-dense area examined, where cell density ranged from 18.2 to 32.9 million cells/cm^2, and M1 neuron density in macaques ranged from 5.1 to 10.6 million cells/cm^2, which is approximately three times lower than the V1 range.

Fig. 3.3 **The mean neuron and cell surface densities by cortical area per case.** The mean neuron **(A)** and cell **(B)** surface densities. Cases 09-27 (*Papio hamadryas anubis/cyncephalus* hybrid) and 11-31 (*P. hamadryas anubis*) are included based on published data (Young et al., 2013b). **(C)** The mean G/N ratio within each cortical area did not vary greatly between cases of the same genus, but the G/N ratio was considerably lower in the baboon hemispheres across all cortical areas. Error bars = SEM.

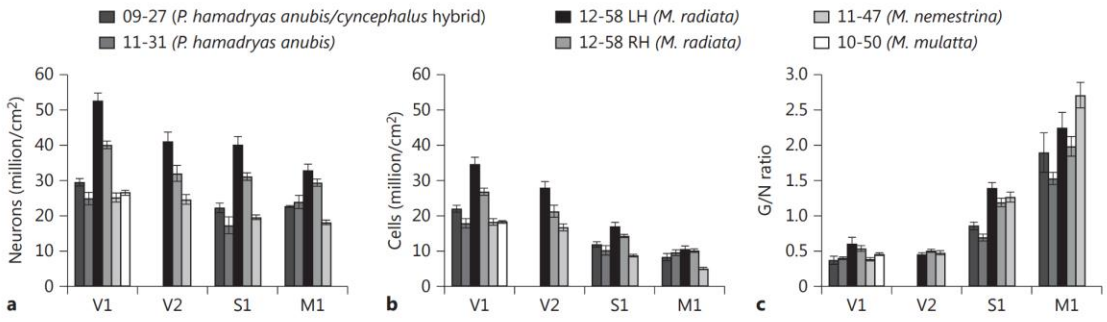

Neuron density versus the A-P dimension was plotted for each case (Fig. 3.4A), with the exception of case 10- 50, whose A-P coordinates were unknown since pieces were not photographed. A similar pattern within the A-P dimension emerges across cases, but there is considerable variation in the range of neuron densities. The neuron distributions follow the same posterior-to-anterior decrease in cortical neuron density that is typical in primates (Collins et al., 2010a; Cahalane et al., 2012; Young et al., 2013a; Young et al., 2013b), but average curve fit estimations suggest that the A-P gradient is not simply linear. Moving from posterior to anterior pieces, V1 values are the highest and are mixed with high V2 values, cortical pieces just anterior to these visual areas contain more moderate values, S1 contains pieces with high-to-moderate neuron densities, M1 contains pieces with lower-than-average neuron densities, and the most anterior pieces have moderate values. For neuron densities plotted by A-P location, we found that a cubic model provided the best correlation (adjusted $R^2 = 0.340$) compared to linear (0.279), exponential (0.244), or quadratic models (0.336). However, an exponential model resulted in the lowest root mean square error (RMSE) (0.253), while a linear model resulted in the highest RMSE (4.45×10^{13}), indicating the least useful fit for prediction. Figure 3.4B summarizes the distribution of neurons within each cortical area for all cases combined.

Other cell/neuron ratio varies by cortical area

To minimize the effects of variability in the raw cell and neuron density measures due to brain sizes in our small sample, we used G/N values to examine differences between cortical areas. The G/N values were binned across cases to examine the ratio in different cortical areas (Fig. 3.3C). Overall, the G/N ratio was consistent within cortical areas across all cases, and there was clear separation between M1, S1, and the two visual areas, V1 and V2, which were very similar. The Kruskal-Wallis test comparing the distributions of the G/N ratio between different

Fig. 3.4 **Distribution of neuron density and the G/N ratio across the A-P gradient. (A)** Distribution of neuron density across the flattened cortex (cases 12-58 LH, 12-58 RH, and 11-47) in a plot of density versus posterior to anterior location. The red dashed line indicates the curve estimation that most closely correlated with the data ($y = 2.79 \times 10^7 - 6.25 \times 10^7 x + 7.36 \times 10^7 x^2 - 2.99 \times 10^7 x^3$). **(B)** Distribution of neuron density within each area (V1, V2, S1, and M1) binned across cases in a plot of neuron density versus posterior to anterior location. **(C)** Distribution of the G/N ratio across each flattened cortex (cases 12-58 LH, 12-58 RH, and 11-47) in a plot of the G/N ratio versus posterior to anterior location. The red dashed line indicates the curve estimation that most closely correlated with the data ($y = 0.58^{(1.61x)}$). **(D)** Distribution of the G/N ratio within each cortical area in a plot of G/N ratio versus posterior to anterior location. The arrowheads identify two outlier pieces in the V1 region with higher G/N ratios that may have included some white matter. The dashed boxes in **(C)** and **(D)** outline tissue pieces containing a high G/N ratio in posterior cortex, and they correspond to the pieces outlined in Figure 3.2 from piriform cortex.

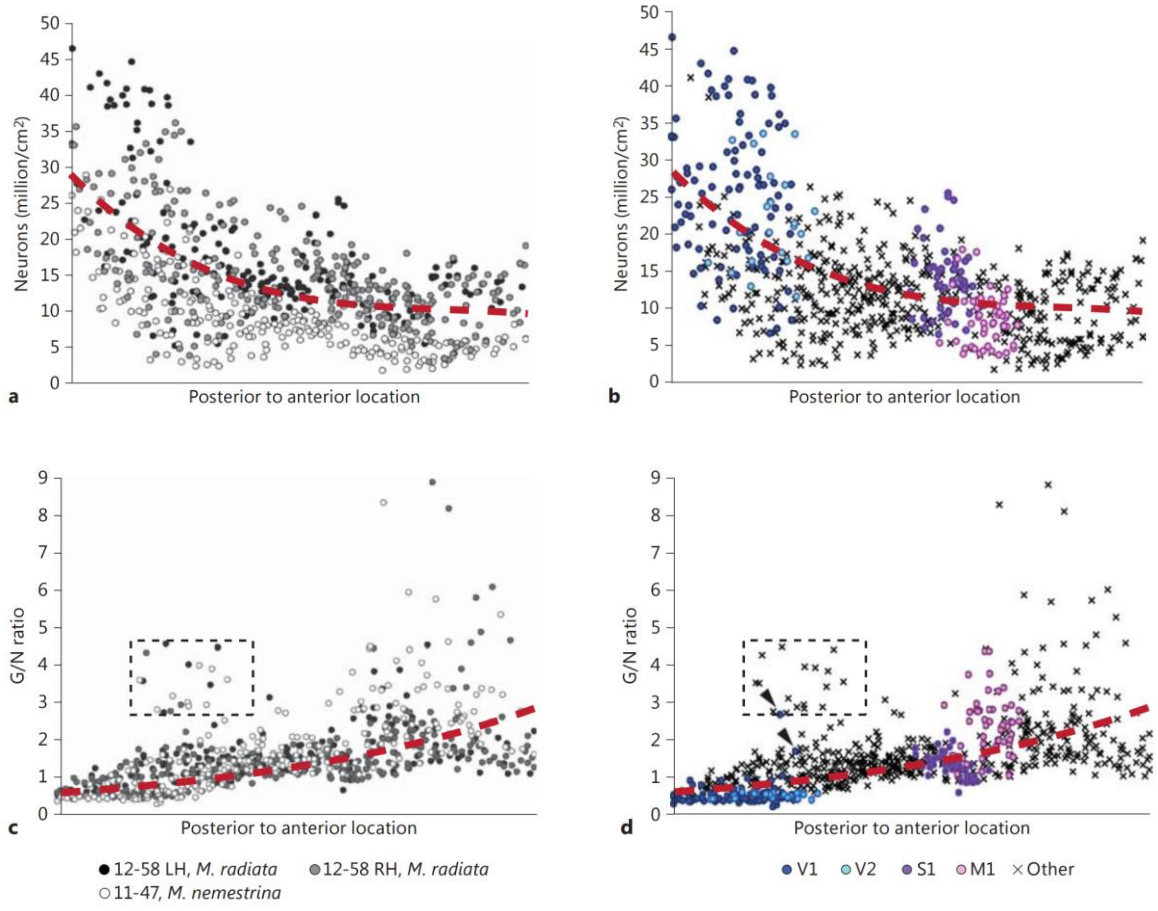

cortical areas revealed significant differences (χ^2= 170, d.f. = 3, p < 0.001, n = 241). However, the pairwise comparison between V1 and V2 was the exception without a statistical difference in the G/N ratio (Z = –0.69, p = 0.489). The average G/N ratio in V1 ranged from 0.38 to 0.61, while it similarly varied from 0.46 to 0.51 in V2. Two outlier pieces in the V1 region with higher G/N ratios (see arrowheads in Fig. 3.4D) may have included some white matter. The average G/N ratio was doubled from V1 to S1, with average values within cases ranging from 1.19 to 1.39 in S1, and the pairwise comparison supported statistical differences between the distributions (Z = –8.31, p < 0.001). G/N ratios for V2 versus S1 (Z = –5.01, p < 0.001) resembled the relationship between V1 and S1. The G/N ratio in M1 was the highest and the range was the most variable, with the average four times higher than the average V1 ratios (Z = –11.75, p < 0.001), and values ranging from 1.99 to 2.71. Similarly, the distributions of the G/N ratio in V2 compared to M1 (Z = –7.32, p < 0.001) resemble the relationships listed for V1, and the pairwise comparison also supported statistical differences between M1 and S1 (Z = –2.19, p = 0.021). While not included in the statistical analysis, the G/N ratios from the two baboons followed trends by area comparable to the macaques studied. However, the average G/N ratios for the two baboons tended to be slightly lower in each cortical area in comparison to the macaque brains (case 09-27: V1 = 0.37, S1 = 0.86, M1 = 1.90; case 11-31: V1 = 0.40, S1 = 0.69, M1 = 1.53).

The A-P plot of the G/N ratio across each case showed more similar values between cases at each A-P coordinate (Fig. 3.4C) compared to neuron densities across the A-P dimension (Fig. 3.4A). For G/N ratios plotted by A-P location, we found that an exponential model provided the best correlation (adjusted R^2= 0.434) compared to linear (0.276), cubic (0.279), or quadratic models (0.277). The exponential model resulted in the best RMSE (0.224), and the

linear model had the largest RMSE (0.744). Figure 3.4D summarizes the distribution of G/N ratios within each cortical area for all cases combined.

Discussion

Here we provide estimates of the total number and density of cells and neurons for multiple pieces of tissue across the cortical sheet, and for four specific areas within the macaque cortex. Comparisons are made with previously published data collected from baboons in a comparable way. Our findings are consistent with previous observations that primary visual cortex and early extrastriate visual areas tend to have higher-than-average neuron and cell densities while motor cortex has lower-than-average densities (Collins et al., 2010a; Collins, 2011; Young et al., 2013b; Collins et al., 2016). These results suggest that this distinct architecture exists across most or all anthropoid primates. While the average cell and neuron densities decrease with increasing brain size across cases, the average cellular composition across the brain remains relatively consistent between cases, and the total number of cells and neurons varies little among cases. The calculated G/N ratios provide clear distinctions between cortical areas M1 and S1 versus visual areas V1 and V2 (Fig. 3.3C).

The overall pattern of cell and neuron densities, and the sizes of cortex and cortical area

In all cases, there was large variation in neuron and cell densities across the many pieces of cortex that were sampled. As the boundaries of the areas were estimates, the densities and especially the values of total size and total number of neurons and cells are not exact and may be underestimates. Likewise, because of small, but variable amounts of missing cortex due to the dissection and flattening process, the values of the total sizes of cortex and total numbers of

neurons and cells are likely underestimates. Yet, some of the results were so robust that clear conclusions are possible. First, as previously reported for various anthropoid primates (Collins et al., 2010a; Young et al., 2013b), neuron densities were highest in primary and secondary visual cortexes. Other visual areas near or adjoining V2 also had high neuron densities, indicating that extrastriate visual areas near V1 all have higher than average neuron densities. Primary somatosensory cortex also had higher than average packing of neurons, while primary motor cortex had low values. To some extent, premotor cortex also had low values, as did regions of ventral frontal cortex and the ventral temporal lobe. A region of dorsolateral prefrontal cortex had moderately high neuron densities. As these differences in neuron densities relate to functional roles, it will be important to obtain more precise estimates of neuron numbers relative to areal boundaries and sizes in the future.

The observed variance in neuron densities across our macaque cases may relate in part to differences in brain size (Table 3.2). For example, case 12-58 LH (*M. radiata*), which has the expected lowest cortical weight and cortical surface area (24.8 g, 100.6 cm^2) [Fooden, 1975, 1981; Schwartz and Kemnitz, 1992], contains the highest cell and neuron densities. Cases 11-47 and 10-50, with 50% greater cortical weights (11-47: 33.2 g; 10-50: 36.4 g) and surface areas (11-47: 151.8 cm^2; 10-50: 152.3 cm^2), contain similar total and areal cell and neuron densities to each other (Table 3.2). However, cases 11-47 and 10-50 contain slightly less overall neurons compared to case 12-58. These two factors, the total number of neurons and brain size, may explain the comparatively higher neuron density for case 12-58.

Patterns across the A-P gradient

All cases examined followed the same pattern of cell and neuron distributions within cortical areas despite our finding that absolute values varied across individuals. Moving from posterior to anterior tissue beginning at V1, the results indicate that (1) V1 has the highest neuron density; (2) there is a graded decline in neuron density across cortex anterior to V1; (3) somatosensory cortex represents a second peak in neuron density, and (4) just anterior to somatosensory cortex there is another slight decline in neuron density (motor cortex), but then neuron density increases again in the more anterior prefrontal cortical region. The region that represents much of this rise in neuron density is part of prefrontal granular cortex (Preuss and Goldman-Rakic, 1991). However, the rise in neuron density in this region of prefrontal cortex appears to be more distinct from surrounding areas in the chimpanzee cortex (Collins et al., 2016). This A-P pattern of neuron density suggests there is a common blueprint of cortical organization between primates, in which there are consistent differences in cell and neuron densities in homologous areas and regions, speculatively due to information-processing demands. An overall A-P gradient of increasing neuron densities has been suggested as a basic pattern derived from a developmental gradient in neuron production (Cahalane et al., 2012), and such a neuron-generating gradient could account for much of the pattern seen in our data. However, the gradual A-P gradient is a result of summing all cortical tissue pieces in the single flattened plane; clear borders emerge between cortical areas when pieces within individual cortical areas are summed. These sharp changes in neuron densities at areal borders, and increased neuron densities in S1 and prefrontal granular cortex, likely depend on factors in addition to the developmental gradients. An overall lateral-to-medial gradient is also a factor to consider, as the developing cortical plate decreases in thickness in the lateral-to-medial direction

(O'Leary et al., 2007). However, it is important to consider the clearly different functional roles of areas with high and low neuron densities, and both the generation and the loss of neurons can influence neuron densities in adults (Rakic et al., 1991; Dehay et al., 2001).

Comparisons with other species

The use of the same procedures for flattening cortex and obtaining cell and neuron counts for many small sections of the cortical sheet in several recent studies on primates allows for a number of potentially useful and informative comparisons. First, both average neuron density and the overall proportion of neurons are variable across species. Approximately 47% of all cells were neurons across macaque cortex, which is slightly lower than the overall proportion in baboons (51 and 52%) (Young et al., 2013b) but higher than in chimpanzees (39%) (Collins et al., 2016). The average cell and neuron densities in macaque cortex (cells: 27.2 million/cm^2, neurons: 12.8 million/cm^2) are slightly higher than the average densities reported in baboon (cells: 21.9 million/cm^2, neurons: 11.3 million/cm^2) or chimpanzee cortex (cells: 26.2 million/cm^2, neurons: 10.4 million/cm^2). However, the larger differences in cell and neuron densities between macaques (cases 12-58, 11-47, and 10-50) suggest that observations on more individuals might reveal more variation.

The slight variability in overall neuron density across species is also apparent in specific cortical areas. In all primates examined, V1 unsurprisingly had the highest neuron densities, and M1 contained the lowest neuron densities (Collins et al., 2010a; Collins, 2011; Young et al., 2013b). The average cell and neuron densities in macaque V1 (cells: 36.1 million/cm^2, neurons: 24.5 million/cm^2) are higher than the average densities found in V1 baboon (cells: 27.2 million/cm^2, neurons: 19.9 million/cm^2) or chimpanzee cortex (cells: 32 million/cm^2, neurons: 21

million/cm^2). Although our estimates of V1 may be an underestimation, the measured surface area of flattened V1 in macaques (9.4–15% of cortex) is consistent with previous studies in baboons (14–15.9%) and chimpanzees (10%).

Furthermore, our finding that the G/N ratios within different cortical areas across all four macaque brains are similar suggests that the variation in packing densities is due to brain size or total number of cells and neurons, and not a counting error. Areas of low neuron density contain larger neurons overall (Friede, 1954; Hawkins and Olszewski, 1957; Tower and Young, 1973) that require more glia per neuron; therefore, areas of low neuron density generally have a higher G/N ratio and the opposite is true for areas of high neuron density. In this respect, the G/N ratio can serve as a useful tool when comparing brains of different sizes (that are closely related) but similar in their overall neuronal composition (e.g., neuron and glial cell size). The average G/N ratio for each macaque brain (case 12-58 LH = 1.40/RH = 1.44, case 11-47 = 1.64, case 10-50 = 1.29) is slightly higher than what has been reported in flattened cortex of baboons (case 09-27 = 1.19, case 11-31 = 1.16) (Young et al., 2013b) and lower than the reported values for one chimpanzee brain (1.86) (Collins et al., 2016). The average G/N ratios in macaque V1 (range = 0.38 – 0.61) is between the average G/N ratios described in V1 of baboons (0.37, 0.40) and a chimpanzee (0.58). The G/N ratios in macaque areas S1 (range = 1.19 – 1.39) and M1 (range = 1.99 – 2.71) are slightly higher than those reported in two baboons (S1 = 0.86 – 0.69; M1 = 1.90–1.53) and more similar to what has been described in chimpanzee neocortex (S1 = 1.25, M1 = 2.96). However, it is unclear if the G/N ratios here reveal any true differences between these primate species. S1 and M1 are more challenging than V1 to identify without electrophysiological data, and it is likely for each species that the M1 region includes some cortex from area 3a and the S1 region includes cortex from areas 3a, 1, and 2. There are

differences in brain size between macaques, baboons, and chimpanzees, but assuming there are no significant changes in average neuron size (Harrison et al., 2002), we would not expect the G/N ratio to vary much.

Nonuniformity across the cortical sheet

The results of a highly influential study three decades ago led to the conclusion that neuron densities did not vary much across cortical areas and species, with the exception that neuron density doubled in V1 of macaque monkeys (Rockel et al., 1980; Carlo and Stevens, 2013). Such findings may have been the result of under-sampling (Cahalane et al., 2012; Herculano-Houzel et al., 2013). Our estimates of neuron numbers using flow and isotropic fractionation from the current study and previous research in prosimians, other Old World monkeys, and hominins (Collins et al., 2010a; Collins, 2011; Young et al., 2013b; Collins et al., 2016) have provided evidence for fluctuations in neuron density in areas anterior to V1. The current methodology has proven to produce results that are not significantly different from those of other methodologies used to count cell and neuron numbers (Bahney and von Bartheld, 2014; Miller et al., 2014), and these ongoing studies provide many more estimates of neuron densities from across the entire cortical sheet. It has been previously reported in other primate species using this methodology that M1 contains lower neuron densities (Young et al., 2013a), and studies on rodents and cats have also reported that M1 contains lower neuron densities than other areas of cortex (Beaulieu and Colonnier, 1989; Allman, 1994; Skoglund et al., 1996; Young et al., 2013a). In the present study, we found that the number of neurons beneath one mm^2 of cortical surface is variable between cortical areas across cases. As first reported three decades ago, primary visual areas have the highest densities of neurons, but secondary visual areas, somatosensory areas, and some of prefrontal cortex also contain higher-than-average neuron

densities, while motor areas contain lower-than-average neuron densities. Similarly, the G/N ratio range is significantly different between some cortical areas, suggesting that the number as well as the size of neuronal and glial cells, and therefore density, differs depending on the functional requirements of that particular cortical area.

Functional implications

Neuron density and average neuron size are inversely related (Herculano-Houzel, 2014; Herculano-Houzel et al., 2014), as larger neurons take up more space and are surrounded by more glial cells which do not vary much in size. Thus, as neuron densities decrease, glial cell densities increase. This inverse relationship is reflected in the G/N ratio that is high in motor cortex and low in V1. These differences likely reflect the different functional roles of neurons in M1, V1, and other cortical areas. Smaller neurons, such as granule cells in layer 4 of V1, are thought to preserve information provided by only a few driving inputs and serve to accurately relay this information from the lateral geniculate nucleus to other cortical areas (Elston et al., 1996; Kaas, 2000; Srinivasan et al., 2015). Larger neurons, such as Betz cells in layer 5 of motor cortex, require more glial support, have larger dendritic arbors (Elston, 2002), and integrate information from many sources. The G/N ratio increases in areas where there are fewer, but larger neurons, and this is seen in areas such as M1, which in macaques contains on average a G/N ratio that is four times higher compared to V1. Other cortical areas vary in neuron densities, and thereby average neuron size, and this variation likely reflects their differing functional roles.

REFERENCES

Allman JM (1994) Brain and lifespan in catarrhine primates.

Allman JM, McLaughlin T, Hakeem A (1993) Brain weight and life-span in primate species. Proc Natl Acad Sci U S A 90:118-122.

Azevedo FA, Carvalho LR, Grinberg LT, Farfel JM, Ferretti RE, Leite RE, Jacob Filho W, Lent R, Herculano-Houzel S (2009) Equal numbers of neuronal and nonneuronal cells make the human brain an isometrically scaled-up primate brain. J Comp Neurol 513:532-541.

Bahney J, von Bartheld CS (2014) Validation of the isotropic fractionator: comparison with unbiased stereology and DNA extraction for quantification of glial cells. J Neurosci Methods 222:165-174.

Balaram P, Young NA, Kaas JH (2014) Histological features of layers and sublayers in cortical visual areas V1 and V2 of chimpanzees, macaque monkeys, and humans. Eye Brain 2014:5-18.

Bass N, Hess H, Pope A, Thalmeier C (1971) Quantitative cytoarchitectonic distribution of neurons, glia, and DNA in rat cerebral cortex. J Comp Neurol 143:481-490.

Beaulieu C, Colonnier M (1989) Number of neurons in individual laminae of areas 3B, 4 gamma, and 6a alpha of the cat cerebral cortex: a comparison with major visual areas. J Comp Neurol 279:228-234.

Cahalane DJ, Charvet CJ, Finlay BL (2012) Systematic, balancing gradients in neuron density and number across the primate isocortex. Front Neuroanat 6:28.

Campi KL, Collins CE, Todd WD, Kaas J, Krubitzer L (2011) Comparison of area 17 cellular composition in laboratory and wild-caught rats including diurnal and nocturnal species. Brain Behav Evol 77:116-130.

Carlo CN, Stevens CF (2013) Structural uniformity of neocortex, revisited. Proc Natl Acad Sci U S A 110:1488-1493.

Christensen JR, Larsen KB, Lisanby SH, Scalia J, Arango V, Dwork AJ, Pakkenberg B (2007) Neocortical and hippocampal neuron and glial cell numbers in the rhesus monkey. Anat Rec (Hoboken) 290:330-340.

Collins CE (2011) Variability in neuron densities across the cortical sheet in primates. Brain Behav Evol 78:37-50.

Collins CE, Airey DC, Young NA, Leitch DB, Kaas JH (2010a) Neuron densities vary across and within cortical areas in primates. Proc Natl Acad Sci U S A 107:15927-15932.

Collins CE, Turner EC, Sawyer EK, Reed JL, Young NA, Flaherty DK, Kaas JH (2016) Cortical cell and neuron density estimates in one chimpanzee hemisphere. Proc Natl Acad Sci U S A 113:740-745.

Collins CE, Young NA, Flaherty DK, Airey DC, Kaas JH (2010b) A rapid and reliable method of counting neurons and other cells in brain tissue: a comparison of flow cytometry and manual counting methods. Front Neuroanat 4:5.

de Sousa AA, Sherwood CC, Schleicher A, Amunts K, MacLeod CE, Hof PR, Zilles K (2010) Comparative cytoarchitectural analyses of striate and extrastriate areas in hominoids. Cereb Cortex 20:966-981.

Dehay C, Savatier P, Cortay V, Kennedy H (2001) Cell-cycle kinetics of neocortical precursors are influenced by embryonic thalamic axons. J Neurosci 21:201-214.

Elston GN (2002) Cortical heterogeneity: implications for visual processing and polysensory integration. J Neurocytol 31:317-335.

Elston GN, Rosa MG, Calford MB (1996) Comparison of dendritic fields of layer III pyramidal neurons in striate and extrastriate visual areas of the marmoset: a Lucifer yellow intracellular injection. Cereb Cortex 6:807-813.

Fooden J (1975) Taxonomy and evolution of liontail and pigtail macaques (Primates: Cercopithecidae). Fieldiana: Zool 67:1-169.

Fooden J (1981) Taxonomy and evolution of the Sinica group of macaques: 2. Species and subspecies accounts of the Indian bonnet macaque, Macaca radiata. Fieldiana Zool ns 1-52.

Friede R (1954) Der quantitative Anteil der Glia an der Cortex entwicklung. Acta Anat 20:290-296.

Gharbawie OA, Stepniewska I, Kaas JH (2011) Cortical connections of functional zones in posterior parietal cortex and frontal cortex motor regions in new world monkeys. Cereb Cortex 21:1981-2002.

Hakeem A, Rodriguez-Sandoval G, Jones M, Allman JM (1996) Brain and life span in primates. New York: Academic Press.

Harrison KH, Hof PR, Wang SS (2002) Scaling laws in the mammalian neocortex: does form provide clues to function? J Neurocytol 31:289-298.

Hawkins A, Olszewski J (1957) Glia/nerve cell index for cortex of the whale. Science 126:76-77.

Herculano-Houzel S (2014) The glia/neuron ratio: how it varies uniformly across brain structures and species and what that means for brain physiology and evolution. Glia 62:1377-1391.

Herculano-Houzel S, Collins CE, Wong P, Kaas JH, Lent R (2008) The basic nonuniformity of the cerebral cortex. Proc Natl Acad Sci U S A 105:12593-12598.

Herculano-Houzel S, Lent R (2005) Isotropic fractionator: a simple, rapid method for the quantification of total cell and neuron numbers in the brain. J Neurosci 25:2518-2521.

Herculano-Houzel S, Manger PR, Kaas JH (2014) Brain scaling in mammalian evolution as a consequence of concerted and mosaic changes in numbers of neurons and average neuronal cell size. Front Neuroanat 8:77.

Herculano-Houzel S, Watson C, Paxinos G (2013) Distribution of neurons in functional areas of the mouse cerebral cortex reveals quantitatively different cortical zones. Front Neuroanat 7:35.

Kaas JH (2000) Why is brain size so important: Design problems and solutions as neocortex gets bigger or smaller. Brain and Mind 1.

Miller DJ, Balaram P, Young NA, Kaas JH (2014) Three counting methods agree on cell and neuron number in chimpanzee primary visual cortex. Front Neuroanat 8:36.

O'Leary DD, Chou SJ, Sahara S (2007) Area patterning of the mammalian cortex. Neuron 56:252-269.

Pakkenberg B, Gundersen HJ (1997) Neocortical neuron number in humans: effect of sex and age. J Comp Neurol 384:312-320.

Preuss TM, Goldman-Rakic PS (1991) Myelo- and cytoarchitecture of the granular frontal cortex and surrounding regions in the strepsirhine primate Galago and the anthropoid primate Macaca. J Comp Neurol 310:429-474.

Rakic P, Suner I, Williams RW (1991) A novel cytoarchitectonic area induced experimentally within the primate visual cortex. Proc Natl Acad Sci U S A 88:2083-2087.

Rockel AJ, Hiorns RW, Powell TP (1980) The basic uniformity in structure of the neocortex. Brain 103:221-244.

Schwartz SM, Kemnitz JW (1992) Age- and gender-related changes in body size, adiposity, and endocrine and metabolic parameters in free-ranging rhesus macaques. Am J Phys Anthrop 89:109-121.

Sherwood CC, Hof PR (2007) The evolution of neuron types and cortical histology in apes and humans. In: The Evolution of Nervous Systems, vol. 4 (Preuss, T. M. and Kaas, J. H., eds), pp 355-378 Oxford: Academic Press.

Skoglund TS, Pascher R, Berthold CH (1996) Heterogeneity in the columnar number of neurons in different neocortical areas in the rat. Neurosci Lett 208:97-100.

Srinivasan S, Carlo CN, Stevens CF (2015) Predicting visual acuity from the structure of visual cortex. Proc Natl Acad Sci U S A 112:7815-7820.

Stephan H, Frahm H, Baron G (1981) New and revised data on volumes of brain structures in insectivores and primates. Folia Primatol (Basel) 35:1-29.

Tower DB, Young OM (1973) The activities of butyrylcholinesterase and carbonic anhydrase, the rate of anaerobic glycolysis, and the question of a constant density of glial cells in cerebral cortices of various mammalian species from mouse to whale. J Neurochem 20:269-278.

Young NA, Collins CE, Kaas JH (2013a) Cell and neuron densities in the primary motor cortex of primates. Front Neural Circuits 7:30.

Young NA, Flaherty DK, Airey DC, Varlan P, Aworunse F, Kaas JH, Collins CE (2012) Use of flow cytometry for high-throughput cell population estimates in brain tissue. Front Neuroanat 6:27.

Young NA, Szabo CA, Phelix CF, Flaherty DK, Balaram P, Foust-Yeoman KB, Collins CE, Kaas JH (2013b) Epileptic baboons have lower numbers of neurons in specific areas of cortex. Proc Natl Acad Sci U S A 110:19107-19112.

CHAPTER 4

Optic nerve, superior colliculus, visual thalamus, and primary visual cortex of the northern elephant seal (*Mirounga angustirostris*) and California sea lion (*Zalophus californianus*)

The following chapter was accepted for publication under the same title in the Journal of Comparative Neurology by Emily Turner, Eva Sawyer, and Jon Kaas; accepted February 9th, 2017

Abstract

The northern elephant seal (*Mirounga angustirostris*) and California sea lion (*Zalophus californianus*) are members of a diverse clade of carnivorous mammals known as pinnipeds. Pinnipeds are notable for their large, ape-sized brains, yet little is known about their central nervous system. Both the northern elephant seal and California sea lion spend most of their lives at sea, but each also spends time on land each year to breed and give birth. These unique coastal niches may be reflected in specific evolutionary adaptations to their sensory systems. Here we report on components of the visual pathway in these two species. We found evidence for two classes of myelinated fibers within the pinniped optic nerve, those with thick myelin sheaths (elephant seal: 9%, sea lion: 7%) and thin myelin sheaths (elephant seal: 91%, sea lion: 93%). To investigate the architecture of the lateral geniculate nucleus, superior colliculus, and primary visual cortex, we processed brain sections from elephant seal and sea lion pups for Nissl

substance, cytochrome oxidase and vesicular glutamate transporters. As in other carnivores, the dorsal lateral geniculate nucleus consisted of three main layers, A, A1, and C, while each superior colliculus similarly consisted of seven distinct layers. The sea lion visual cortex is located at the posterior side of cortex between the upper and lower banks of the postlateral sulcus, while the elephant seal visual cortex extends far more anteriorly along the dorsal surface and medial wall. These results are relevant to comparative studies related to the evolution of large brains.

Introduction

Pinnipeds are a diverse clade of mammals and consist of three families: Odobenidae (walrus), Otariidae (eared seals: sea lions and fur seals), and Phocidae (earless seals: true seals). These mammals belong to the order Carnivora and while they are most closely related to the Ursidae family that consists of eight bear species, they are also distantly related to dogs, cats, and ferrets. Pinnipeds spend most of their lives in water, but also a significant amount of time on land to breed and give birth, in contrast to other large-brained marine mammals, such as cetaceans, that are obligately aquatic.

In recent years, there has been increased interest in the sensory systems of pinnipeds, for these species have unique adaptations to both terrestrial and aquatic environments. All pinnipeds have distinctive mystacial vibrissae. The California sea lion (CSL) and northern elephant seal (NES) use their whiskers primarily for prey detection (Dehnhardt et al., 2001; Glaser et al., 2011). In recent experiments, Glaser et al. (2011) found that sea lions can follow hydrodynamic trails while blindfolded with the use of their vibrissae, but fail at this task with vision alone when

their vibrissae are blocked with a muzzle. Similar studies in harbor seals have shown that these mammals can track the direction of hydrodynamic trail from an artificial rubber fin with 90% accuracy after a five second delay and 70% accuracy after a 35 second delay (Wieskotten et al., 2010). Others have reported how sea lions and seals can differentiate objects or wakes by shape and size with their whiskers, or complete complex sensorimotor tasks (Dehnhardt et al., 1998; Wieskotten et al., 2011; Milne and Grant, 2014). These findings suggest that the pinniped somatosensory system may play a dominant role over the visual system when it comes to evolutionarily important behaviors such as hunting.

A typical NES will spend approximately nine to ten months of the year at sea, with 90% of that underwater, and can perform dives lasting up to 119 minutes in duration at depths greater than 1500 meters (Le Boeuf et al., 1988; Stewart and DeLong, 1995). Even on land, elephant seals have many sleep apnea events, with breath-holds lasting up to 25 minutes (Blackwell and Le Boeuf, 1993). Given these remarkable respiratory capabilities and the elevated endogenous carbon monoxide levels that these animals balance with large oxygen stores, most current research with the NES concerns the use of this species as a model for coping with oxidative stress. Very little is known about the sensory systems of the NES. Given the depths to which these mammals can dive in search of prey (Hassrick et al., 2007; Kuhn et al., 2009) and the relative lack of light at these deep-sea locations, except for bioluminescence, visual cues must be limited during these dives. McGovern et al. (2015) found that the number of myelinated axons innervating each elephant seal vibrissae is five to eight times more than terrestrial mammals, supporting the idea that these animals have highly sensitive vibrissae that are useful in detecting prey at these depths. However, there is support for the hypothesis that elephant seals rely in part on their vision, as do most other carnivores. Pupil size in the NES can adapt from terrestrial

daylight conditions to the darker conditions at their foraging depths in six minutes, which is less than half the time it would take for a CSL or human to adapt to that change (Levenson and Schusterman, 1999).

Despite clear evidence that the somatosensory system in pinnipeds is highly specialized for many of their behaviors, there also is anatomical evidence that the visual systems of pinnipeds have evolved anatomical adaptations as a result of their amphibious environment. Levenson et al. (2006) reported that the deep-diving NES is the only pinniped species studied that has rods characteristic of an adaptation for marine life, with a spectral peak sensitivity of 487 nm in contrast to 499 or 501 nm for other pinniped species and closely-related terrestrial mammals (e.g. sea otters, polar bears). This "blue-shifted" trend has been reported in other deep sea mammals and fish (McFarland, 1971; Bowmaker, 1995; Hunt et al., 1996; Bowmaker, 1998; Fasick and Robinson, 2000) suggesting that it is related to the necessity for increased sensitivity to blue-green wavelengths of light that are present in deeper parts of the ocean. The entire pinniped clade may lack the *S*-cone type, the cone that transduces short wavelengths, in contrast to the existence of the *S*-cone in sea otters and polar bears (Peichl et al., 2001; Levenson et al., 2006). Many cetaceans also do not have *S*-cones (Levenson and Dizon, 2003), leading to speculation that re-adaptation from a terrestrial to an aquatic environment is responsible for the convergent loss of *S*-cones in these two distinct mammalian groups (Griebel and Peichl, 2003).

Other anatomical features of the pinniped eye are clear examples of adaptations for an amphibious environment. In deep-diving animals, such as the NES, pupil size can widely range from 422 mm^2 in dark adapted, deep sea conditions, to only 0.9 mm^2 in light adapted conditions (Levenson and Schusterman, 1997). The CSL inhabits more shallow and murky waters, and has only been reported at maximum depths near 274 m (Feldkamp et al., 1989); their pupil size range

is more limited, varying from 8.4 mm^2 to 220 mm^2. Furthermore, the lower limit of adjustment to varying light levels in the CSL represents only 22.1% of maximum pupil size in the NES (Levenson and Schusterman, 1997), which suggests that the visual system of the NES is better adapted to function in light-limited conditions. Most pinnipeds have an aquatically adapted spherical lens that makes their eyes emmetropic in water, but due to the large refractive power of the cornea these mammals would be myopic in air. To address this problem, the CSL and most other pinnipeds have a flat region of the cornea that is approximately 6-10 mm in diameter that serves as an emmetropic region where refraction is identical in water and air (Wilson, 1970; Dawson et al., 1987; Mass and Supin, 1992; 2003; 2007). It has also been suggested that there are accommodation mechanisms in play that might alter the physical structure of the lens, but these precise capabilities are still unknown.

The tapetum lucidum, or "eye-shine" layer, is intraocular reflective tissue which serves to enhance scotopic vision by providing retinal cells a second opportunity for photon-photoreceptor stimulation (Ollivier et al., 2004), and it has been described in many species, including pinnipeds and cetaceans, that rely upon vision in dim environments (Nagy and Ronald, 1970; Jamieson and Fisher, 1971; Nagy and Ronald, 1975; Dawson, 1980; Braekevelt, 1986; Miller et al., 2010). The medial interlaminar nucleus (MIN), a division of the lateral geniculate nucleus (LGN), represents a region of the retina that includes the tapetum in the brains of related terrestrial carnivores (i.e., raccoon, weasel, and fox), but has not been characterized in any pinniped brain (Sanderson, 1974; Lee et al., 1984). Topographic maps of retinal ganglion cell distributions in multiple pinniped species consistently show an area with higher than average ganglion cell densities (Mass and Supin, 1992; Welsch et al., 2001; Mass and Supin, 2003; 2005), comparable to the fovea or area centralis in primates (Rodieck, 1973), or visual streak in terrestrial carnivores

(Stone, 1965). This high-density area is within the binocular portion of the retina, which provides the highest visual resolution.

Despite an increasing amount of knowledge regarding the anatomical structure and visual capabilities of pinnipeds, surprisingly little is known about how sensory information is processed by their brains. Recently, the first comprehensive report of the CSL somatosensory system revealed that these brains share fundamental components with many other mammals, such as a well-developed trigeminal system that allows for the representation of whisker modules in the brainstem and thalamus, as in mice (Sawyer et al., 2016). Similarly, while the CSL has a highly gyrified neocortex, its somatosensory cortex has distinct sulcal homologies with other terrestrial carnivores that remain in consistent locations across clades. Both the CSL and NES brains contain more secondary folds and sulci than related terrestrial carnivores, which makes them more difficult to accurately characterize in terms of neocortical components (Montie et al., 2009). Montie et al. (2009) were the first group to provide an anatomically labeled MRI atlas of the CSL brain that has been helpful for comparative studies, but there has been no similar research regarding the neuroanatomy or processing of sensory information in the NES to date. Basic information regarding the organization of their visual thalamus, superior colliculus, primary visual cortex, and other related visual areas remains unknown, largely due to difficulties in attaining tissue and working with such large specimens. In cats, the three physiological retino-geniculo-cortico streams are the X-, Y-, and W- pathways, which are comparable to the parvocellular, magnocellular, and koniocellular streams in primates (Sherman, 1985; Casagrande and Norton, 1991; Hendry and Reid, 2000; Sherman and Guillery, 2004). Pinniped species likely have similar parallels streams as seen in other carnivores.

To address unanswered questions regarding the organization of the visual systems in the CSL and the NES, we used various immunohistochemical markers and histological stains to examine the optic nerve, superior colliculus, visual thalamus, and primary visual cortex of both pinniped species.

Materials and Methods

Animals

Images of live animals were taken on beaches in Año Nuevo State Park (San Francisco, CA) and La Jolla Cove (San Diego, CA). Tissue samples were collected from two NES (*Mirounga angustirostris*) pups (both male, ages approximately two months old) and three CSL *(Zalophus californianus*) pups (two female and one male, ages approximately 9-10 months old) that were stranded on the California coast and transported to The Marine Mammal Center (Sausalito, CA) for rehabilitation. The veterinary staff determined that euthanasia was appropriate for the pups due to their poor clinical prognoses, and veterinary staff euthanized the animals with a barbiturate overdose. All samples were collected under a Marine Mammal Protection Act permit from the National Marine Fisheries Service (No. 18786), and the rare and valuable nature of this tissue dictates the small sample size.

Tissue preservation

The bodies of the five pups were made available after the veterinary staff pronounced the animals dead. Within 10 to 15 minutes, the heads were removed and a flexible rubber tube was inserted into each carotid artery and held in place with an adjustable rubber band. Each head was

then perfused through the carotid arteries via gravity perfusion with four liters of 0.01 M phosphate-buffered saline (PBS), followed by four liters of 4% paraformaldehyde (PFA) in PB (pH 7.5) for approximately 20 minutes. After each perfusion, the brain was removed, and cranial nerves were sampled bilaterally and stored in 10% formaldehyde. The brains were post-fixed in 4% PFA for 36 hours. Two NES hemispheres and two CSL hemispheres were then blocked into six pieces: the brainstem, the cerebellum, and the left and right anterior and posterior cortices. Brain tissue blocks were then placed in 30% sucrose (in PB) for cryoprotection for a minimum of three days prior to sectioning. Of the three remaining brains, one NES and two CSLs, the brainstem was removed from one NES and one CSL for sectioning, but the cortices and one remaining CSL brain were kept intact for examination of the external anatomy.

Tissue processing

Each eye was removed and the anterior segment of the eye (cornea) was removed with scissors. The vitreous body was removed carefully with scissors and forceps. Segments of the optic nerve were cut close to the optic chiasma and post-fixed in 2.5% glutaraldehyde solution in PBS for a minimum of 48 hours. The cranial nerves were then transferred to osmium tetroxide, dehydrated in a graded ethanol series, placed in propylene oxide, and embedded in resin. They were then cut at 1 *u*m, mounted on a glass slide, and stained with 1% toluidine blue.

Following cryo-protection, the left anterior and posterior cortex of one NES brain (case 15-16), the left anterior and posterior cortex of one CSL brain (case 16-14), and the brainstems of the NES and CSL were cut in 50 *u*m thick coronal sections using a sliding microtome with a freezing stage. The sections were divided into eight series and one series each was stained for cytochrome oxidase (CO) (Wong-Riley, 1979), Nissl substance with thionin, or vesicular

glutamate transporter 1 or 2 protein (VGluT1, VGluT2). Nissl preparations were used to identify cell bodies, whereas CO preparations revealed areas of high metabolic activity. Vesicular glutamate transporter proteins regulate the storage and release of glutamate from the synapses of excitatory neurons, and thus stains for these proteins label the terminations of these glutamatergic axons. All immunohistochemical techniques have been previously described elsewhere (Balaram et al., 2013).

Antibody characterization

See Table 4.1 for a list of antibodies used. Rabbit anti-VGluT1 (Synaptic Systems, Goettingen, Germany) is generated against Strep-Tag fusion protein of rat VGluT1 (amino acids 456-560). Pre-absorption with the immunogen resulted in negative immunolabeling (Zhou et al., 2007), and no staining was observed in VGluT1$^{-/-}$ mice (Wojcik et al., 2004). The antibody recognizes a large fragment of the VGluT1 protein, and in Western blot preparations the antibody labels a single band at 65kDA (Balaram et al., 2013). This antibody has been used to label VGluT1 in rodents (Dondzillo et al., 2010), primates (Balaram et al., 2013), and sea lions (Sawyer et al., 2016).

Mouse anti-VGluT2 (Millipore, Bedford, MA, USA) is generated against a recombinant rat protein. In Western blots of primate neocortex, the antibody recognizes a 56-kDa band, which is the known molecular weight of VGluT2 (Balaram et al., 2013; Baldwin et al., 2013). This antibody has been used to label VGluT2 in rodents (Dondzillo et al., 2010), shrews (Wong and Kaas, 2009; Balaram et al., 2015), squirrels (Wong and Kaas, 2008), primates (Balaram et al., 2013), and sea lions (Sawyer et al., 2016).

Table 4.1 Antibodies used

Antibodies used

Antigen	Description of Immunogen	Source, host species, catalog No., close or lot No., RRID	Concentration (ug/ml)
Vesicular glutamate transporter 1 (VGLUT1)	Recombinant protein from rat (aa 456-560)	Synaptic Systems, rabbit polyclonal, 135 303, AB_887876	0.2
Vesicular glutamate transporter 2 (VGLUT2)	Recombinant protein from rat VGLUT2	Millipore, mouse monoclonal, MAB5504, AB_2187552	0.2
Biotinylated horse anti-mouse IgG	Mouse IgG	Vector, mouse polyclonal, BA-2000, AB_2313581	3
Biotinylated goat anti-rabbit IgG	Rabbit IgG	Vector, rabbit polyclonal, BA-1000, AB_2313606	3

VGluT1 and VGluT2 have characteristic complementary expression patterns in rodents and primates in neocortex and other subcortical areas. VGluT1 is strongly expressed throughout the neocortex in layers 1-3 in mice (Kaneko and Fujiyama, 2002) and primates (Balaram et al., 2013), whereas VGluT2 is strongly expressed in layer 4 of primary sensory areas in mice (Liguz-Lecznar and Skangiel-Kramska, 2007), primates (Balaram et al., 2013), ferrets (Nahmani and Erisir, 2005), and the CSL (Sawyer et al., 2016). Stains for VGluT1 and VGluT2 have been used to reveal anatomical patterns in the thalamus and brainstem of rodents (Kaneko and Fujiyama, 2002; Louderback et al., 2006; Graziano et al., 2008; Sakurai et al., 2013), primates (Qi et al., 2011; Sawyer et al., 2015) and the CSL (Sawyer et al., 2016). In mice, immunoreactivity for VGluT1 is thoroughly distributed throughout the hippocampal layers, while immunoreactivity for VGluT2 is limited to the granular cell layer of the hippocampus (Kaneko and Fujiyama, 2002). In addition, there is a nearly uniform distribution of VGluT1 in the mouse thalamus, but more discrete laminar distributions of VGluT2. The immunostaining that we saw for our VGluT1

and VGluT2 antibodies in the sea lion and elephant seal brains matched these previously reported distribution patterns.

Image acquisition and analysis

High-resolution images of the cranial nerves were obtained using an Imager M2 microscope with a mounted AxioCam Mrc (Zeiss). Images of all other processed sections were obtained using an SCN400 slide scanner (Leica) or a Nikon DXM2200 camera mounted on a Nikon (Tokyo, Japan) E800 microscope. All images were imported into Adobe Photoshop (Adobe Systems, San Jose, CA, USA) and were only adjusted for brightness and contrast when necessary.

One optic nerve per species was analyzed for the total number of myelinated fibers. For this nerve count, 100X images of the entire semi-thin section were imported into Adobe Illustrator. Two distinct classes of nerve fibers, those with thick and thin myelination, are easily identifiable at 100X magnification. A red marker was manually placed on every thinly myelinated fiber and a green marker was placed on every thickly myelinated fiber. Individual images of the red and green markers were imported into ImageJ (Schneider et al., 2012) and counted with the "Analyze particles" function. The areas of a random sample of 1,000 thick nerve fibers and 1,000 thin nerve fibers each in 3 CSL optic nerves (from 2 animals) and 1 NES optic nerve were measured in ImageJ to reveal the distribution of the sizes within the two nerve fiber categories.

For reconstruction of the cortex and midbrain structures, sections stained for CO, Nissl, and VGluT2 were used. Primary visual cortex was identified as a posterior region with dense, homogenous staining of layer 4 for all three markers, while the LGN was identifiable by its

distinct shape and clearly divided septa. The series stained for CO was scanned, and the images were imported into Adobe Illustrator for reconstruction; each CO section was approximately 400 *u*m apart from one another. For primary visual cortex, these sections were outlined, and the regions with a dark CO band in layer 4 were identified and traced. The boundaries of the presumptive primary visual cortex were identified after the alignment of these tracings. The presumptive primary visual cortex was then plotted onto a photograph of the juvenile NES or CSL brain following the identification of major sulci. As both primary (area 17) and secondary visual cortex (area 18) of well-studied carnivores, such as cats and ferrets (Sanides and Hoffmann, 1969; Price, 1985; Innocenti et al., 2002), have primary-like architectonic features, including a dense expression of VGluT2 in layer 4 (unpublished results), the depicted primary visual cortex discussed in this study likely includes areas 17 and 18. For the LGN and superior colliculus, the sections were similarly traced and the divisions of this structure were marked and aligned.

Anatomical designations

Anatomical designations for sulci were made with references to reports of other pinnipeds, including the CSL (Murie, 1874; Montie et al., 2009; Sawyer et al., 2016), otarrid fur seal (Fish, 1898; Ladygina et al., 1985) and phocid seal (Turner and Miller, 1880; Rioch, 1937). Detailed reports on the brains of other carnivores (dog, *Canis familiaris*: Singer (1962); cat, *Felis domesticus*: Snider and Niemer (1961)) were also referenced.

Results

In the mammalian visual pathway, visual information processed by the retina is projected through the optic nerve to the thalamus and midbrain. The ascending visual system has major relays in the thalamus and cortex as described below.

Visual anatomy

Some external features of the NES and CSL bodies that are relevant to the visual system are displayed in Figure 4.1. Male NES are known for their prominent trunk or proboscis that elongates following sexual maturity, but they also have a broad face with very large, frontward facing eyes (Fig. 4.1A). The trunk of the face is large enough that it physically occludes part of the visual field for each eye (Fig. 4.1B). The large eyecup is approximately 47 mm in diameter at the largest part of the eye. The vitreous body was very rigid as opposed to a soft, gel-like material, and not easily detachable from the retina. The NES has a third protective eyelid, or nictitating membrane, that swipes horizontally across the eye to moisten and remove debris and offers physical protection when the seal is submerged. Each eye has an almost spherical lens, a thick cornea, and a highly developed blueish-green tapetum, or mirror-like layer that reflects light back through the eye, that extends 22 mm in radius uniformly around the optic disk when the eyecup is flattened.

The eyes of the CSL are also front-facing, but they are located more laterally than the eyes of the NES (Fig. 4.1C). The CSL pup has large, round eyes that sit above long vibrissae and are fully open at birth. Each eye distinctly extends laterally (Fig. 4.1D), and the eyecup is approximately 31 mm in diameter at the largest part of the eye. Like elephant seals, they also have a horizontally-swiping nictitating membrane, a spherical lens, a thick cornea, and a shiny

blueish-green tapetum layer behind the retina that extends 14 mm in radius uniformly around the optic disk when flattened.

Optic nerve

The NES optic nerve was visibly similar in cross sectional area (4.56 ± 0.01 mm^2, n = 7 cross sections of one nerve; Fig. 4.2A) to the olfactory nerve, but appeared considerably smaller than the trigeminal nerve. The nerve fibers are separated into sections by the connective tissue trabeculae, which carries the blood vessels supplying the nerve. Some astrocytes are also visible within these large sections. Two distinct populations of myelinated fibers were identifiable within the circumference of the optic nerve: fibers with thick myelin sheaths and those with thin myelin sheathes (Fig. 4.2B). There was a total of 278,521 myelinated fibers in the NES optic nerve, and these could be further divided into 253,572 (91%) thin fibers and 24,949 (9%) thick fibers. The average area of the thinly myelinated fibers in one nerve was 2.56 ± 0.05 $u m^2$ (n = 1000) compared to 12.50 ± 0.19 $u m^2$ (n = 1000) for the class of thickly myelinated fibers. The areas of thinly myelinated fibers ranged from 0.14 $u m^2$ to 9.26 $u m^2$ and resembled a normal distribution with a slight right skew, while the areas of thickly myelinated fibers had a wider range of values (1.39 $u m^2$ - 46.02 $u m^2$) and no distinct peaks or skew (Fig. 4.2C). The distribution of fibers with thick or thin sheaths was not uniform across the entirety of the optic nerve. Most areas within the optic nerve contained many fibers with thin sheaths and few fibers with thick sheaths (Fig. 4.2D), with the except of one section of the optic nerve near its edge which had a higher concentration of fibers with thick sheaths (Fig. 4.2E).

The cross-sectional area (5.25 ± 0.02 mm^2, n = 12) of the CSL optic nerve appeared larger than that of the trigeminal nerve. (Fig. 4.3A). Two classes of myelinated fibers were

Figure 4.1 **External visual anatomy of the northern elephant seal and California sea lion**. **(A)** The elephant seal has large, front-facing eyes. **(B)** Lateral view of the elephant seal shows its large, bulging eyes and thick eyelid, in addition to its large trunk. **(C)** Sea lion eyes are slightly more lateralized than the elephant seal. **(D)** Lateral view of the sea lion face and eye.

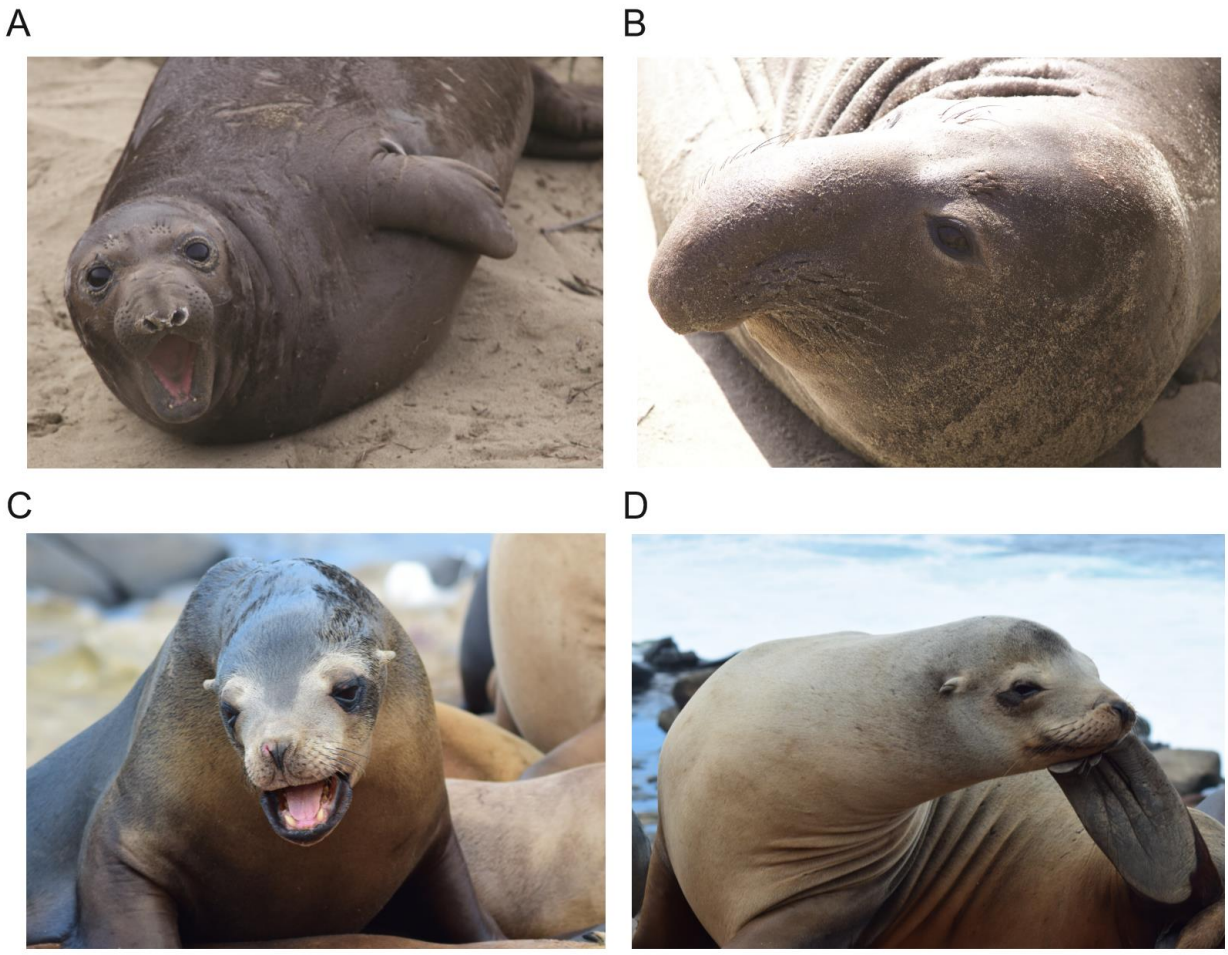

apparent in the CSL optic nerve, but these classes were less obvious at 100X magnification than those of the NES (Fig. 4.3B). The total number of myelinated fibers in the CSL optic nerve was 129,958, subdivided into 120,439 (92.7%) thin fibers and 9,519 (7.3%) thick fibers. The areas of thinly myelinated fibers in one nerve ranged from 1.35 um^2 to 17.16 um^2 and resembled a normal

distribution with a minimally present right skew, while the areas of thickly myelinated fibers had a wider range of values (7.35 um^2 - 119.71.02 um^2) and no distinct peaks or skew (Fig. 4.3C). The average area of the thinly myelinated fibers averaged across three nerves was 5.39 ± 0.4 um^2 (n = 3000; 1000 per nerve) compared to 30.26 ± 0.24 um^2 for the class of thickly myelinated fibers (n = 3000). The distribution of thin and thick fibers was generally consistent across the entirety of the optic nerve, with most areas containing mainly thinly myelinated fibers. The one exception was a small area near the center of the nerve that appeared to contain a slightly increased quantity of thickly myelinated fibers relative to the rest of the nerve (Fig. 4.3D, E).

Superior colliculus

The superior colliculus of the NES is large and distinctly laminated, arranged into different layers based on neuronal morphology and afferent/efferent projection patterns. In related mammals, retinal projections primarily terminate in the superficial layers of the SC, including the zonal layer (SZ), upper and lower superficial gray layers (uSGS and lSGS, respectively), and selectively within the optic layer (SO). The mammalian SC is typically subdivided into approximately seven cytoarchitecturally distinct layers and further sublayers based on CO and Nissl preparations, and our results are largely consistent with previous findings in other mammals (Viktorov, 1968; Kanaseki and Sprague, 1974; Norita, 1980; Laemle, 1981; 1983; May, 2006) (Fig. 4.4).

In coronal sections through the midbrain stained for Nissl, CO, and VGluT2 protein, the superficial SC layers could be divided based on the intensity and structures of the staining. The outermost narrow layer, SZ, was characterized by a thin, densely stained band of VGluT2 protein immunoreactivity. Ventral to the SZ, the densely packed superficial gray layer (SGS) could be

Figure 4.2 **Optic nerve of the elephant seal**. (**A)** Photomicrograph of the optic nerve stained with toluidine blue. (**B)** Photomicrograph of the optic nerve stained with toluidine blue at 100x magnification used for counting. Red dots label examples of thin fibers. Green dots label examples of thick fibers. (**C)** Histograms of the distribution of axon area (um^2) in the optic nerve of thinly myelinated (top) and thickly myelinated (bottom) fibers. **(D)** Higher magnification view of the rectangle labeled "1" in panel A. Thin fibers are labeled with red dots and thick fibers labeled with green dots. This section of the optic nerve represents the majority of the optic nerve where are more labeled the thin (red) fibers. (**E)** Higher magnification view of the rectangle labeled "2" in panel A. This section of the optic nerve shows an example from a specific area of the optic nerve where there are more labeled thick (green) fibers.

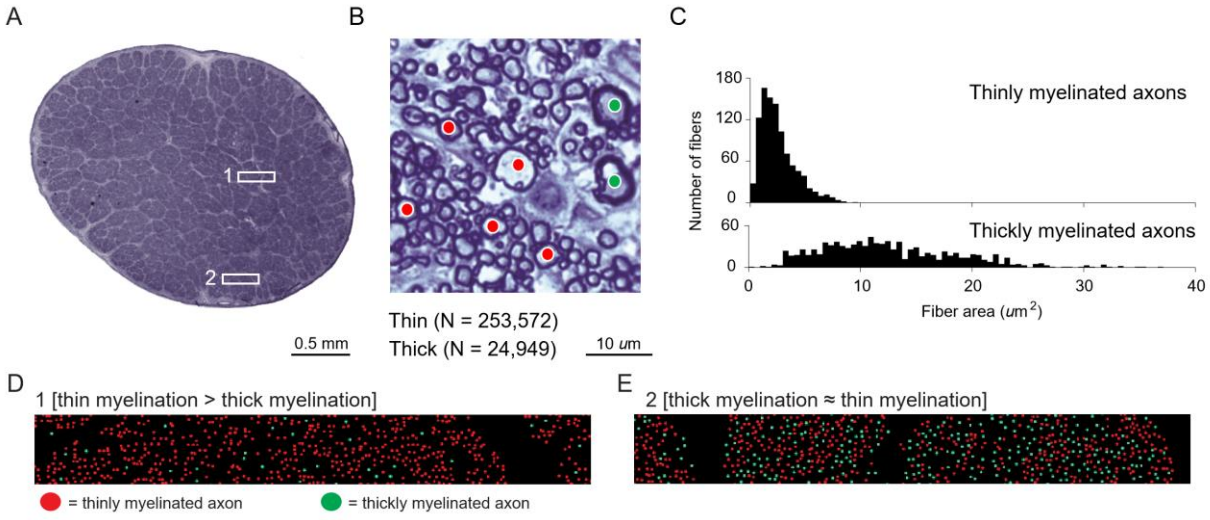

Figure 4.3 **Optic nerve of the sea lion. (A)** Photomicrograph of the optic nerve stained with toluidine blue. **(B)** Photomicrograph of the optic nerve stained with toluidine blue at high counting magnification. Red dots label examples of thin fibers. Green dots label examples of thick fibers. **(C)** Histograms of the distribution of axon area (um^2) in the optic nerve of thinly myelinated (top) and thickly myelinated (bottom) fibers. **(D)** Higher magnification view of the rectangle labeled "1" in panel A. Thin fibers are labeled with red dots and thick fibers labeled with green dots. This section of the optic nerve represents the majority of the optic nerve where are more labeled the thin (red) fibers. **(E)** Higher magnification view of the rectangle labeled "2" in panel A. This section of the optic nerve shows an example from a more centrally-located area of the optic nerve where there is a slight increase in labeled thick (green) fibers.

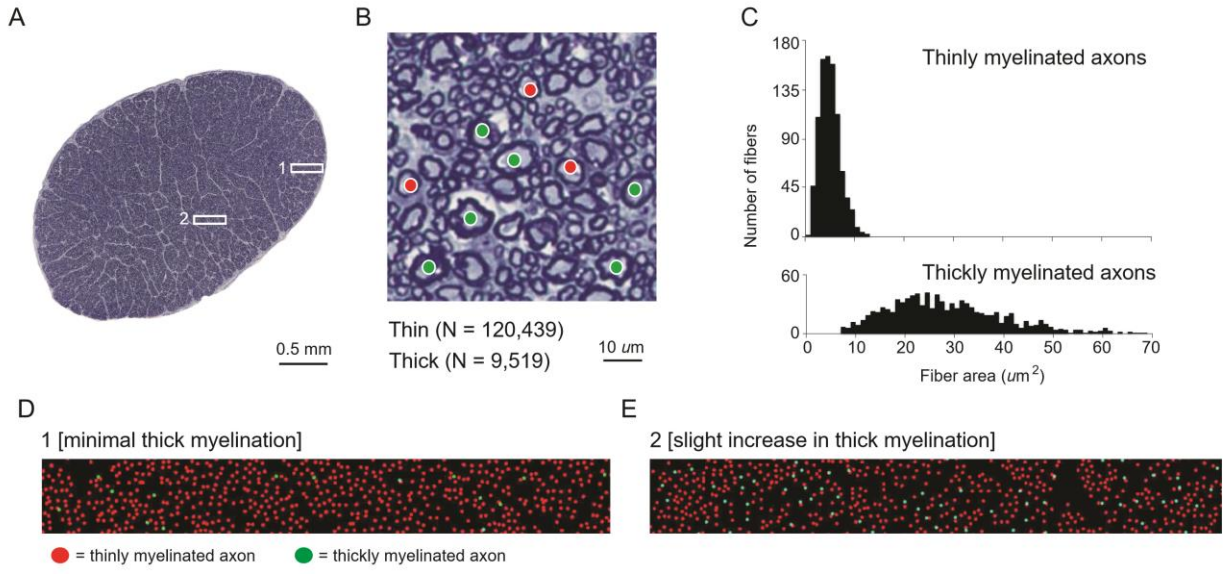

separated into two further sublayers: the dorsal uSGS and the ventral lSGS. The uSGS contained dense VGluT2 terminations, which is consistent with its role as a major recipient of retinotectal projections (Fig. 4.4F). This thick band of VGluT2 immunoreactivity in the uSGS was patchy, indicating that retinal inputs were not evenly distributed within this sublayer. The SO layer showed less intense staining for VGluT2 protein and moderate CO label.

The SC of the CSL was distinctly laminated in a similar manner to the NES (Fig. 4.5). The superficial SC layers could be divided based on the intensity of coronal sections stained for Nissl substance, CO, and VGluT2 protein. SZ was characterized by a thin, densely stained band of VGluT2 immunoreactivity, while SGS was immunoreactive for VGluT2 protein and could be divided into two additional sublayers: the dorsal uSGS that contained a dark VGluT2 immunoreactive band (Fig. 4.5F), and the ventral lSGS that stained less strongly for VGluT2 protein. The dark VGluT2-positive band in the lower part of the uSGS was more broadly dispersed and less patchy than in the NES. The SO layer showed less intense staining for VGluT2 protein and CO.

Ventral to the three superficial layers, four deeper layers, the intermediate gray layer (SGI), intermediate white layer (SAI), deep gray layer (SGP), and deep white layer (SAP) were identified in the NES and CSL based on Nissl, CO, and VGluT2 processing, but each of these areas contained less intense VGluT2 terminations than the lower subdivision of the uSGS. The periaqueductal gray area (PAG), which is adjacent to the cerebral aqueduct, was characterized by dark and uniform VGluT2 immunoreactivity in both species.

Figure 4.4 **Histology of the elephant seal superior colliculus. (A)** Section 853 processed for Nissl substance and labeled for all layers of the superior colliculus. **(B)** Higher magnification of the superficial layers of section 853 showing the zonal layer, superficial gray layer, and optic layer. **(C)** Section 851 processed for cytochrome oxidase reactivity. **(D)** Higher magnification of section 851 showing the superficial layers. **(E)** Section 852 processed for vesicular glutamate transporter 2 protein immunoreactivity. **(F)** Higher magnification image of section 852. A patchy, dense band of vesicular glutamate transporter 2 protein terminations is present in the upper superficial gray layer. Arrowheads indicate patches of vesicular glutamate transporter 2 terminations. SZ, zonal layer; uSGS, upper superficial gray layer; lSGS, inner superficial gray layer; SO, optic layer; uSGI, upper intermediate gray layer; lSGI, lower intermediate gray layer; SAI, intermediate white layer; SGP, deep gray layer; SAP, deep white layer; PAG, periaqueductal gray; CO, cytochrome oxidase; VGluT2, vesicular glutamate transporter 2 protein; D, dorsal; L, lateral.

Figure 4.5 **Histology of the sea lion superior colliculus. (A)** Section 754 processed for Nissl substance and labeled for all layers of the superior colliculus. **(B)** Higher magnification image of the section 754 showing the zonal layer, superficial gray layer, and optic layer. **(C)** Section 745 processed for cytochrome oxidase reactivity. **(D)** Higher magnification image of section 745 showing the superficial layers. **(E)** Section 780 processed for vesicular glutamate transporter 2 protein immunoreactivity. **(F)** Higher magnification image of section 780 showing a broadly dense band of vesicular glutamate transporter 2 protein terminations in the upper superficial gray layer. An arrowhead indicates an area of dense terminations, but it is more broadly distributed instead of patchy. SZ, zonal layer; uSGS, upper superficial gray layer; lSGS, inner superficial gray layer; SO, optic layer; uSGI, upper intermediate gray layer; lSGI, lower intermediate gray layer; SAI, intermediate white layer; SGP, deep gray layer; SAP, deep white layer; PAG, periaqueductal gray; CO, cytochrome oxidase; VGluT2, vesicular glutamate transporter 2 protein; D, dorsal; L, lateral.

Figure 4.4

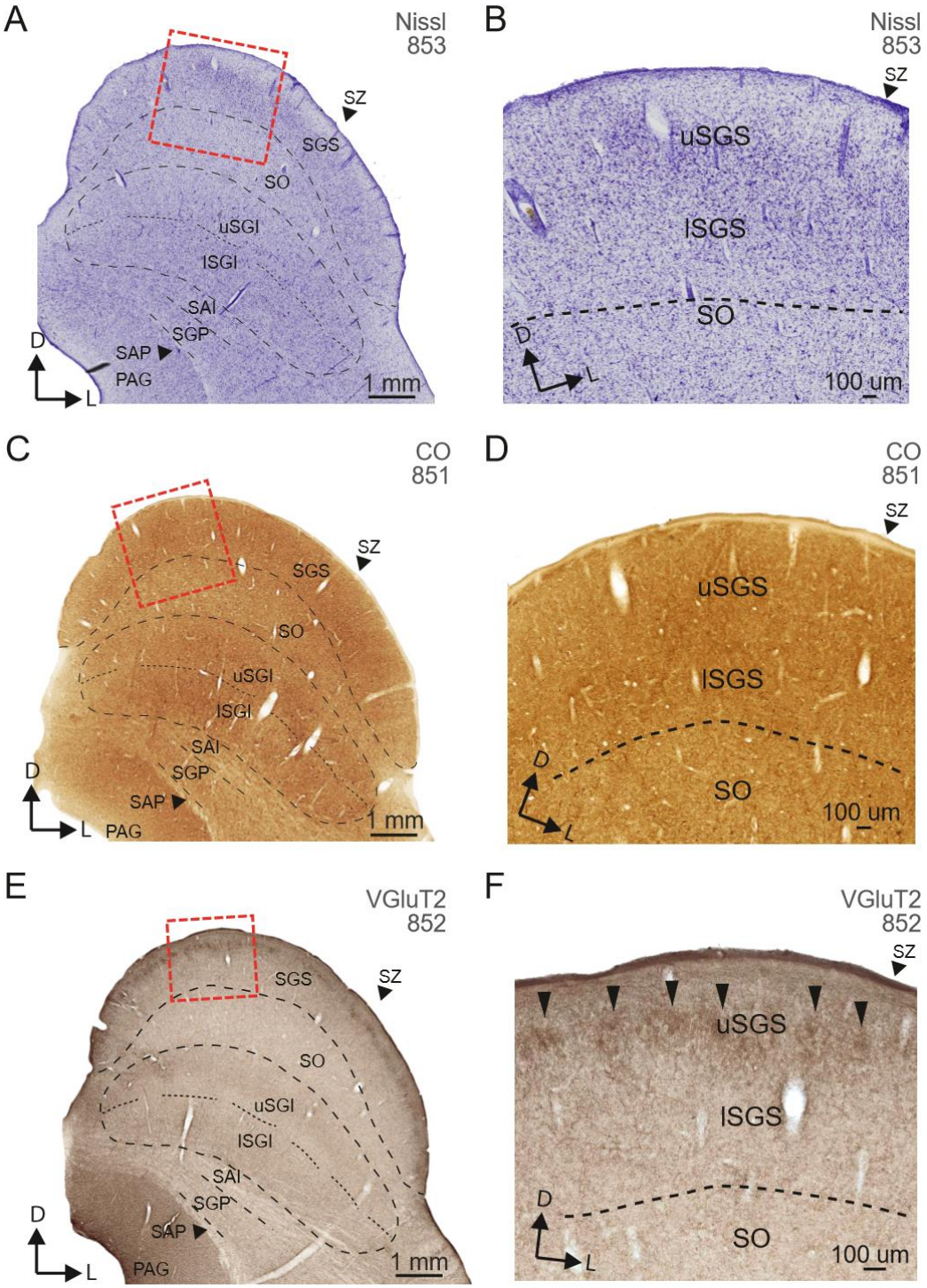
A
Nissl
853
SZ
SGS
SO
uSGI
lSGI
SAI
SGP
SAP
PAG
D
L
1 mm
B
Nissl
853
SZ
uSGS
lSGS
SO
D
L
100 um
C
CO
851
SZ
SGS
SO
uSGI
lSGI
SAI
SGP
SAP
PAG
D
L
1 mm
D
CO
851
SZ
uSGS
lSGS
SO
D
L
100 um
E
VGluT2
852
SZ
SGS
SO
uSGI
lSGI
SAI
SGP
SAP
PAG
D
L
1 mm
F
VGluT2
852
SZ
uSGS
lSGS
SO
D
L
100 um

Figure 4.5

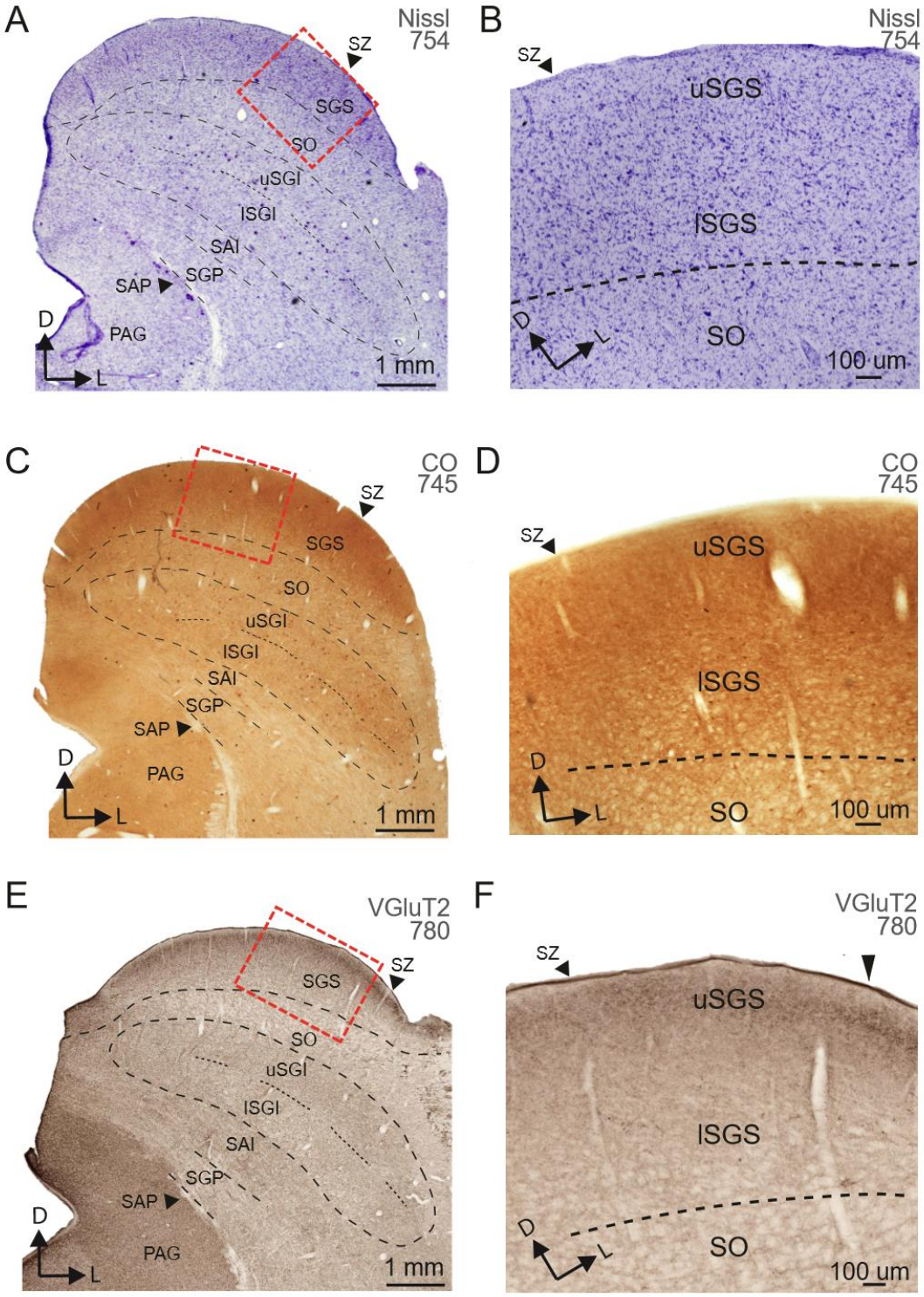
A
Nissl
754
SZ
SGS
SO
uSGI
lSGI
SAI
SGP
SAP
PAG
D
L
1 mm
B
Nissl
754
SZ
uSGS
lSGS
SO
D
L
100 um
C
CO
745
SZ
SGS
SO
uSGI
lSGI
SAI
SGP
SAP
PAG
D
L
1 mm
D
CO
745
SZ
uSGS
lSGS
SO
D
L
100 um
E
VGluT2
780
SZ
SGS
SO
uSGI
lSGI
SAI
SGP
SAP
PAG
D
L
1 mm
F
VGluT2
780
SZ
uSGS
lSGS
SO
D
L
100 um

Lateral geniculate nucleus

In coronal sections through the blocks of the NES that contain the thalamus (Fig. 4.6A-D), the LGN stains densely for CO and VGluT2 protein. These markers reveal distinct architectonic borders within the thalamus, as there are three distinct subdivisions of the LGN visible in the Nissl, CO, and VGluT2 sections. These divisions correspond to the most lateral layer A, layer A1, and the most medial layer C of other carnivores (Daw and Pearlman, 1970; Guillery and Kaas, 1971; Sanderson, 1974). In the NES, the three layers are similar in size. There are distinct subdivisions marked by changes in VGluT2 immunoreactivity within the C layer, which likely are layers C1 and C2. Figure 4.6E displays sketches of the LGN showing its progression from rostral sections (section 617) to near its caudal extent (section 561). The LGN was rostro-caudally present over approximately 3.6 mm in the sections cut in the coronal plane. The septum corresponding to the optic disk of the retina (Kaas et al., 1973) is shown in Nissl section 577, where it is located in the A layer that receives input from the contralateral eye. The location of the MIN area is unclear.

In coronal sections through the thalamus of the CSL brain, the LGN stains densely for CO and VGluT2 protein (Fig. 4.7A-D). Contralateral layer A is distinctly larger than ipsilateral layer A1. Layer C is the most medial layer, and its boundaries are less clear than layers A and A1. Layer A1 is divided into two segments, at the dorsal and ventral locations of the LGN. The locations of the MIN area and the optic disk are unclear. Figure 4.7E displays sketches of the LGN showing its progression from the most rostral sections (section 672) to its caudal extent (section 608). The LGN was rostro-caudally present over approximately 4.6 mm in the coronal plane.

Figure 4.6 **Histology and representation of the elephant seal lateral geniculate nucleus**. Brain sections 545 - 633 through the cortex contained the lateral geniculate nucleus. **(A)** Schematic of section 593 cut in the coronal plane. The red shading indicates the boundaries of the lateral geniculate nucleus (LGN), and the grey lines show the subdivisions of the LGN as indicated by histological markers. **(B-D)** High magnification images of sections 593, 588, and 594 stained for Nissl substance, cytochrome oxidase, and vesicular glutamate transporter 2 protein, respectively. The dashed lines represent the boundaries of the LGN, and individual layers are labeled based on distinct septa visible in each stain. The arrowheads in panel D indicate the possible locations of further C layers based on changes in VGluT2 immunohistochemistry. **(E)** Schematic of coronal sections through the LGN and surrounding thalamic areas from rostral to caudal sections. Nissl section 577 shows the location of the optic disk in the dashed box. CO, cytochrome oxidase; VGluT2, vesicular glutamate transporter 2 protein; D, dorsal; M, medial.

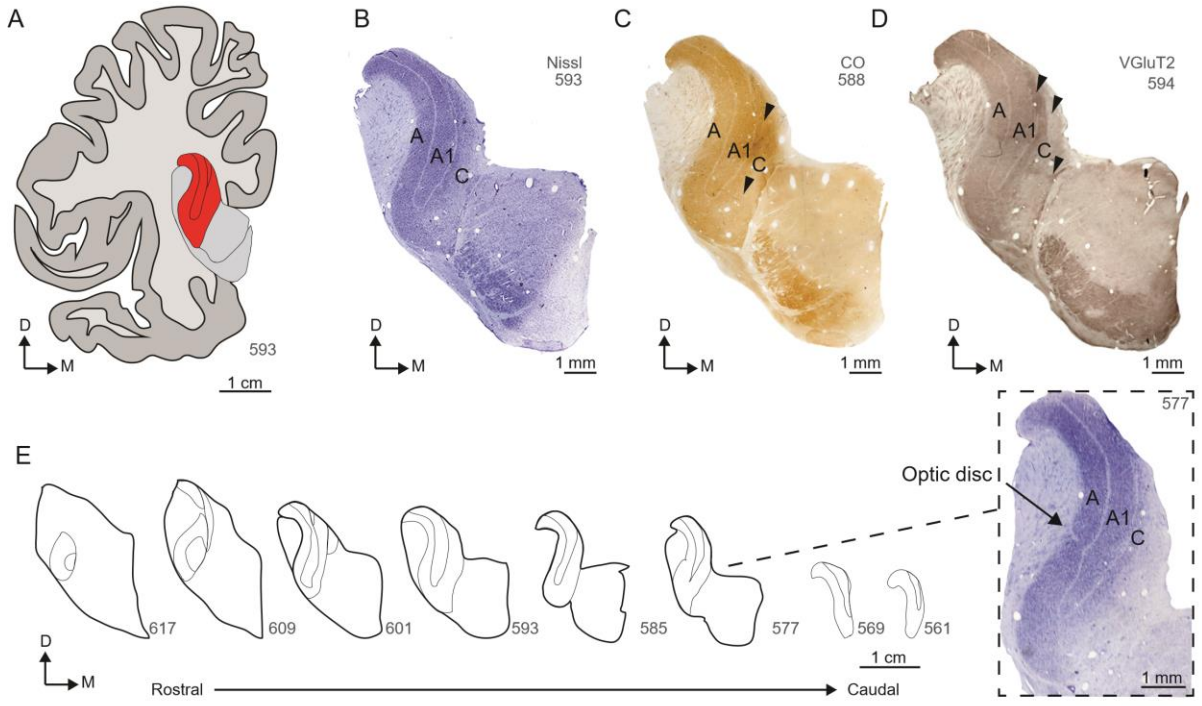

Figure 4.7 **Histology and representation of the sea lion lateral geniculate nucleus**. Brain sections 600 - 672 through the cortex contained the lateral geniculate nucleus. **(A)** Schematic of section 608. The red shading indicates the boundaries of the lateral geniculate nucleus (LGN) and the grey lines show the subdivisions of the LGN as indicated by histological markers. (**B-D)** High magnification images of sections 608, 609, and 610 stained for Nissl substance, cytochrome oxidase, and vesicular glutamate transporter 2 protein, respectively. The dashed lines represent the boundaries of the LGN, and individual layers are labeled based on distinct septum visible in each stain. (**E)** Schematic of coronal sections through the LGN and surrounding thalamic areas from rostral to caudal. CO, cytochrome oxidase; VGluT2, vesicular glutamate transporter 2 protein; D, dorsal; M, medial.

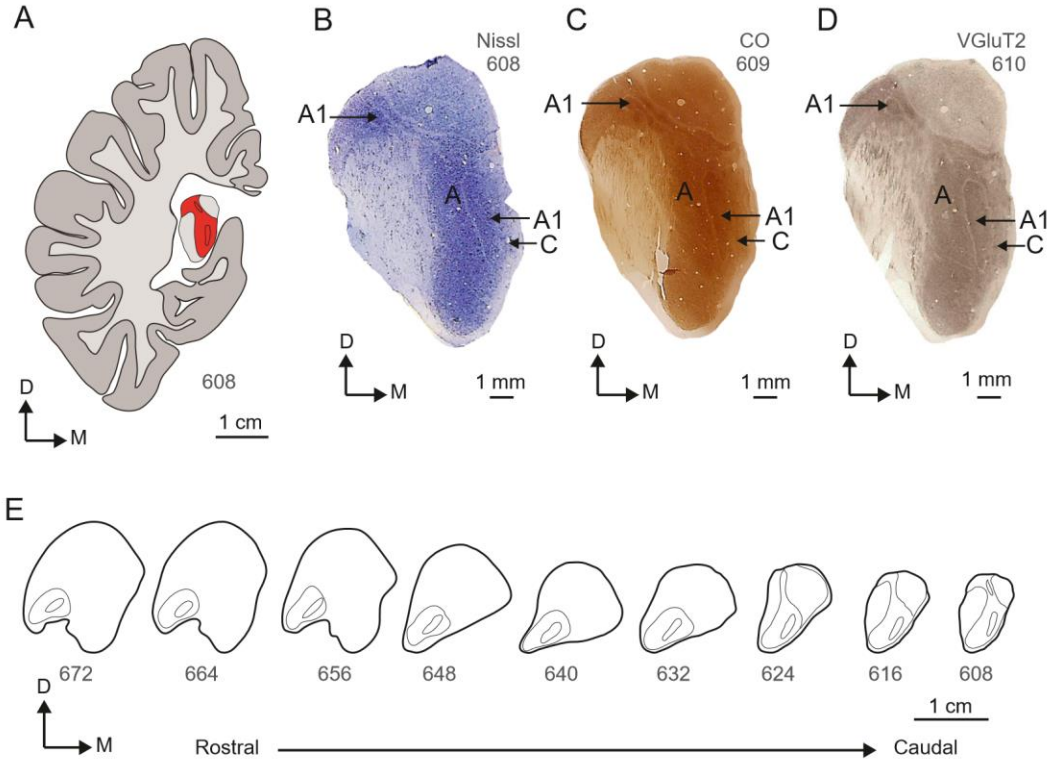

Visual cortex

The external brain of one intact juvenile NES brain was examined. The brain was widest at the middle near the anterior front of the cerebellum (11 cm), and narrowest in the anterior regions (3.6 cm). The brain was approximately 9.3 cm long in length, and the weight after perfusion and immersion fixation was 485 g. For the two intact juvenile CSL brains examined, each brain was widest at the posterior end where occipital cortex is located (9.0 cm, 9.0 cm), and narrowest towards the anterior portion of the brain (2.0 cm, 2.4 cm). The two brains were 9.2 cm and 9.0 cm long, weighing 278.4 g and 289.7 g, respectively, after perfusion and immersion fixation.

The NES neocortex is most notable for its elaborate patterns of sulci and gyri. The sulcal patterns between hemispheres were similar enough that they could be identified, but they were not identical. Brief examination of the second NES brain prior to cutting revealed that across individuals, the most significant or deep sulci were relatively consistent in location, but shallow and less pronounced sulci were more variable in location, depth, and size. Distinct sulci and anatomical features related to the visual system are indicated in Fig. 4.8. The optic nerves are located on the ventral side of the brain posterior to the olfactory bulbs (Fig. 4.8A). Dorsal, caudal, and medial views of the NES brain reveal the locations of posterior sulci that were found near or borders of primary visual cortex (Fig. 4.8B-D). These sulci and the optic nerve are labeled in a schematic of these brain views in Fig. 4.8E-H.

The neocortex of the CSL was similar to the NES neocortex in that it also contained a large number of sulci. Despite both CSL brains being consistent in the general location of major sulci, such as the lateral sulcus and posterior lateral sulcus, there are major hemispheric and

individual differences in the distribution and size of other sulci. More shallow sulci were more variable in their characteristics between the two brains, as opposed to deeper sulci that could be easily distinguished in either brain. Prominent sulci related to the visual system and the optic nerve are displayed in Fig. 4.9. Ventral, dorsal, caudal, lateral, and medial views of the CSL

Figure 4.8 **Anatomy of the elephant seal cortex.** (**A-D)** Ventral, right dorsal, right caudal, and right medial views, respectively. Panels B, C, and D show a single hemisphere. (**E-H)** Drawings of A-D with four major posterior sulci labeled. The optic nerve (cranial nerve II) is also labeled in E. SS, splenial sulcus; LS, lateral sulcus; ES, entolateral sulcus. C, caudal; D, dorsal; L, lateral. Scale bars = 1 cm.

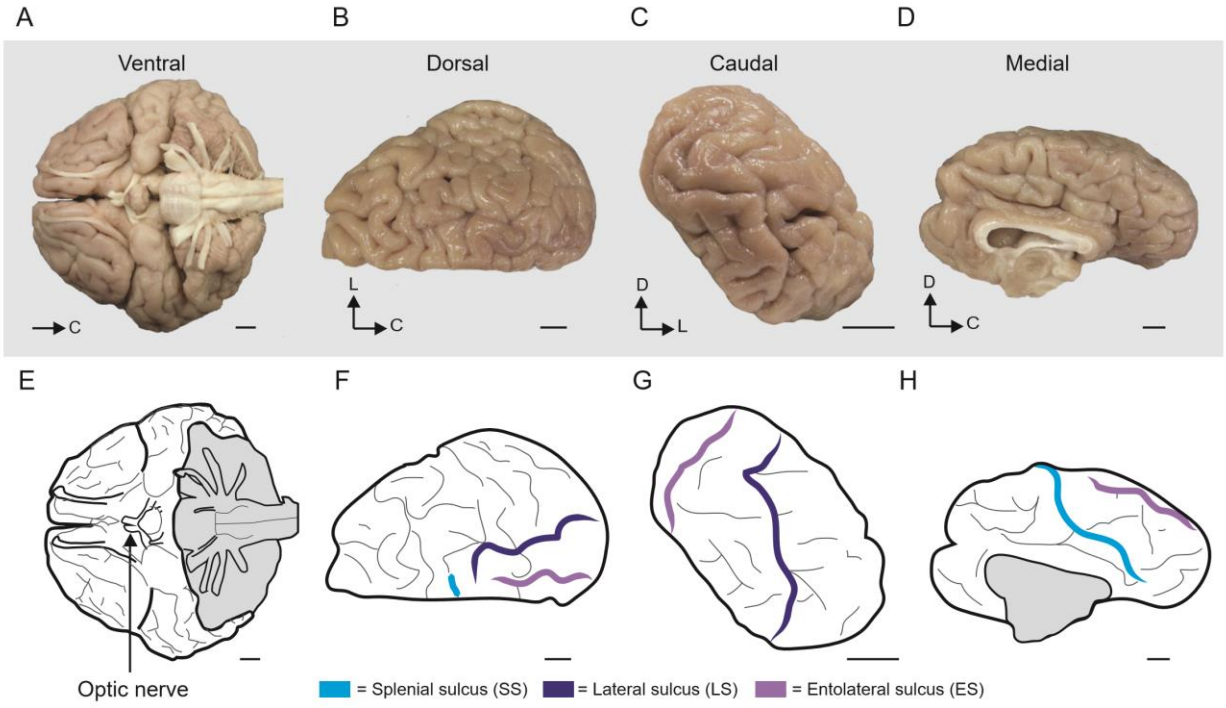

Figure 4.9 **Anatomy of the sea lion cortex.** (**A-E)** Ventral, dorsal, caudal, left lateral, and left medial views, respectively. Note that the cerebellum and brainstem have been removed in the ventral view. **(F-J)** Drawings of A-E with major sulci labeled. The optic nerve (cranial nerve II) is labeled in F. Lat, lateral sulcus; Ps, pseudosylvian sulcus; CoS, coronal sulcus; Ans, ansate sulcus; Sp, splenial sulcus; Cs, cruciate sulcus; SuS, suprasplenial sulcus; PLs, posterior lateral sulcus; SE, ectolateral sulcus; C, caudal; D, dorsal. Scale bars = 1 cm.

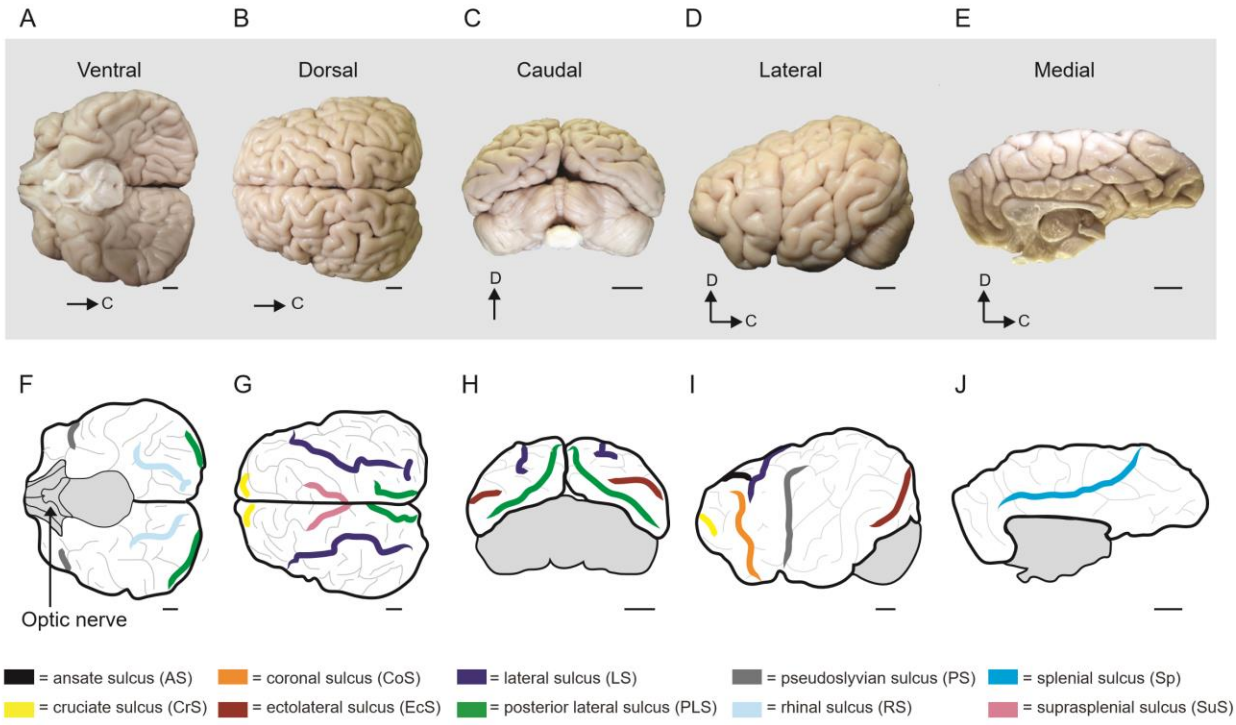

brain (Fig. 4.9A-E), and their schematic representations with labeled sulci (Fig. 4.9F-J) reveal the locations of both posterior sulci that are relevant to primary visual cortex and anterior sulci that have been identified in previous studies (Sawyer et al., 2016) . The optic nerves are located on the anterior ventral side of the brain (Fig. 4.9F).

Sections stained for CO, Nissl substance, and VGluT2 protein in both species contained a densely-stained band in select regions (elephant seal: Fig. 4.10A-D; sea lion: Fig. 4.11A-D).

These regions had six distinct layers based on differences in cell distribution and size. The densely-stained band corresponded to layer 4 in the Nissl sections (elephant seal: Fig. 4.10E-G; sea lion: Fig. 4.11A-D), which consists of densely packed small cells, a feature that is characteristic of primary sensory areas. Aside from a densely-packed layer 4, other characteristics included a cell sparse layer 1, a thin and sparsely packed layer 5, and a thick and densely packed layer 6. Together, these features identity this region as primary visual cortex, given its location in the caudo-medial location. The region we identify here likely includes area 18, which receives input from the LGN and has primary-like architectonic features in other carnivores (Sanides and Hoffmann, 1969; Stone and Dreher, 1973; Price, 1985; Innocenti et al., 2002).

In the NES, the medial-dorsal areas of sections 1 - 857 (spanning approximately 4.28 cm on the anterior-posterior axis) contained the densely stained layer 4, the presumptive primary visual cortex (Fig. 4.12A-B). In the most posterior regions of the brain, primary visual cortex is bordered ventrally by the splenial sulcus and dorsal-laterally by the lateral sulcus. In increasingly anterior sections, the entolateral sulcus emerges as a dorsomedial fissure within primary visual cortex. In the most posterior sections, the extent of the dense band extended far ventrally along the medial wall, but decreased to only the dorsal region by section 857 at the disappearance of the splenial sulcus. A 3D reconstruction of the dorsolateral view highlighting the presumptive primary visual cortex is shown in Figure 4.12A. Primary visual cortex also extends onto the medial wall of the cerebral hemisphere throughout its entire anterior to posterior extent (not shown).

Figure 4.10 **Histology on coronal sections of the elephant seal visual cortex.** Brain sections 0 - 857 through the cortex contained primary visual cortex. **(A)** Schematic of section 107. The red line is the area where the presumptive primary visual cortex is, as defined in sections stained for cytochrome oxidase, Nissl substance, and vesicular glutamate transporter 2 protein (shown here). Arrows point to the architectonic borders of primary visual cortex. **(B)** Section 100 stained for Nissl substance showing neuron-dense layers 4 and 6. **(C)** Section 97 stained for cytochrome oxidase, showing a darkly stained band in layer 4. **(D)** Section 107 stained for vesicular glutamate transporter 2 protein, showing dense labeling in layer 4 and sparse labeling corresponding to layer 6. **(E-G)** Enlarged sections of the area within the black dashed lines in B-D show the laminar distributions of each marker. Black horizontal lines indicate the laminar boundaries. CO, cytochrome oxidase; VGluT2, vesicular glutamate transporter 2 protein; D, dorsal; L, lateral.

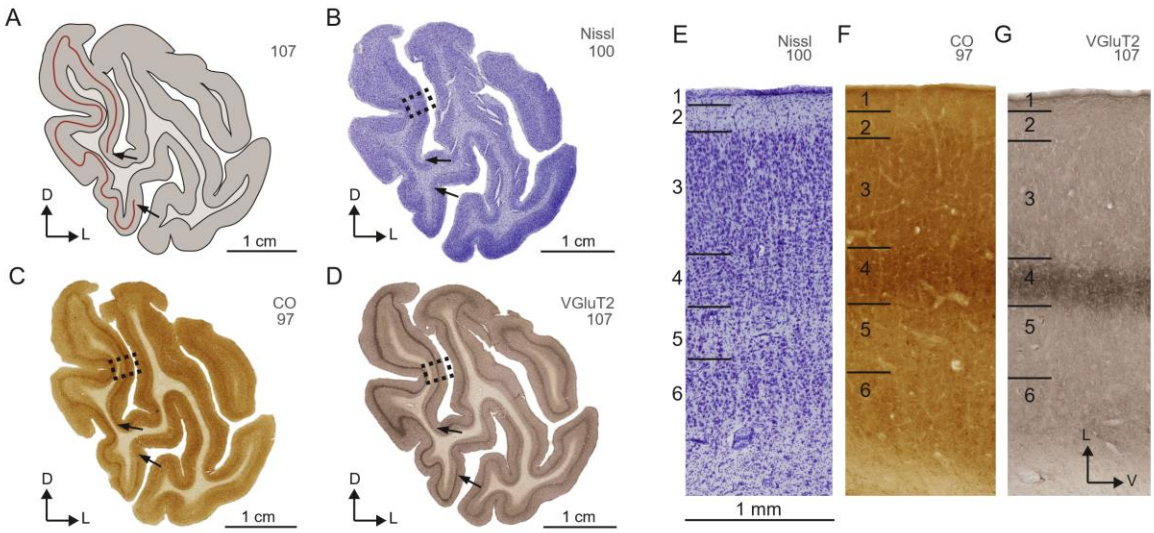

Figure 4.11 **Histology on coronal sections of the sea lion primary visual cortex.** Brain sections 0 - 553 through the cortex contained primary visual cortex. **(A)** Schematic of section 131. The red line is the area where the presumptive primary visual cortex is, as defined in sections stained for cytochrome oxidase, Nissl substance, and vesicular glutamate transporter 2 protein (shown here). Arrows point to an example of the architectonic borders of primary visual cortex. **(B)** Section 209 stained for Nissl substance showing neuron-dense layers 4 and 6. **(C)** Section 202 stained for cytochrome oxidase, showing a darkly stained band in layer 4. **(D)** Section 212 stained for vesicular glutamate transporter 2 protein, showing dense labeling in layer 4 and sparser labeling corresponding to layer 6. **(E-G)** Enlarged sections of the area within the black dashed lines in B-D show the laminar distributions of each marker. Black horizontal lines indicate the laminar boundaries. CO, cytochrome oxidase; VGluT2, vesicular glutamate transporter 2 protein; D, dorsal; M, medial.

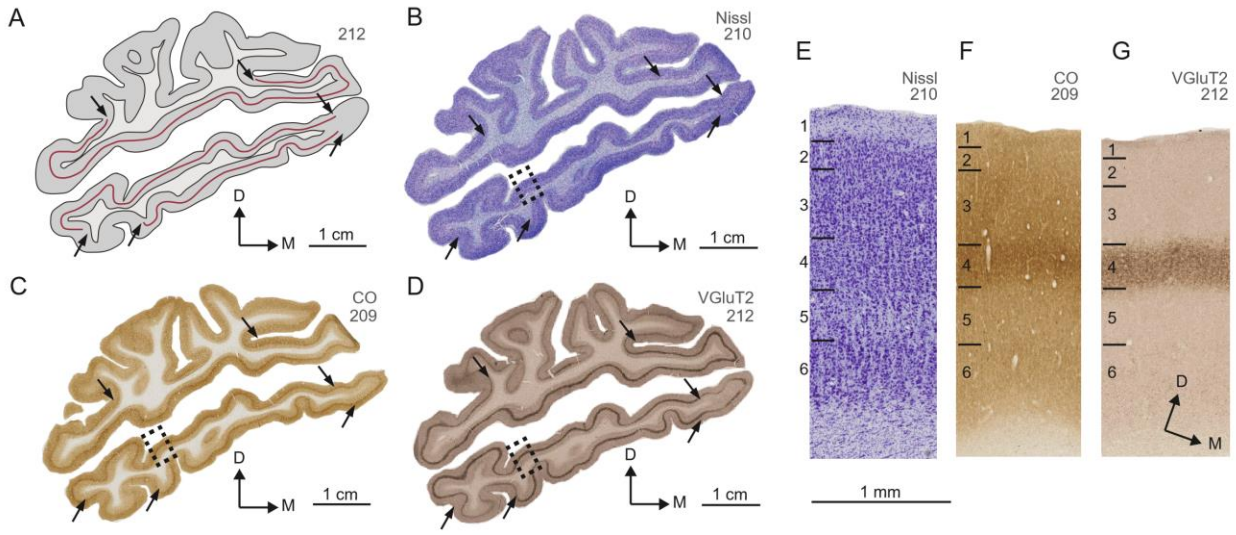

In the CSL, primary visual cortex is located in the most posterior part of the brain, along the dorsal and ventral banks of the posterior lateral sulcus (Fig. 4.13A-B). In the most posterior regions of the brain (sections 1-169), primary visual cortex includes all areas on the separated tissue inferior to the postlateral sulcus while, superior to the postlateral sulcus, primary visual cortex is bordered medially by the lateral sulcus and laterally by the ectolateral sulcus. In

increasingly anterior sections, the splenial and rhinal sulci serve as primary visual cortex borders for tissue inferior to the postlateral sulcus. In the most anterior sections (sections 457 to 553), the postlateral sulcus ends and the splenial and lateral sulci become the medial and dorsolateral primary visual cortex borders. A 3D reconstruction of the posterior view highlighting the presumptive primary visual cortex is shown in Figure 4.13A, although much of primary visual cortex is hidden within the postlateral sulcus.

Discussion

The present study aimed to characterize specific organizational components of the visual pathway in the northern elephant seal (NES) and California sea lion (CSL). Our conclusions support the hypothesis that the organization of the pinniped visual system is similar to that of closely related terrestrial mammals. The distribution of VGluT2 protein and CO in the SC, LGN, and primary visual cortex allowed us to identify novel architectonic characteristics and make inferences related to the functional properties of these areas. Overall, we find many similarities between the NES and CSL visual systems, as well as some subtle differences that may reflect varying species visual demands.

Visual anatomy

In general, pinnipeds have good vision both on land and underwater, and have overcome the anatomical challenges that terrestrial mammalian eyes face in water (Schusterman, 1981; 2006; Hanke et al., 2009). Our findings concerning the anatomy of the pinniped eye are consistent with previous reports that describe the lens, cornea, and tapetum. The blueish-green tapetal color in both pinnipeds is similar to other descriptions (Miller et al., 2010). Similar to

Figure 4.12 **The representation of primary visual cortex in the elephant seal. (A)** Sketches of dorsal, medial, and dorsal posterior views of the elephant seal cortex. The dotted lines indicate the boundaries of the coronal sections; the posterior grey area marks the numerical boundaries of primary visual cortex. The bars numbered on top correspond to the 50-um thick section numbers. The light blue overlay on each view indicates the presumptive primary visual cortex based on histological and cytoarchitectural markers. Note that the sulcal patterns across samples and between hemispheres of the same brain are variable. **(B)** Schematic of coronal sections throughout primary visual cortex. The red stripes on each section represent areas in which there are histological markers of primary visual cortex as defined in sections stained for cytochrome oxidase, Nissl, and vesicular glutamate transporter 2 protein. The number of each section, beginning with the most posterior section, is labeled in gray and corresponds to map in A. Arrows point to major sulci. SS, splenial sulcus; LS, lateral sulcus; ES, entolateral sulcus; C, caudal; D, dorsal; L, lateral.

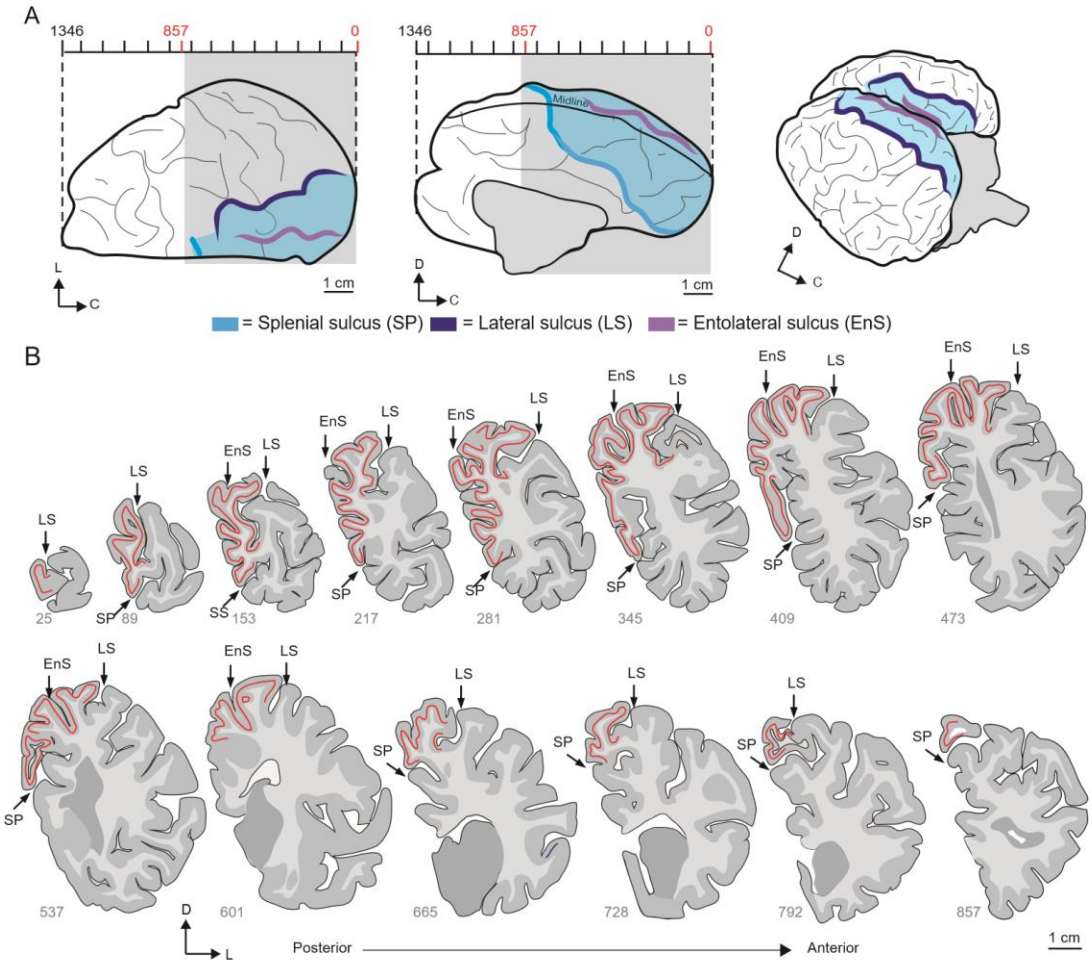

Figure 4.13 **The representation of primary visual cortex in the sea lion. (A)** Sketches of dorsal, left lateral, and posterior views of the sea lion cortex. The dotted lines indicate the boundaries of the coronal sections; the posterior grey area marks the numerical boundaries of primary visual cortex. The numbered bars on top correspond to the 50-um thick section numbers. The light blue overlay on each view indicates the presumptive primary visual cortex based on histological and cytoarchitectonic markers. Note that the sulcal patterns across 56 samples and between hemispheres of the same brain are variable. **(B)** Schematic of coronal sections throughout primary visual cortex. The red stripes on each section represent areas in which there are histological markers of primary visual cortex as defined in sections stained for cytochrome oxidase, Nissl substance, and vesicular glutamate transporter 2 protein. The number of each section, beginning with the most posterior section, is labeled in gray and corresponds to map in A. Arrows point to major sulci. AS, ansate sulcus; EcS, ectolateral sulcus; PLS, posterior lateral sulcus; SuS, suprasplenial sulcus; CoS, coronal sulcus; LS, lateral sulcus; PS, pseudosylvian sulcus; SP, splenial sulcus; C, caudal; D, dorsal; L, lateral.

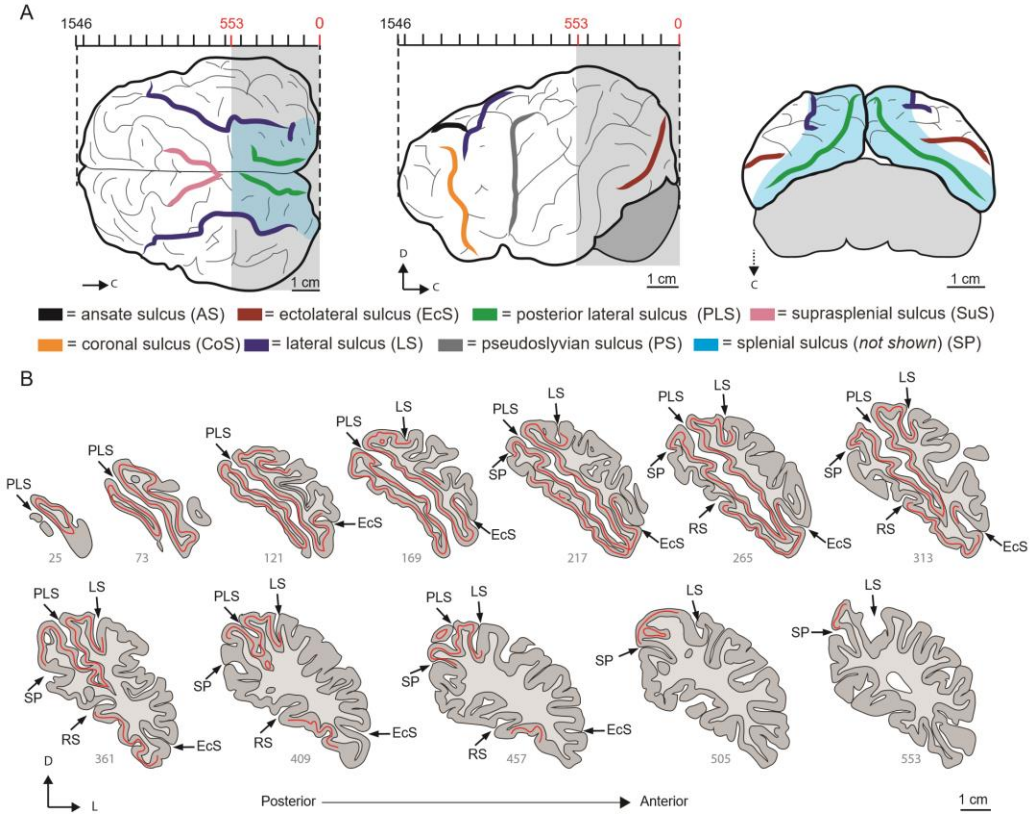

cetaceans, in which the tapetum covers between two-thirds to the entire fundus (Dawson, 1980; Young et al., 1988), the CSL and NES tapeta, like those of other pinnipeds, cover most of the fundus (Mass and Supin, 2007). Carnivores and other predatory animals that are active in the dark have well-developed tapeta to represent the lower visual field that is less bright, while most diurnal species, such as primates and birds, do not rely upon a tapetal layer for enhanced vision (Ollivier et al., 2004). One characteristic that differs between the NES and CSL is the more pronounced lateralization of the CSL eyes. Consequently, the binocular visual field of the CSL and corresponding binocular midbrain projections are likely different.

It is important to note that some anatomical features of the pinniped pups studied here differ from those of adults. For example, while the size of the eyeball in 3-month old CSL pups is approximately 31 mm, adult eyeballs can become as large as 50 mm, which is equivalent to the size of a horse eye (Ninomiya, 2016). Similarly, there are anatomical changes that occur in the NES as they develop. For example, following sexual maturity, the nose of the male NES extends dorsally between the eyes, serving as a physical barrier between the two visual fields. It is possible that these adult males lose some binocular vision and must rely on other sensory systems for judgments of depth and distance. These physical changes serve as reminders that development into adulthood triggers corresponding functional and anatomical changes in the brain that will almost certainly result in changes to the pinniped visual pathway.

Optic nerve

A correct approximation of the number of axons within any sensory nerve is important because these counts likely reflect the type or quantity of sensory information that is transmitted to the rest of the central nervous system. Similarly, these counts can offer a sense of sensory

resolution. The number of axons within the optic nerve, and the comparison of this number between species may reveal the degree to which each species relies on that particular sense, as we can expect greater innervation, and therefore more resolution, with an increasing number of axons. The cross-sectional area of the CSL optic nerve was greater than the NES optic nerve, but contained fewer myelinated fibers (NES: 278,521; CSL: 129,958). This discrepancy, in which the NES has more myelinated fibers despite a smaller area, is due to the smaller diameter of its thinly myelinated fibers that are more densely packed. The larger number of fibers in the NES optic nerve may reflect the more refined visual abilities of its eye, but there may be other factors such as eye size that influence these estimates.

Our measurements of the myelinated fibers within the optic nerve are comparable to other studies that have quantified the number of axons in two related pinniped species, the Phocid hooded seal (*Cystophora cristata*) and the harbor seal (*Phoca vitulina*) (Wohlert et al., 2016). That study reported 481,600 ± 1,300 axons in the hooded seal and 187,000 ± 8,000 axons in the harbor seal optic nerve. Other studies of the pinniped optic nerve report similar results of 147,000 fibers in the harbor seal and 174,000 in the bearded seal (*Phoca barbata*) (Putter, 1902). The hooded seal and NES are comparable in their total numbers of myelinated fibers, but both optic nerves contain more fibers compared to other pinnipeds. These differences may be related to the visual demands in their similar habitats, as the hooded seal is another deep-diving pinniped whose observed maximum diving time is one hour and diving depths exceed 1000 meters (Folkow and Blix, 1999). A closely related terrestrial carnivore species, *Canis familiaris*, or the domestic dog, has axon numbers, estimated at 154,000 (Bruesch and Arey, 1942) and 136,000 (Arey and Schaible, 1934), that are similar to those of some pinnipeds. It is plausible, based on the number of myelinated fibers, some species, such as the NES and hooded seal, may have

superior visual abilities compared to other pinnipeds and related carnivores. However, all of these estimates are considerably lower than the estimates in humans (1,244,005 ± 20,033) (Balazsi et al., 1984) or macaques (1,632,600 ± 219,650) (Sandell and Peters, 2001) who have smaller eyes. Eye size and the corresponding retinal surface area of each animal can in part explain why the NES has more optic nerve fibers than the CSL, as the NES has both a larger eyecup and larger retinal surface area. As Mass and Supin (2007) note, the overall retinal ganglion cell densities in all pinnipeds studied to date (1,000-2,500 cells/mm^2) are lower than those found in terrestrial carnivores (6,000-14,000 cells/mm^2), but when the larger pinniped eye size is taken into consideration, the average cell density per angular unit of the visual field is similar between pinnipeds and terrestrial carnivores (200-400 cells/deg^2). Thus, visual acuity is likely to be similar. However, in the dimmer deep water environment of the pinnipeds, ganglion cells may receive inputs from more rods, contributing to greater darkness sensitivity.

There are some important methodological differences between our counting methods and those of Wohlert et al. (2016). Each optic nerve in this study was counted manually in its entirety. While the number reported by Wohlert et al. (2016) is an estimate based on the size of each nerve and counts of 30 to 105 40 x 40 $u m^2$ sample frames, such estimates may be somewhat off due to regional differences in the distribution of thickly- and thinly myelinated axons. The criticism of using the method of proportionate areas in optic nerve estimations due to the presence of "thick" and "thin" fiber myelination has been addressed previously by others (Bruesch and Arey, 1942), and given the large variability in fiber diameters shown here, it is a valid concern.

Axon diameter reflects axon conduction velocity. Bishop and O'Leary (1938) were the first to provide evidence of the grouping of axons by conduction velocity in the cat optic nerve

and tract. Axons which are larger in diameter tend to have thicker myelin sheaths and this change in myelin thickness increases the velocity of the axon impulse conduction (Sanders and Whitteridge, 1946). In carnivores, the axons of X, Y, and W ganglion cells are morphologically segregated by axon diameter (Fukuda et al., 1985). The larger and more thickly myelinated nerve fibers likely stem from the Y class of ganglion cells that will conduct faster than the more thinly myelinated fibers. The X ganglion cells have thinner axons that conduct at a slower rate, while the W class with the thinnest axons conducts at the slowest rate (Fukuda, 1971). Previous studies have examined the organization of the cat optic nerve, and it has been reported in the cat that there are certain areas of the optic nerve which are characterized by clusters of large fibers (Donovan, 1967), as in the present study. This organization of fiber clusters in the optic nerve in carnivores is attributed to developmental patterns as opposed to a strict retinotopic organization (Fitzgibbon and Reese, 1996). In carnivores, all three classes of ganglion cells project to both the LGN and the SC (Stone, 1983). The M, P, and K ganglion cell classes and pathway in primates are proposed homologues of the carnivore Y, X, and W pathways (Sherman, 1985).

Superior colliculus

The distinctive SC subdivisions in the NES and CSL noted in these histochemical preparations are exciting and novel findings that have not been reported for any pinniped species. It is well known that the mammalian SC is a complex structure that plays an important role in guiding movement of the eyes, ears, and head during stimulus orientation (Huerta and Harting, 1984; Munoz and Guitton, 1985; 1989). The mammalian SC receives input from both cortical and subcortical regions in addition to projecting to numerous structures within the central nervous system (Huerta and Harting, 1984; Kaas and Huerta, 1988).

The SC is traditionally divided into three superficial layers, which are exclusively visual, and four intermediate-to-deep layers, which exhibit mixed sensory and premotor activity (Casagrande et al., 1972; Harting et al., 1973; Graham, 1977; Edwards et al., 1979; Edwards, 1980). It has been previously reported in multiple mammalian species that retinotectal projections primarily terminate within SGS, and to a lesser extent in SO (cat: Graybiel (1975; 1976), ferret: Zhang and Hoffmann (1993), monkey: Pollack and Hickey (1979), rat: Lund et al. (1980), squirrel: Petry et al. (1989)). In cats, the SGS layer of the SC receives segregated input from the Y and W classes of retinal ganglion cells; the W inputs terminate superficially near the surface of the SC and the Y afferents are found deeper near the SO layer (Hoffmann, 1973). The SC receives less but some input from the X class of retinal ganglion cells (Cleland and Levick, 1974). .

Evidence suggests that retinal ganglion cells use VGluT2 as their primary glutamatergic transporter, as strong VGluT2 protein immunoreactivity has been reported in the ganglion cells of rat and human retinas (Gong et al., 2006). This suggests that retinal projections terminating in the superficial layers of the SC should exhibit strong and diffuse VGluT2 immunoreactivity. Others have reported this exact pattern of dense superficial VGluT2 protein positive terminations in several mammalian species, including Old World macaque monkeys (Balaram et al., 2013), prosimian galagos (Balaram et al., 2011), and tree shrews (Balaram et al., 2015). This pattern is consistent with our findings, as we report a dense VGluT2-positive band in the dorsal sublayer of the SGS and a less intense, but still strong, VGluT2 immunoreactivity in the lSGS of both pinniped species. The distinct “puffs” or “patches” of VGluT2 protein in the superficial layers of the SC are characteristics of tectal organization that have been reported in cats with other histochemical stains (Huerta and Harting, 1984; Illing and Graybiel, 1986; Illing, 1992; 1996).

Our preliminary report here regarding the basic structure of the SC provides evidence that modules within the SC are preserved broadly within mammals, retaining some of the same organization across all species examined so far.

Lateral geniculate nucleus

The laminated lateral geniculate nucleus is the primary visual relay nucleus in the thalamus, and serves to relay retinal information to direct inputs to striate cortex, as well as extra-striate areas. The LGN receives retinal input from both eyes and has direct projections to area 17. The laminar patterns within the LGN is variable across species, but in mammals each layer is innervated by one eye or the other. Here, we report that the LGN of the NES and CSL closely resembles the LGN of a terrestrial carnivore. In both pinnipeds, there are distinct lightly-stained and cell-sparse septum which separate the darkly-stained and cell-dense layers (A, A1, and C, as well as possible C1 and C2 sublayers).

Overall, the appearance of the LGN in the NES and CSL is consistent with that of the cat and ferret, and has similarities with closely related species such as the weasel and fox. Sketches of the caudal LGN for the NES and two closely related species are shown in Figure 4.14. The divisions of the pinniped LGNs were largely in alignment with those of the cat and ferret. We speculate that as in the cat LGN, layers A and A1 are structurally and functionally matched pairs of inputs from two eyes, with layer A innervated by the contralateral retina and lamina A1 innervated ipsilaterally, and composed of relay X and Y cells, with minimal differences between the two layers (Wilson et al., 1976; Hickey et al., 1977; Wilson et al., 1984; Montero, 1991). We find that representation of the ipsilateral eye appears to be smaller than that of the contralateral eye in the CSL LGN, but such a difference was not obvious for the NES. These findings are

interesting given that layer A represents the complete contralateral visual hemifield while the A1 layer represents only the binocular portion of that hemifield (Kaas et al., 1972). In the mink and weasel, laminae A and A1 are each subdivided (Sanderson, 1974), but we do not see evidence for any pattern similar to this in either pinniped.

Figure 4.14 **Comparative view of the lateral geniculate nucleus. (A)** cat, **(B)** ferret, **(C)** elephant seal, and **(D)** sea lion. The laminar designations for the LGN in the cat comes from Sherman and Guillery (2002) and Sherman (2016), and the ferret from Kawasaki et al. (2004) and Sanchez-Vives et al. (1996). The LGN in the elephant seal and sea lion are from the results of this study. PGN, perigeniculate nucleus; D, dorsal; L, lateral; P, posterior.

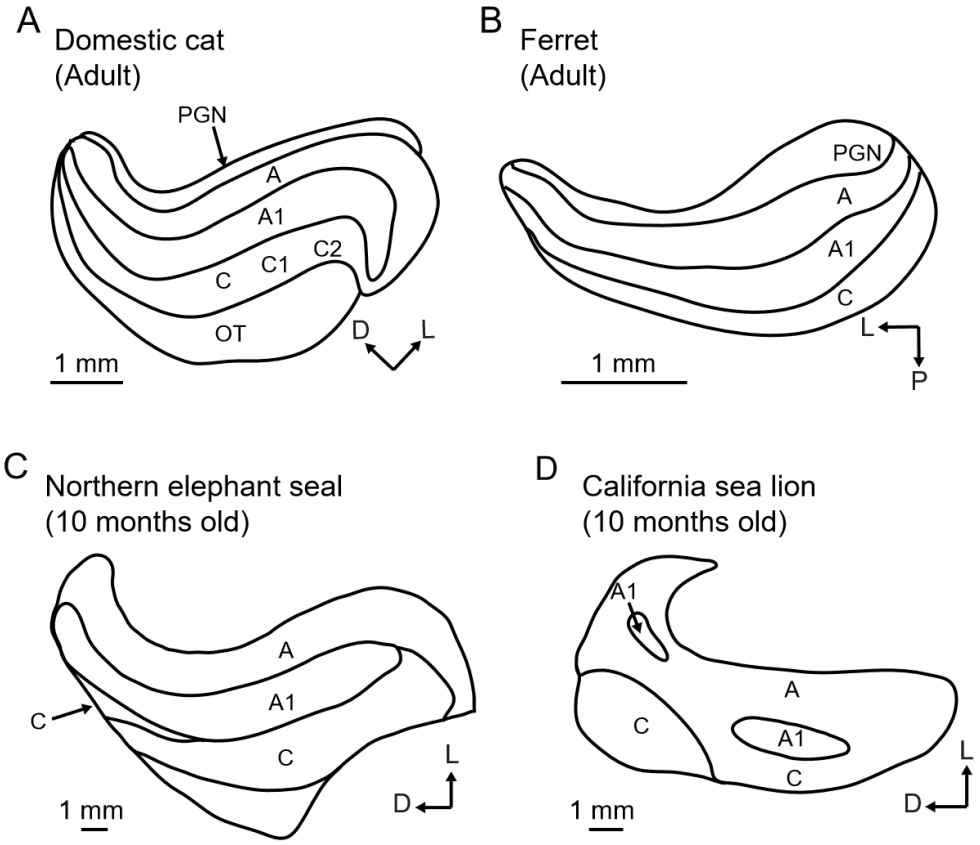

The NES LGN contains certain organized regions within the C layers, with at least 2 distinct subdivisions of the C layer, and we speculate that there are likely C1 and C2 divisions. It has been reported in some carnivore species that the subdivisions of the C layer cannot be identified using the Nissl stain (Guillery, 1971), which may explain why we were not able to identify further sublayers if they are present. However, in some species, such as the fox, all 5 layers are easily identifiable (Kaas et al., 1972). Some obvious problems arise by studying the LGN in a two-dimensional section given the segregation of some layers. For example, the dog was only thought to have two layers in the MIN (Morimoto et al., 1984), a contralateral and ipsilateral, until Lee et al. (1999) were able to reconstruct the dog LGN in a three dimensional form. While we could not identify definitive borders for MIN, we speculate that it is present in both the CSL and NES LGN as it has been described in many families of mammalian carnivores that have specializations for dimly lit environments, and it is likely located near layer C. The organization of the perigeniculate nucleus (PGN) is not consistent among carnivores, as it is a thin layer in the cat and fox but thicker in the weasel and raccoon (Sanderson, 1974). It is unknown whether this nucleus is present in a pinniped, as we did not find evidence for it in these histochemical preparations.

Future studies of the pinniped thalamus could certainly reveal more, but our results are the first to detail the basic organization of the lateral geniculate body in a pinniped. The evidence presented here that suggests there are distinct structural and corresponding functional streams in the pinniped LGN lends support to the fact that vision is important in these species. With more detailed investigation of the NES and CSL thalamus (e.g., different cutting plane) it will be possible to mark further divisions of the C layer, as we hypothesize that it contains just as many subdivisions as in the cat or fox LGN (layers C, C1, and C2). This would be interesting to

investigate, as it would reveal whether these are modules that have been generally preserved within the carnivore order despite different visual demands.

Visual cortex

Our study is one of the first to report on the neuroanatomy of visual cortex in both the CSL and the NES. There have been some efforts to describe and label the external anatomy of CSL brains (Murie, 1874; Montie et al., 2009), but no such efforts involving the NES. The labeling of major sulci in this study was therefore conservative, in which we only labeled major sulci that appear to have clear homologues in other carnivores (cats: Snider and Niemer (1961) and dogs: Singer (1962); Dua-Sharma et al. (1970)), those that bordered the presumptive primary visual cortex, or those that had been previously identified in Sawyer et al. (2016) or Montie et al. (2009). However, many of the sulci in the CSL and NES brain are unique to pinnipeds.

The sulcal patterns and location of primary visual cortex for the CSL, NES, and two closely related species are shown in Figure 4.15. The location of primary somatosensory cortex is also shown when available for comparative purposes. The location of the presumptive primary visual region in the NES and CSL generally corresponds to that of terrestrial carnivores with some select differences. The lateral sulcus is one of the few posterior sulci near primary visual cortex that is present in each species, but the relationship between the location of the sulcus and primary visual cortex varies slightly. It is known that area 17 resides far more anteriorly and medially in cats than in ferrets (Law et al., 1988), but are otherwise similar. In the cat and ferret brains, area 17 only encroaches on the lateral and postlateral sulcus, wraps around the caudal pole, traverses the suprasplenial sulcus (i.e., occipitotemporal sulcus in ferret), and terminates on the caudal bank of the splenial sulcus (Sanides and Hoffmann, 1969; Law et al., 1988). In each

pinniped, the lateral sulcus serves as a dorsolateral border of primary visual cortex, while in the cat and ferret, area 17 does not extend as far laterally as the lateral sulcus. The caudal pole of the CSL primary visual cortex more closely resembles that of the ferret, as it extends to the inferior part of the caudal pole, while primary visual cortex is only identifiable in the superior half of the caudal pole in the NES and cat brains. In both pinnipeds, but more so in the NES, primary visual cortex extends far along the anterior surface. The CSL primary visual cortex does not extend far down the medial wall, as it is bordered inferiorly by the splenial sulcus. While the splenial sulcus also serves as an inferior border to primary visual cortex in the NES, the splenial sulcus is located more posteriorly compared to the CSL brain. The most significant difference between the two pinnipeds is that the CSL primary visual cortex largely lies on the mesial surface along the posterior lateral sulcus, which was a landmark not observable or as distinctive in the NES brain.

In the cat brain, however, LGN cells are known to project not only to area 17 but also to other visual areas, such as area 18. While X cell afferents are rare in area 18, Y afferents are heavily dispersed in the upper part of layer 4. Since these connections also likely use VGluT2 as their primary glutamate neurotransmitter, we would expect to see moderate-to-dense VGluT2 protein immunoreactivity in layer 4 of area 18. Sections of cat neocortex, where definitive area 17 and 18 borders are known, stained for VGluT2 protein confirm that there is strongly VGluT2 immunoreactivity in layer 4 of area 18, but there is a change in intensity at the 17/18 border (unpublished). Consequently, our primary visual cortex region likely includes areas 17 and 18, but no clear difference in the intensity of VGluT2 protein immunoreactivity was identified to distinguish area 17 from area 18.

There are few electrophysiological studies involving pinnipeds, and even less involving recordings from primary visual cortex. The species most closely related to the animals in this

Figure 4.15 **Comparative view of primary visual cortex. (A)** cat, **(B)** ferret, **(C)** dog, **(D)** northern elephant seal, and **E:** California sea lion. The sulcal patterns of the cat brain are based off the works of Snider and Niemer (1961), the ferret brain from Manger et al. (2002) and Innocenti et al. (2002), respectively, and the dog brain from Singer (1962). The region for area 17 in the cat comes from Sanides and Hoffmann (1969) and Scannell et al. (1995), the ferret from Law et al. (1988), and the dog from (Ofri et al., 1994). Primary visual cortex (areas 17 + 18) in the sea lion and elephant seal are from the results of this study. The region for primary somatosensory cortex (area 3b) in the cat comes from Felleman et al. (1983), in the ferret from Leclerc et al. (1993) and Rice et al. (1993), in the dog from Bromiley et al. (1956), and in the sea lion from (Sawyer et al., 2016). AS, ansate sulcus; CrS, cruciate sulcus; CoS, coronal sulcus; EcS, ectolateral sulcus; EsS, ectosylvian sulcus; EnS, entolateral sulcus; LS, lateral sulcus; PLS, posterior lateral sulcus; PS, pseudosylvian sulcus; RS, rhinal sulcus; Sp, splenial sulcus; SuS, suprasplenial sulcus; SS, suprasylvian sulcus; C, caudal; D, dorsal; S1, primary somatosensory cortex; V1, primary visual cortex.

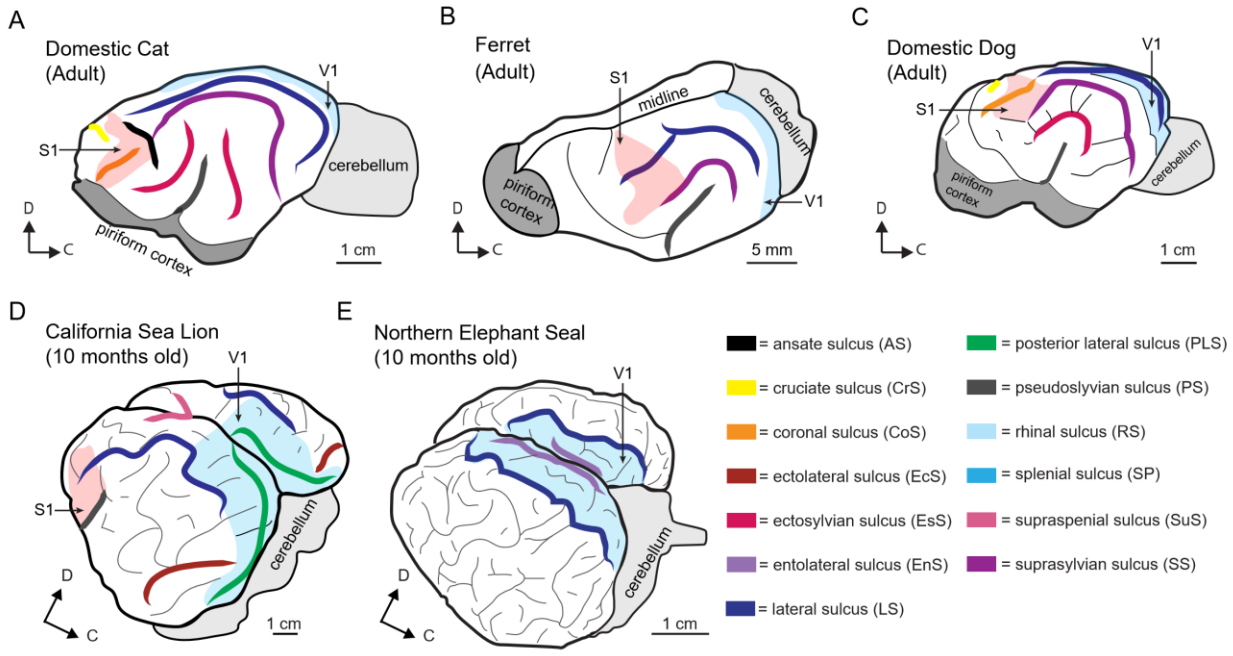

study for which electrophysiological recordings of primary visual cortex exists is the Weddell seal pup (Gruenau and Shurley, 1976). In this study, Gruenau and Shurley recorded visually

evoked responses (VER), electrical potentials recorded after brief visual stimuli, from pups three to 365 days old, but they only recorded from the surface of two sites in primary visual cortex and reported that VERs were confined to visual and visual association areas, even in the older individuals. This contrasts from the similar sized-brain of terrestrial humans, where VERs can be recorded at 12 weeks old outside of the occipital region. However, it is less likely that these results are reflective of an underdeveloped visual system, and more likely are a result of undetected responses from deep pseudo-gyri underneath the surface.

The current study, which delineates the boundaries of primary visual cortex in two pinniped species, will be useful for future studies. It is unclear how area 17 in the Weddell seal was defined by Gruenau and Shurley (1976) as the entire brain was not mapped functionally. Similarly, in a more recent study which counted the number of neurons and glial cells in the harp seal (Walloe et al., 2010), they base their definition of area 17 off the uncertain boundaries reported by Gruenau and Shurley (1976). Despite similarities in the general location of primary visual areas, our results provide further evidence that each brain has a different pattern of gyri, so that histological data is needed to precisely demarcate boundaries of visual areas.

Conclusions

To our knowledge this is the first detailed report on the subcortical and cortical visual components of the NES and CSL brains. Their visual systems are adapted to function in their amphibious environments. We have described the pathway in which visual information in processed, beginning at the optic nerve and continuing through the visual thalamus to visual cortex. The pinniped visual system is of interest due to evidence that this system may work in

conjunction with somatosensation for foraging. Our methodologies in counting cranial nerve II myelinated axons have provided the most accurate and comprehensive results to date. We also show that the cytoarchitectonic features of the LGN and primary visual cortex are extraordinarily similar in both pinniped brains and that they resemble these same structures in closely related terrestrial carnivores. The identification of the primary region which likely includes areas 17 and 18 in both the CSL and NES brains facilitates comparisons with other mammals with large brains. Overall, the visual systems of seals and sea lion share many conserved components of the central nervous systems of other mammals.

REFERENCES

Arey L, Schaible A (1934) The nerve-fiber composition of the optic nerve. Anat Rec 58:3.

Balaram P, Hackett TA, Kaas JH (2013) Differential expression of vesicular glutamate transporters 1 and 2 may identify distinct modes of glutamatergic transmission in the macaque visual system. J Chem Neuroanat 50-51:21-38.

Balaram P, Isaamullah M, Petry HM, Bickford ME, Kaas JH (2015) Distributions of vesicular glutamate transporters 1 and 2 in the visual system of tree shrews (Tupaia belangeri). J Comp Neurol 523:1792-1808.

Balaram P, Takahata T, Kaas JH (2011) VGLUT2 mRNA and protein expression in the visual thalamus and midbrain of prosimian galagos (Otolemur garnetti). Eye Brain 2011:5-15.

Balazsi AG, Rootman J, Drance SM, Schulzer M, Douglas GR (1984) The effect of age on the nerve fiber population of the human optic nerve. Am J Ophthalmol 97:760-766.

Baldwin MK, Balaram P, Kaas JH (2013) Projections of the superior colliculus to the pulvinar in prosimian galagos (Otolemur garnettii) and VGLUT2 staining of the visual pulvinar. J Comp Neurol 521:1664-1682.

Bishop G, O'Leary J (1938) Potential records from the optic cortex of the cat. J Neurophysiol 1:391-404.

Blackwell S, Le Boeuf B (1993) Developmental aspects of sleep apnoea in northern elephant seals, Mirounga angustirostris. J Zool 231:437-447.

Bowmaker JK (1995) The visual pigments of fish. Prog Retinal Eye Res 15:31.

Bowmaker JK (1998) Evolution of colour vision in vertebrates. Eye (Lond) 12 (Pt 3b):541-547.

Braekevelt CR (1986) Fine structure of the tapetum cellulosum of the grey seal (Halichoerus grypus). Acta Anat (Basel) 127:81-87.

Bromiley RB, Pinto Hamuy T, Woolsey CN (1956) Somatic afferent areas I and II of dog's cerebral cortex. J Neurophysiol 19:485-499.

Bruesch S, Arey L (1942) The number of myelinated and unmyelinated fibers in the optic nerve of vertebrates. Journal of Comparative Neurol 88:631-665.

Casagrande VA, Harting JK, Hall WC, Diamond IT, Martin GF (1972) Superior colliculus of the tree shrew: a structural and functional subdivision into superficial and deep layers. Science 177:444-447.

Casagrande VA, Norton TT (1991) Lateral geniculate nucleus: a review of its physiology and function. . In: Vision and Visual Dysfunction, vol. 4 (Leventhal, A. G., ed) New York: Macmillan Press.

Cleland BG, Levick WR (1974) Brisk and sluggish concentrically organized ganglion cells in the cat's retina. J Physiol 240:421-456.

Daw NW, Pearlman AL (1970) Cat colour vision: evidence for more than one cone process. J Physiol 211:125-137.

Dawson W (1980) The cetacean eye. In: Cetacean behavior: mechanisms and functions (Herman, L., ed), pp 53-100 New York: Wiley.

Dawson W, Schroeder J, Sharpe S (1987) Corneal surface properties of two marine mammals. Mar Mammal Sci 3:186-197.

Dehnhardt G, Mauck B, Hanke W, Bleckmann H (2001) Hydrodynamic trail-following in harbor seals (Phoca vitulina). Science 293:102-104.

Dehnhardt G, Mauck B, Hyvarinen H (1998) Ambient temperature does not affect the tactile sensitivity of mystacial vibrissae in harbour seals. J Exp Biol 201:3023-3029.

Dondzillo A, Satzler K, Horstmann H, Altrock WD, Gundelfinger ED, Kuner T (2010) Targeted three-dimensional immunohistochemistry reveals localization of presynaptic proteins Bassoon and Piccolo in the rat calyx of Held before and after the onset of hearing. J Comp Neurol 518:1008-1029.

Donovan A (1967) The nerve fibre composition of the cat optic nerve. J Anat 101:1-11.

Dua-Sharma S, Sharma K, Jacobs H (1970) The canine brain in stereotaxic coordinates. Cambridge: MIT Press.

Edwards SB (1980) The deep cell layers of the superior colliculus: their reticular characteristics and structural organization. In: The reticular formation revisited (Hobson, J. A. and Brazier, M. A. B., eds), pp 193-209 New York: Raven Press.

Edwards SB, Ginsburgh CL, Henkel CK, Stein BE (1979) Sources of subcortical projections to the superior colliculus in the cat. J Comp Neurol 184:309-329.

Fasick JI, Robinson PR (2000) Spectral-tuning mechanisms of marine mammal rhodopsins and correlations with foraging depth. Vis Neurosci 17:781-788.

Feldkamp S, DeLong R, Antonelis G (1989) Diving patterns of California sea lions, *Zalophus californianus*. Can J Zool 67:872-883.

Felleman DJ, Wall JT, Cusick CG, Kaas JH (1983) The representation of the body surface in S-I of cats. J Neurosci 3:1648-1669.

Fish P (1898) The brain of the fur seal, callorhinus ursinus; with a comparative description of those of *Zalophus californianus, Phoca vitulina, Ursus americanus,* and *Monachus tropicalis.* Journal of Comparative Neurol 8:57-91.

Fitzgibbon T, Reese BE (1996) Organization of retinal ganglion cell axons in the optic fiber layer and nerve of fetal ferrets. Vis Neurosci 13:847-861.

Folkow L, Blix A (1999) Diving behaviour of hooded seal (*Cystophora cristata*) in the Greenland and Norwegian Seas. Polar Biol 22:61-74.

Fukuda Y (1971) Receptive field organization of cat optic nerve fibers with special reference to conduction velocity. Vision Res 11:209-226.

Fukuda Y, Hsiao CF, Watanabe M (1985) Morphological correlates of Y, X and W type ganglion cells in the cat's retina. Vision Res 25:319-327.

Glaser N, Wieskotten S, Otter C, Dehnhardt G, Hanke W (2011) Hydrodynamic trail following in a California sea lion (Zalophus californianus). J Comp Physiol A Neuroethol Sens Neural Behav Physiol 197:141-151.

Gong J, Jellali A, Mutterer J, Sahel JA, Rendon A, Picaud S (2006) Distribution of vesicular glutamate transporters in rat and human retina. Brain Res 1082:73-85.

Graham J (1977) An autoradiographic study of the efferent connections of the superior colliculus in the cat. J Comp Neurol 173:629-654.

Graybiel AM (1975) Anatomical organization of retinotectal afferents in the cat: an autoradiographic study. Brain Res 96:1-23.

Graybiel AM (1976) Evidence for banding of the cat's ipsilateral retinotectal connection. Brain Res 114:318-327.

Graziano A, Liu XB, Murray KD, Jones EG (2008) Vesicular glutamate transporters define two sets of glutamatergic afferents to the somatosensory thalamus and two thalamocortical projections in the mouse. J Comp Neurol 507:1258-1276.

Griebel U, Peichl L (2003) Colour vision in aquatic mammals- facts and open questions. Aquatic Mammals 29:18-30.

Gruenau SP, Shurley JT (1976) Visual evoked response (VER) changes during maturation in the Weddell seal. Dev Psychobiol 9:477-493.

Guillery RW (1971) Patterns of synaptic interconnections in the dorsal lateral geniculate nucleus of cat and monkey: a brief review. Vision Res Suppl 3:211-227.

Guillery RW, Kaas JH (1971) A study of normal and congenitally abnormal retinogeniculate projections in cats. J Comp Neurol 143:73-100.

Hanke FD, Hanke W, Scholtyssek C, Dehnhardt G (2009) Basic mechanisms in pinniped vision. Exp Brain Res 199:299-311.

Harting JK, Hall WC, Diamond IT, Martin GF (1973) Anterograde degeneration study of the superior colliculus in Tupaia glis: evidence for a subdivision between superficial and deep layers. J Comp Neurol 148:361-386.

Hassrick JL, Crocker DE, Zeno R, Blackwell S, Costa DP, Le Boeuf B (2007) Swimming speed and foraging strategies of northern elephant seals. Deep Sea Res Part 2 Top Study Oceanoger 54:369-383.

Hendry SH, Reid RC (2000) The koniocellular pathway in primate vision. Annu Rev Neurosci 23:127-153.

Hickey TL, Spear PD, Kratz KE (1977) Quantitative studies of cell size in the cat's dorsal lateral geniculate nucleus following visual deprivation. J Comp Neurol 172:265-281.

Hoffmann KP (1973) Conduction velocity in pathways from retina to superior colliculus in the cat: a correlation with receptive-field properties. J Neurophysiol 36:409-424.

Huerta M, Harting J (1984) The mammalian superior colliculus studies of its morphology and connections. In: Comparative neurology of the optic tectum (Vanegas, H., ed), pp 687-773 New York: Plenum.

Hunt DM, Fitzgibbon J, Slobodyanyuk SJ, Bowmaker JK (1996) Spectral tuning and molecular evolution of rod visual pigments in the species flock of cottoid fish in Lake Baikal. Vision Res 36:1217-1224.

Illing RB (1992) Association of efferent neurons to the compartmental architecture of the superior colliculus. Proc Natl Acad Sci U S A 89:10900-10904.

Illing RB (1996) The mosaic architecture of the superior colliculus. Prog Brain Res 112:17-34.

Illing RB, Graybiel AM (1986) Complementary and non-matching afferent compartments in the cat's superior colliculus: innervation of the acetylcholinesterase-poor domain of the intermediate gray layer. Neuroscience 18:373-394.

Innocenti GM, Manger PR, Masiello I, Colin I, Tettoni L (2002) Architecture and callosal connections of visual areas 17, 18, 19 and 21 in the ferret (Mustela putorius). Cereb Cortex 12:411-422.

Jamieson G, Fisher H (1971) The retina of the harbour seal, *Phoca vitulina*. Can J Zool 49:19-23.

Kaas JH, Guillery RW, Allman JM (1972) Some principles of organization in the dorsal lateral geniculate nucleus. Brain, Behavior, Evolution 6:253-299.

Kaas JH, Guillery RW, Allman JM (1973) Discontinuities in the dorsal lateral geniculate nucleus corresponding to the optic disc: a comparative study. J Comp Neurol 147:163-179.

Kaas JH, Huerta M (1988) Subcortical visual system of primates. In: Comparative Primate Biology, vol. 4: Neurosciences (Steklis, H. P., ed) New York: Alan R Liss, Inc.

Kanaseki T, Sprague JM (1974) Anatomical organization of pretectal nuclei and tectal laminae in the cat. J Comp Neurol 158:319-337.

Kaneko T, Fujiyama F (2002) Complementary distribution of vesicular glutamate transporters in the central nervous system. Neurosci Res 42:243-250.

Kawasaki H, Crowley JC, Livesey FJ, Katz LC (2004) Molecular organization of the ferret visual thalamus. J Neurosci 24:9962-9970.

Kuhn CE, Crocker DE, Tremblay Y, Costa DP (2009) Time to eat: measurements of feeding behaviour in a large marine predator, the northern elephant seal Mirounga angustirostris. J Anim Ecol 78:513-523.

Ladygina TF, Popov VV, Supin A (1985) [Topical organization of somatic projections to the cerebral cortex of the seal Callorhinus ursius]. Neirofiziologiia 17:344-351.

Laemle LK (1981) A Golgy study of cellular morphology in the superficial layers of superior colliculus man, Saimiri, and Macaca. J Hirnforsch 22:253-263.

Laemle LK (1983) A Golgi study of cell morphology in the deep layers of the human superior colliculus. J Hirnforsch 24:297-306.

Law MI, Zahs KR, Stryker MP (1988) Organization of primary visual cortex (area 17) in the ferret. J Comp Neurol 278:157-180.

Le Boeuf B, Costa D, Huntley A, Feldkamp S (1988) Continuous, deep diving in female Northern seals, *Mirounga angustirostris*. Can J Zool 66:446-458.

Leclerc SS, Rice FL, Dykes RW, Pourmoghadam K, Gomez CM (1993) Electrophysiological examination of the representation of the face in the suprasylvian gyrus of the ferret: a correlative study with cytoarchitecture. Somatosens Mot Res 10:133-159.

Lee C, Malpeli JG, Schwark HD, Weyand TG (1984) Cat medial interlaminar nucleus: retinotopy, relation to tapetum and implications for scotopic vision. J Neurophysiol 52:848-869.

Lee I, Kim J, Lee C (1999) Anatomical characteristics and three-dimensional model of the dog dorsal lateral geniculate body. Anat Rec 256:29-39.

Levenson DH, Dizon A (2003) Genetic evidence for the ancestral loss of short-wavelength-sensitive cone pigments in mysticete and odontocete cetaceans. Proc Biol Sci 270:673-679.

Levenson DH, Ponganis PJ, Crognale MA, Deegan JF, 2nd, Dizon A, Jacobs GH (2006) Visual pigments of marine carnivores: pinnipeds, polar bear, and sea otter. J Comp Physiol A Neuroethol Sens Neural Behav Physiol 192:833-843.

Levenson DH, Schusterman RJ (1997) Pupillometry in seals and sea lions: ecological implications. Can J Zool 75:2050-2057.

Levenson DH, Schusterman RJ (1999) Dark adaptation and visual sensitivity in shallow and deep-diving pinnipeds. Marine Mammal Science 15:1303-1313.

Liguz-Lecznar M, Skangiel-Kramska J (2007) Vesicular glutamate transporters VGLUT1 and VGLUT2 in the developing mouse barrel cortex. Int J Dev Neurosci 25:107-114.

Louderback KM, Glass CS, Shamalla-Hannah L, Erickson SL, Land PW (2006) Subbarrel patterns of thalamocortical innervation in rat somatosensory cortical barrels: Organization and postnatal development. J Comp Neurol 497:32-41.

Lund RD, Land PW, Boles J (1980) Normal and abnormal uncrossed retinotectal pathways in rats: an HRP study in adults. J Comp Neurol 189:711-720.

Manger PR, Kiper D, Masiello I, Murillo L, Tettoni L, Hunyadi Z, Innocenti GM (2002) The representation of the visual field in three extrastriate areas of the ferret (Mustela putorius) and the relationship of retinotopy and field boundaries to callosal connectivity. Cereb Cortex 12:423-437.

Mass AM, Supin AY (1992) Peak density, size and regional distribution of ganglion cells in the retina of the fur seal Callorhinus ursinus. Brain Behav Evol 39:69-76.

Mass AM, Supin AY (2003) Retinal topography of the harp seal Pagophilus groenlandicus. Brain Behav Evol 62:212-222.

Mass AM, Supin AY (2005) Ganglion cell topography and retinal resolution of the Steller sea lion (*Eumetopias jubatus*). Aquatic Mammals 31:393-402.

Mass AM, Supin AY (2007) Adaptive features of aquatic mammals' eye. Anat Rec (Hoboken) 290:701-715.

May PJ (2006) The mammalian superior colliculus: laminar structure and connections. Prog Brain Res 151:321-378.

McFarland WN (1971) Cetacean visual pigments. Vision Res 11:1065-1076.

McGovern KA, Marshall CD, Davis RW (2015) Are vibrissae viable sensory structures for prey capture in northern elephant seals, Mirounga angustirostris? Anat Rec (Hoboken) 298:750-760.

Miller SN, Colitz CM, Dubielzig RR (2010) Anatomy of the California sea lion globe. Vet Ophthalmol 13:63-71.

Milne AO, Grant RA (2014) Characterisation of whisker control in the California sea lion (Zalophus californianus) during a complex, dynamic sensorimotor task. J Comp Physiol A Neuroethol Sens Neural Behav Physiol 200:871-879.

Montero V (1991) A quantitative study of synaptic contacts on interneurons and relay cells of the cat lateral geniculate nucleus. Exp Brain Res 86.

Montie EW, Pussini N, Schneider GE, Battey TW, Dennison S, Barakos J, Gulland F (2009) Neuroanatomy and volumes of brain structures of a live California sea lion (Zalophus californianus) from magnetic resonance images. Anat Rec (Hoboken) 292:1523-1547.

Morimoto M, Kubota T, Miyahara H, Kanaseki T (1984) The laminar structures and axon terminals of retinal fibers of the dorsal lateral geniculate nucleus of the dog: a study by a horseradish peroxidase method. Fukuoka Igaku Zasshi 75:633-644.

Munoz DP, Guitton D (1985) Tectospinal neurons in the cat have discharges coding gaze position error. Brain Res 341:184-188.

Munoz DP, Guitton D (1989) Fixation and orientation control by the tecto-reticulo-spinal system in the cat whose head is unrestrained. Rev Neurol (Paris) 145:567-579.

Murie J (1874) Researches upon the anatomy of the Pinnipedia-Part III. Descriptive anatomy of the sea-lion (Otaria jubata). Transact Zool Soc Lond 8:501-582.

Nagy A, Ronald K (1970) The harp seal, *Pagophilus groenlandicus* (Erxleben 1777). Can J Zool 48:367-370.

Nagy A, Ronald K (1975) A light and electron microscopic study of the structure of the retina of the harp seal *Pagophilus groenlandicus* (Erxleben 1777). Rapports et Proces-verbaux des Réunions Conseil International pour l'Éxploration de la Mer 169:92-96.

Nahmani M, Erisir A (2005) VGluT2 immunochemistry identifies thalamocortical terminals in layer 4 of adult and developing visual cortex. J Comp Neurol 484:458-473.

Ninomiya H (2016) Microvasculature of the California sea lion (Zalophus californianus) eye and its functional significance. Vet Ophthalmol.

Norita M (1980) Neurons and synaptic patterns in the deep layers of the superior colliculus of the cat. A Golgi and electron microscopic study. J Comp Neurol 190:29-48.

Ofri R, Dawson W, Samuelson DA (1994) Mapping of the cortical area of central vision in dogs. JProg Comp Vet Ophthalmol 4:172-178.

Ollivier FJ, Samuelson DA, Brooks DE, Lewis PA, Kallberg ME, Komaromy AM (2004) Comparative morphology of the tapetum lucidum (among selected species). Vet Ophthalmol 7:11-22.

Peichl L, Behrmann G, Kroger RH (2001) For whales and seals the ocean is not blue: a visual pigment loss in marine mammals. Eur J Neurosci 13:1520-1528.

Petry HM, Agarwala S, May JG, 3rd (1989) Striped pattern of labeling in ground squirrel superior colliculus following intraocular HRP injections. Brain Res 489:199-203.

Pollack JG, Hickey TL (1979) The distribution of retino-collicular axon terminals in rhesus monkey. J Comp Neurol 185:587-602.

Price DJ (1985) Patterns of cytochrome oxidase activity in areas 17, 18 and 19 of the visual cortex of cats and kittens. Exp Brain Res 58:125-133.

Putter A (1902) Die Augen der Wassersaugetiere. Zoologische Jahrbücher Abteilung für Anatomie und Ontogenie der Tiere Abteilung für Anatomie und Ontogenie der Tiere 17:99-402.

Qi HX, Gharbawie OA, Wong P, Kaas JH (2011) Cell-poor septa separate representations of digits in the ventroposterior nucleus of the thalamus in monkeys and prosimian galagos. J Comp Neurol 519:738-758.

Rice FL, Gomez CM, Leclerc SS, Dykes RW, Moon JS, Pourmoghadam K (1993) Cytoarchitecture of the ferret suprasylvian gyrus correlated with areas containing multiunit responses elicited by stimulation of the face. Somatosens Mot Res 10:161-188.

Rioch D (1937) A physiological and histological study of the frontal cortex of the seal *(Phoca vitulina).* Biol Bull 73:591-602.

Rodieck RW (1973) The vertebrate retina; principles of structure and function. San Francisco,: Freeman.

Sakurai K, Akiyama M, Cai B, Scott A, Han BX, Takatoh J, Sigrist M, Arber S, Wang F (2013) The organization of submodality-specific touch afferent inputs in the vibrissa column. Cell Rep 5:87-98.

Sanchez-Vives MV, Bal T, Kim U, von Krosigk M, McCormick DA (1996) Are the interlaminar zones of the ferret dorsal lateral geniculate nucleus actually part of the perigeniculate nucleus? J Neurosci 16:5923-5941.

Sandell JH, Peters A (2001) Effects of age on nerve fibers in the rhesus monkey optic nerve. J Comp Neurol 429:541-553.

Sanders FK, Whitteridge D (1946) Conduction velocity and myelin thickness in regenerating nerve fibres. J Physiol 105:152-174.

Sanderson KJ (1974) Lamination of the dorsal lateral geniculate nucleus in carnivores of the weasel (Mustelidae), raccoon (Procyonidae) and fox (Canidae) families. J Comp Neurol 153:238-266.

Sanides F, Hoffmann J (1969) Cyto- and myeloarchitecture of the visual cortex of the cat and of the surrounding integration cortices. J Hirnforsch 11:79-104.

Sawyer EK, Liao CC, Qi HX, Balaram P, Matrov D, Kaas JH (2015) Subcortical barrelette-like and barreloid-like structures in the prosimian galago (Otolemur garnetti). P Natl Acad Sci USA 112:7079-7084.

Sawyer EK, Turner EC, Kaas JH (2016) Somatosensory brainstem, thalamus, and cortex of the California sea lion (Zalophus californianus). J Comp Neurol 524:1957-1975.

Scannell JW, Blakemore C, Young MP (1995) Analysis of connectivity in the cat cerebral cortex. J Neurosci 15:1463-1483.

Schusterman RJ (1981) Visual acuities in pinnipeds. Psychological Record 31:125-143.

Schusterman RJ (2006) Aerial and underwater visual acuity in the California sea lion (Zalophus californianus) as a function of luminance. Annals New York Academy of Sciences 188:37-46.

Sherman S (1985) Functional organization of the W-cell, X-cell, and Y-cell pathways in the cat - a review and hypothesis. Prog Psychobiol Physiol Psych 11:233-314.

Sherman SM (2016) Thalamus plays a central role in ongoing cortical functioning. Nat Neurosci 19:533-541.

Sherman SM, Guillery RW (2002) The role of the thalamus in the flow of information to the cortex. Philos Trans R Soc Lond B Biol Sci 357:1695-1708.

Sherman SM, Guillery RW (2004) Thalamus. In: The synaptic organization of the brain (Shepherd, G., ed), pp 311-359 New York: Oxford UP.

Singer M (1962) The brain of the dog in section. Philadelphia: Saunders.

Snider R, Niemer W (1961) A stereotaxic atlas of the cat brain. Chicago: University of Chicago Press.

Stewart B, DeLong R (1995) Double migrations of the northern elephant seal, *Mirounga angustirostris.* J Mammal 76:196-205.

Stone J (1965) A quantitative analysis of the distribution of ganglion cells in the cat's retina. J Comp Neurol 124:337-352.

Stone J (1983) Parallel processing in the visual system : the classification of retinal ganglion cells and its impact on the neurobiology of vision. New York: Plenum Press.

Stone J, Dreher B (1973) Projection of X- and Y-cells of the cat's lateral geniculate nucleus to areas 17 and 18 of visual cortex. J Neurophysiol 36:551-567.

Turner W, Miller W (1880) Report on the seals collected during the voyage of *H.M.S. Challenger* in the years 1873-76. Edinburgh: Neill & Company.

Viktorov IV (1968) Neuronal structure of superior colliculus of the lamina quadrigemina in the cat. Arkh Anat Gistol Embriol 54:45-55.

Walloe S, Eriksen N, Dabelsteen T, Pakkenberg B (2010) A neurological comparative study of the harp seal (Pagophilus groenlandicus) and harbor porpoise (Phocoena phocoena) brain. Anat Rec (Hoboken) 293:2129-2135.

Welsch U, Ramdohr S, Riedelsheimer B, Hebel R, Eisert R, Plotz J (2001) Microscopic anatomy of the eye of the deep-diving Antarctic Weddell seal (Leptonychotes weddellii). J Morphol 248:165-174.

Wieskotten S, Dehnhardt G, Mauck B, Miersch L, Hanke W (2010) Hydrodynamic determination of the moving direction of an artificial fin by a harbour seal (Phoca vitulina). J Exp Biol 213:2194-2200.

Wieskotten S, Mauck B, Miersch L, Dehnhardt G, Hanke W (2011) Hydrodynamic discrimination of wakes caused by objects of different size or shape in a harbour seal (Phoca vitulina). J Exp Biol 214:1922-1930.

Wilson A (1970) Vision of the Weddell seal (Leptonychotes weddelli). In: Antarctic Ecology, vol. 1 (Holdgate, M., ed), pp 490-494.

Wilson JR, Friedlander MJ, Sherman SM (1984) Fine structural morphology of identified X- and Y-cells in the cat's lateral geniculate nucleus. Proc R Soc Lond B Biol Sci 221:411-436.

Wilson PD, Rowe MH, Stone J (1976) Properties of relay cells in cat's lateral geniculate nucleus: a comparison of W-cells with X- and Y-cells. J Neurophysiol 39:1193-1209.

Wohlert D, Kroger J, Witt M, Schmitt O, Wree A, Czech-Damal N, Siebert U, Folkow L, Hanke FD (2016) A Comparative Morphometric Analysis of Three Cranial Nerves in Two Phocids: The Hooded Seal (Cystophora cristata) and the Harbor Seal (Phoca vitulina). Anat Rec (Hoboken) 299:370-378.

Wojcik SM, Rhee JS, Herzog E, Sigler A, Jahn R, Takamori S, Brose N, Rosenmund C (2004) An essential role for vesicular glutamate transporter 1 (VGLUT1) in postnatal development and control of quantal size. Proc Natl Acad Sci U S A 101:7158-7163.

Wong-Riley M (1979) Changes in the visual system of monocularly sutured or enucleated cats demonstrable with cytochrome oxidase histochemistry. Brain Res 171:11-28.

Wong P, Kaas JH (2008) Architectonic subdivisions of neocortex in the gray squirrel (Sciurus carolinensis). Anat Rec (Hoboken) 291:1301-1333.

Wong P, Kaas JH (2009) Architectonic subdivisions of neocortex in the tree shrew (Tupaia belangeri). Anat Rec (Hoboken) 292:994-1027.

Young N, Hope G, Dawson W, Jenkins R (1988) The tapetum fibrosum in the eyes of two small whales. Marine Mammal Science 4.

Zhang HY, Hoffmann KP (1993) Retinal projections to the pretectum, accessory optic system and superior colliculus in pigmented and albino ferrets. Eur J Neurosci 5:486-500.

Zhou J, Nannapaneni N, Shore S (2007) Vesicular glutamate transporters 1 and 2 are differentially associated with auditory nerve and spinal trigeminal inputs to the cochlear nucleus. J Comp Neurol 500:777-787.

CHAPTER 5

CONCLUSIONS

Summary

The primary goals of Chapters 2 – 4 were to (1) determine the number of total cells and neurons in the neocortex of a chimpanzee and three different macaque species and (2) describe the basic architecture of visual pathway structures in the northern elephant seal and California sea lion. The reports of the total number of cells and neurons in the chimpanzee and macaque are largely consistent with previous studies in other Old World monkeys, New World monkeys, and prosimian galagos (Collins et al., 2010; Collins, 2011; Young et al., 2013a; Young et al., 2013b) that show a consistent pattern of neuron densities that are higher in the posterior visual areas of cortex, and lower neuron densities towards the anterior pole of the brain in motor cortex. This pattern has been documented in each primate species studied to date, and suggests that these patterns of neuronal densities are a shared feature of all modern primates. Given these facts, it is evident that the primate neocortex is nonuniform in its distribution of neurons. The original findings of Rockel et al. (1980) and replicated study by Carlo and Stevens (2013) argue for the uniformity of neocortex (with the exception of primary visual cortex). The current results presented here and by others (Herculano-Houzel et al., 2008; Collins et al., 2010; Collins, 2011; Young et al., 2013a; Young et al., 2013b), however, support the nonuniformity of cortex, especially as it pertains to changes in neuron densities in primary somatosensory and motor areas. Thus, this research represents an important contribution to this debate, especially in the

context of recent publications which support the isotropic fractionator method as a technique as reliable and valid as stereology (Bahney and von Bartheld, 2014; Miller et al., 2014).

From the described architectonic features of the visual system of the northern elephant seal and California sea lion, it is evident they share many features with other distantly related carnivores, such as the three-layered structure of the LGN that is present in both pinnipeds and the cat. This research represents the first study to define the architectonic characteristics of the visual system in any pinniped brain. We previously described the somatosensory system of the California sea lion in a recent publication (Sawyer et al., 2016), and future projects seek to report on the somatosensory system in the northern elephant seal and the auditory system in both species. Together, these descriptions of the primary sensory systems in pinnipeds will further our understanding of these mammals' visual and sensory capabilities. Given their marine habitats, the behaviors of these animals are a mystery in many ways. The availability of architectonic knowledge for these species is important for the continued funding and interpretation of behavioral research.

One purpose in the design and implementation of these research projects was to learn more about why and how human brains are so large, and if that one factor even contributes in some way to our better cognitive abilities. This leads to the question of what *is* the determinant of behavioral and cognitive capabilities? However, this is a subject still under investigation. Humans stand out from other species in that we have the highest absolute number of neurons in the cerebral cortex (Herculano-Houzel, 2012; Herculano-Houzel et al., 2014). However, a large brain is not necessarily a proxy for cognitive abilities, as birds (songbirds and parrots) have greater neuronal densities in their forebrain than primates of the same brain mass, despite their smaller brains (0.36 – 21.81 grams; 28 avian species) (Olkowicz et al., 2016). Birds, in particular

corvids and parrots, have been shown to have some cognitive abilities that match those of humans, including abilities such as recognizing themselves in a mirror (Prior et al., 2008), planning for the future (Raby et al., 2007), and manufacturing tools (Weir et al., 2002). The large numbers of neurons that are concentrated in high densities likely contribute to the neural basis of intelligence in both birds and primates. Therefore, absolute brain size might not be the best predictor of cognitive capacity.

It remains unclear still as to what makes the human brain special, and if it truly is special (Azevedo et al., 2009). Or, if the human brain would be special regardless of its size. The scaling rules which apply to the primate brain are consistent amongst all hominins, including simians, great apes, and humans (Herculano-Houzel and Kaas, 2011). One interesting consideration in the discussion of primate brain size is body size, as while the scaling rules for the brain have remained the same throughout primate evolution, it does not appear so for the primate body, as exhibited through the discrepancy in body size between humans and great apes. The common idea is that humans evolved a brain too large for their body, but this is a misguided opinion, that could instead be thought about in the framework that great apes instead evolved a larger body (Herculano-Houzel and Kaas, 2011). Humans may have been able to "afford" a larger brain speculatively due to of the invention of cooking, which provides more energy in less time, in contrast to great apes who have a metabolic limitation imposed by their diets (Fonseca-Azevedo and Herculano-Houzel, 2012). In considering body size, great apes may have evolved to have larger bodies from large quantities of less nutritional food due to pressures from sexual selection, such as females preferring larger males (Herculano-Houzel and Kaas, 2011).

Likewise with body size, the degree of cortical folding may not be correlated with cognitive abilities and number of neurons. Mota and Herculano-Houzel (2015) recently

discovered that cortical expansion and more folded brains are neither a consequence nor requirement for an increasing number of neurons in the mammalian cerebral cortex. Similarly, some outlier species (such as the lissencephalic manatee) do not fit in with the hypothesis that there is a strict relationship between total brain mass and degree of cortical folding. Rather, the degree of folding across all mammalian species occurs as a result of the expanding cortex settling into the most stable configuration, which is dependent on the total surface area and average cortical thickness. Future studies examining the cell and neuronal content of pinniped brains and other large folded brains will certainly reveal more concerning how the number of neurons relates to cortical folding and brain size, and if it plays a determining role or not. Now that the basic visual and somatosensory (Sawyer et al., 2016) neuroanatomy of these animals have been described, studies of cell and neuron counts can be more easily performed.

The visual system of carnivores and primates

The retinogeniculostriate pathway, or the primary visual pathway, is responsible for the transfer of visual information to visual cortex via the retinas. In the simplest overview of this pathway in mammals, visual stimuli are encoded by retinal ganglion cells, and this visual input is transmitted to separate layers of the LGN via the optic nerve. The LGN preserves the retinotopic map of visual stimuli, and finally this information is relayed from the LGN to layers 4 and 6 of primary visual cortex. The research in the preceding chapters sought to describe how this pathway is configured in the northern elephant seal and California sea lion, and whether the visual pathway in those animals even resembles that of other carnivores. In addition, we aimed to build upon our already dense knowledge of the primate visual system that has been studied in

detail over the past century. These research aims together seek to contribute to the long-standing question of how human brains have evolved to become so uniquely complex.

The synaptic connections between retinal ganglion cells and neurons of the LGN have evolved differently across species, and these connections have been extensively studied in primates and cats. In catarrhine primates (Old World monkeys, apes and humans), there are three neuronal streams originating from three primary types of retinal ganglion cells: the large parasol ganglion cells belonging to the magnocellular (M) pathway, the smaller midget ganglion cells of the parvocellular (P) pathway, and the small ganglion cells of the koniocellular (K) pathway. These three different types of retinal ganglion cells project to the corresponding M, P, and K layers of the dorsal LGN, the visual processing relay station before information is transmitted to primary visual cortex. In contrast to primates, the visual system of cats and other carnivores contains X, Y, and W classes of retinal ganglion cells, which correspond to the P, M, and K classes in primates, respectively. The X and Y cells represent the two main classes of ganglion cells which innervate the LGN.

The configuration of the LGN can help determine how the visual system of pinnipeds relates to either other carnivores, such as cats, or a different clade of mammals such as primates. The target of almost all M, P, and K ganglion cells in primates is the LGN (Weller and Kaas, 1989), which is a well-laminated structure with four main layers in primates: two ventral magnocellular layers that receive input from the M class of ganglion cells, and two dorsal parvocellular layers that receive input from the retinal P cells (see Fig. 5.1 for schematic of macaque LGN). Each external M and P layer receives input from the contralateral eye, while the internal M and P layers receive input from the ipsilateral eye. In most primates, the K class of retinal ganglion cells projects to the interlaminar layers of the LGN, apart from nocturnal

prosimian primates, in which the K cells project to two distinct koniocellular layers. In anthropoid primates, such as macaques, the LGN is typically described as having six distinct layers, composed of four parvocellular and two magnocellular layers, although the increase in P layers is more so a result of sublayers. The functions of the P, M, and K systems are thought to be unique, as P cells are involved in fine vision which evolved in anthropoid primates and project exclusively to the LGN, while M cells are thought to play a role in visual change detection. While the role of the K cell system in primates is still somewhat unknown, it is thought to play a role in vision in dim light environments due to the larger K cell layers in prosimian primates and reduced representation in other primates, like the macaque.

Figure 5.1 **The visual thalamus in primates and carnivores**. Sketches adapted from Sherman and Guillery (2002) and Jeffries et al. (2014).

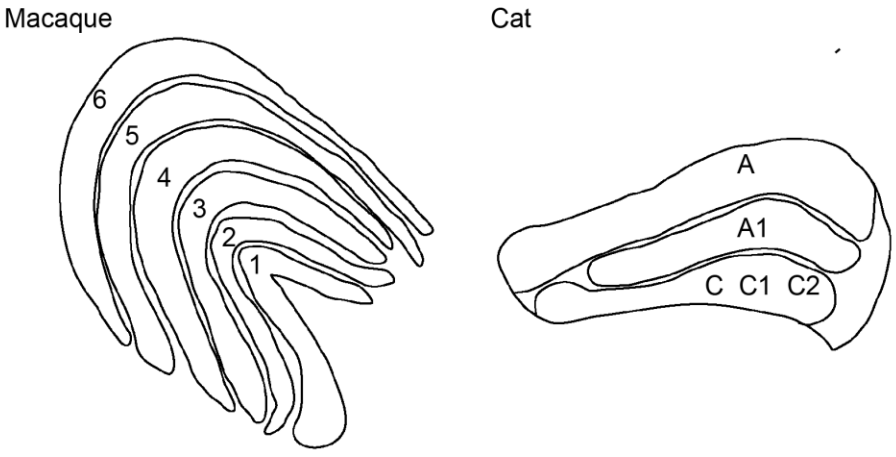

In contrast, the cat LGN is configured differently than in primates, as it is composed of three main laminae: A, A1, C (see Fig. 5.2 for schematic of cat LGN). The layers of the cat LGN

are organized predominantly by ocular input, as laminae A and C are innervated by the contralateral retina, while laminae A1 is innervated by the ipsilateral retina (Stone, 1983; Sherman, 1985). There appear to be minimal differences between layers A and A1, which are composed of relay X and Y cells (Wilson et al., 1976; Hickey et al., 1977; Wilson et al., 1984; Montero, 1991). One select difference between the organization of the LGN in primates and cats is that the X and Y pathways mix within the A and A1 LGN layers in contrast to how the M and P pathways terminate in distinct layers. The W pathway terminates in the bottom part of the C layer (layers C1 and C2), while the upper part of the C layer receives Y cell input, in contrast to primate K cells that terminate in distinct layers. Given the configuration of the LGN in both the California sea lion and elephant seal, in that there are three distinct layers in each species, it is likely that the connections of the primary visual pathway in pinnipeds more closely resemble those described in cats.

Future directions

A future area of the cell and neuron counts component of this research will interpret how the number of cells and neurons in primate neocortex changes across development. This study, in the prosimian galago, additionally will determine how the architecture of primate neocortex changes across early development and compares to adult cortical architecture. Wong and Kaas (2010) reported on the architectonic features of the adult galago brain, and in our preliminary results we compare how juvenile neocortex and subcortical structures differ across development in areas related to the visual system. In primary visual cortex, for example, there are significant

changes in the immunoreactivity for parvalbumin, VGluT2, and NeuN. For example, in VGluT2 preparations at P0, there is minimal reactivity for VGluT2 in area 17 (Fig. 5.2). Layer 4 is

Figure 5.2 **Distribution of VGluT2 protein throughout galago development**. The distribution of VGluT2 is shown at P0, P7, and in a mature galago. Laminar boundaries are marked. Scale bar = 100 um.

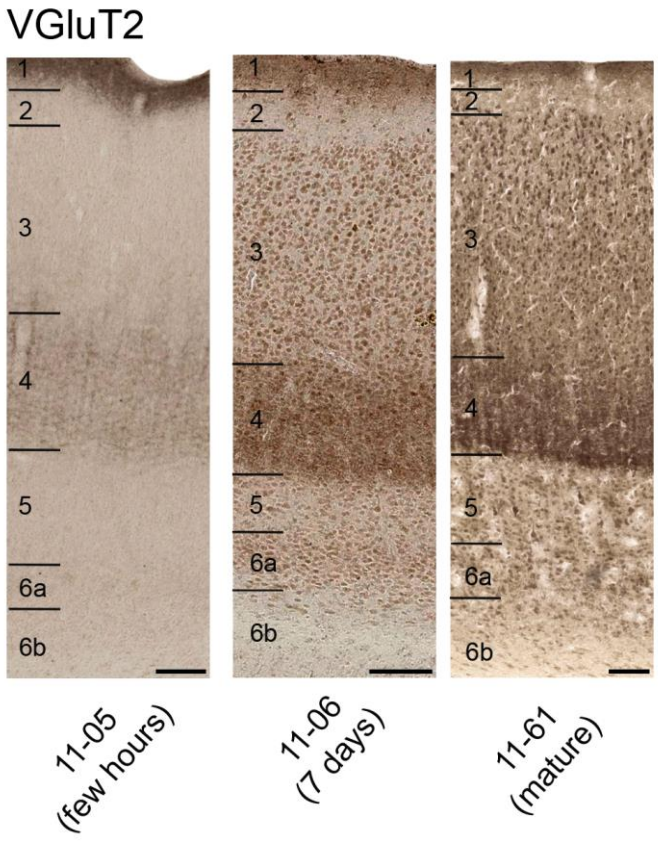

weakly stained for VGluT2, but there are no distinct cell bodies. Layer 4 is subdivided into three distinct compartments, in which the dorsal and ventral layers are more densely stained for VGluT2 terminations, and the middle layer is less densely stained. At P7, there is a denser distribution of VGluT2 immunoreactive cells in layers 3 – 6. Layer 4 is more densely stained for

VGluT2 at P7 compared to P0, but there is still a middle subdivision of layer 4 which remains weakly stained for VGluT2. Layer 6 at P7 is moderately stained for VGluT2 terminations. In mature galagos, the distribution of VGluT2 is similar to that at P7, in which layer 4 is densely stained for VGluT2. It has been suggested that the development of cortex occurs in a hierarchical order (O'Leary, 1989; Donoghue and Rakic, 1999; Sur and Leamey, 2001), and as such we do find supporting evidence that primary sensory areas, such visual, somatosensory, and auditory cortex, are some of the earliest areas to show signs of maturity. However, similar to the findings in marmosets (Bourne and Rosa, 2006), we also find evidence for the early maturation of the middle temporal area (MT) in galagos, which supports the idea of area MT as a primary visual area. These preliminary results thus suggest that there is significant reorganization of the galago cortex throughout development, and differences in brain organization between juvenile and mature primates. This emphasizes the need for not only more specimen in cell counts research to account for individual differences, but increased breadth in age in these samples. The architectonic component of this research will supplement the cell and neuron counts gained using the isotropic fractionator technique.

To make direction comparisons between the visual systems of primates and carnivores, future comparative research concerning the distribution of three calcium-binding proteins (CBPs), parvalbumin, calbindin, and calretinin, is anticipated in pinniped brains. There is only minimal research examining the distribution of CBPs in any pinniped brain (Hof et al., 1999), and now that certain components of the visual system in pinnipeds have been described, we can begin to categorize the distribution of neurochemical markers in neocortex. There is a continued interest in studying these neurochemical markers because each CBP appears to identify distinct cortical areas that probably have different functions. Across the mammalian taxa, we speculate

that there are as few as 20 or 30 areas in some living species, to well over 200 in humans, suggesting that throughout mammalian evolution there has been a focus on modification and addition of cortical areas (Kaas, 2012), and CBPs can help define these modules. The cortical distributions of both CBP cell bodies and fibers are important, since the fiber system in primates is likely to have both intrinsic cortical origins and extrinsic projections from subcortical regions. Figure 5.3 shows preliminary results from northern elephant seal tissue stained for parvalbumin. Here, V1 is clearly distinct from the other parts of cortex. Quantification and laminar analysis of parvalbumin-immunoreactive cell bodies and fibers, in addition to calbindin and calretinin, in various pinniped species will contribute to other available data concerning the distribution of CBPs amongst different mammals (Hof et al., 1999).

Figure 5.3 **Parvalbumin in the northern elephant seal.** The distribution of a calcium-binding protein, parvalbumin, in the northern elephant seal. Red line indicates the boundaries of primary visual cortex. EnS = entolateral sulcus; LS = lateral sulcus; SS = suprasylvian sulcus.

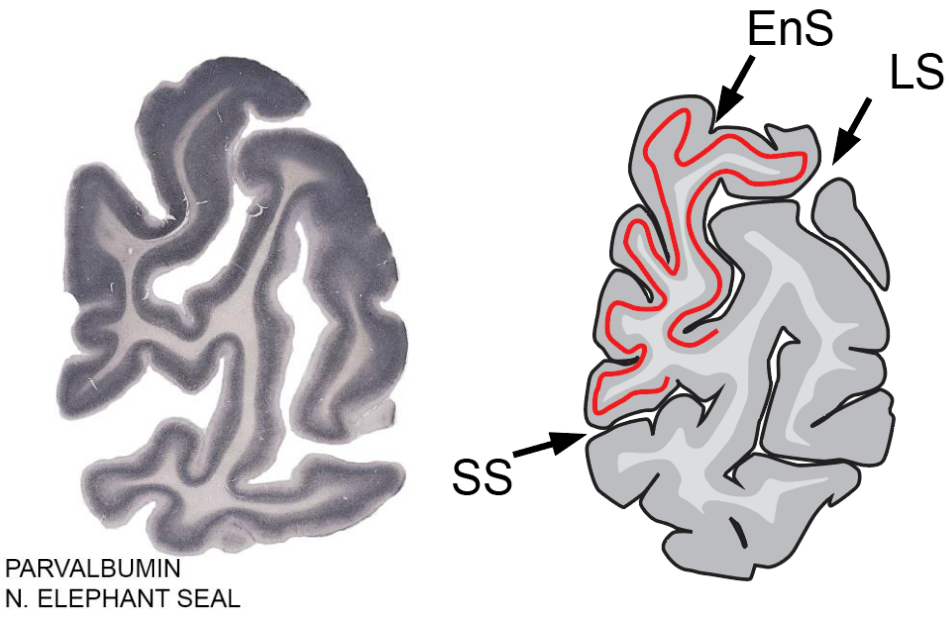

REFERENCES

Azevedo FA, Carvalho LR, Grinberg LT, Farfel JM, Ferretti RE, Leite RE, Jacob Filho W, Lent R, Herculano-Houzel S (2009) Equal numbers of neuronal and nonneuronal cells make the human brain an isometrically scaled-up primate brain. J Comp Neurol 513:532-541.

Bahney J, von Bartheld CS (2014) Validation of the isotropic fractionator: comparison with unbiased stereology and DNA extraction for quantification of glial cells. J Neurosci Methods 222:165-174.

Bourne JA, Rosa MG (2006) Hierarchical development of the primate visual cortex, as revealed by neurofilament immunoreactivity: early maturation of the middle temporal area (MT). Cereb Cortex 16:405-414.

Carlo CN, Stevens CF (2013) Structural uniformity of neocortex, revisited. Proc Natl Acad Sci U S A 110:1488-1493.

Collins CE (2011) Variability in neuron densities across the cortical sheet in primates. Brain Behav Evol 78:37-50.

Collins CE, Airey DC, Young NA, Leitch DB, Kaas JH (2010) Neuron densities vary across and within cortical areas in primates. Proc Natl Acad Sci U S A 107:15927-15932.

Donoghue MJ, Rakic P (1999) Molecular gradients and compartments in the embryonic primate cerebral cortex. Cereb Cortex 9:586-600.

Fonseca-Azevedo K, Herculano-Houzel S (2012) Metabolic constraint imposes tradeoff between body size and number of brain neurons in human evolution. Proc Natl Acad Sci U S A 109:18571-18576.

Herculano-Houzel S (2012) The remarkable, yet not extraordinary, human brain as a scaled-up primate brain and its associated cost. Proc Natl Acad Sci U S A 109 Suppl 1:10661-10668.

Herculano-Houzel S, Collins CE, Wong P, Kaas JH, Lent R (2008) The basic nonuniformity of the cerebral cortex. Proc Natl Acad Sci U S A 105:12593-12598.

Herculano-Houzel S, Kaas JH (2011) Gorilla and orangutan brains conform to the primate cellular scaling rules: implications for human evolution. Brain Behav Evol 77:33-44.

Herculano-Houzel S, Manger PR, Kaas JH (2014) Brain scaling in mammalian evolution as a consequence of concerted and mosaic changes in numbers of neurons and average neuronal cell size. Front Neuroanat 8:77.

Hickey TL, Spear PD, Kratz KE (1977) Quantitative studies of cell size in the cat's dorsal lateral geniculate nucleus following visual deprivation. J Comp Neurol 172:265-281.

Hof PR, Glezer, II, Conde F, Flagg RA, Rubin MB, Nimchinsky EA, Vogt Weisenhorn DM (1999) Cellular distribution of the calcium-binding proteins parvalbumin, calbindin, and calretinin in the neocortex of mammals: phylogenetic and developmental patterns. J Chem Neuroanat 16:77-116.

Jeffries AM, Killian NJ, Pezaris JS (2014) Mapping the primate lateral geniculate nucleus: a review of experiments and methods. J Physiol Paris 108:3-10.

Kaas JH (2012) Evolution of columns, modules, and domains in the neocortex of primates. Proc Natl Acad Sci U S A 109 Suppl 1:10655-10660.

Miller DJ, Balaram P, Young NA, Kaas JH (2014) Three counting methods agree on cell and neuron number in chimpanzee primary visual cortex. Front Neuroanat 8:36.

Montero V (1991) A quantitative study of synaptic contacts on interneurons and relay cells of the cat lateral geniculate nucleus. Exp Brain Res 86.

Mota B, Herculano-Houzel S (2015) BRAIN STRUCTURE. Cortical folding scales universally with surface area and thickness, not number of neurons. Science 349:74-77.

O'Leary DD (1989) Do cortical areas emerge from a protocortex? Trends Neurosci 12:400-406.

Olkowicz S, Kocourek M, Lucan RK, Portes M, Fitch WT, Herculano-Houzel S, Nemec P (2016) Birds have primate-like numbers of neurons in the forebrain. Proc Natl Acad Sci U S A 113:7255-7260.

Prior H, Schwarz A, Gunturkun O (2008) Mirror-induced behavior in the magpie (Pica pica): evidence of self-recognition. PLoS Biol 6:e202.

Raby CR, Alexis DM, Dickinson A, Clayton NS (2007) Planning for the future by western scrub-jays. Nature 445:919-921.

Rockel AJ, Hiorns RW, Powell TP (1980) The basic uniformity in structure of the neocortex. Brain 103:221-244.

Sawyer EK, Turner EC, Kaas JH (2016) Somatosensory brainstem, thalamus, and cortex of the California sea lion (Zalophus californianus). J Comp Neurol 524:1957-1975.

Sherman S (1985) Functional organization of the W-cell, X-cell, and Y-cell pathways in the cat - a review and hypothesis. Prog Psychobiol Physiol Psych 11:233-314.

Sherman SM, Guillery RW (2002) The role of the thalamus in the flow of information to the cortex. Philos Trans R Soc Lond B Biol Sci 357:1695-1708.

Stone J (1983) Parallel processing in the visual system : the classification of retinal ganglion cells and its impact on the neurobiology of vision. New York: Plenum Press.

Sur M, Leamey CA (2001) Development and plasticity of cortical areas and networks. Nat Rev Neurosci 2:251-262.

Weir AA, Chappell J, Kacelnik A (2002) Shaping of hooks in New Caledonian crows. Science 297:981.

Weller RE, Kaas JH (1989) Parameters affecting the loss of ganglion cells of the retina following ablations of striate cortex in primates. Vis Neurosci 3:327-349.

Wilson JR, Friedlander MJ, Sherman SM (1984) Fine structural morphology of identified X- and Y-cells in the cat's lateral geniculate nucleus. Proc R Soc Lond B Biol Sci 221:411-436.

Wilson PD, Rowe MH, Stone J (1976) Properties of relay cells in cat's lateral geniculate nucleus: a comparison of W-cells with X- and Y-cells. J Neurophysiol 39:1193-1209.

Wong P, Kaas JH (2010) Architectonic subdivisions of neocortex in the Galago (Otolemur garnetti). Anat Rec (Hoboken) 293:1033-1069.

Young NA, Collins CE, Kaas JH (2013a) Cell and neuron densities in the primary motor cortex of primates. Front Neural Circuits 7:30.

Young NA, Szabo CA, Phelix CF, Flaherty DK, Balaram P, Foust-Yeoman KB, Collins CE, Kaas JH (2013b) Epileptic baboons have lower numbers of neurons in specific areas of cortex. Proc Natl Acad Sci U S A 110:19107-19112.

APPENDIX

Patchy distributions of myelin and vesicular glutamate transporter 2 align with cytochrome oxidase blobs and interblobs in the superficial layers of primary visual cortex

The following appendix chapter was published under the same title in the journal Eye and Brain by Emily Rockoff, Pooja Balaram, and Jon Kaas; September 2014.

Abstract

Blobs are a modular component of the primary visual cortex (area 17) of all primates, but not of other mammals closely related to primates. They are characterized as an even distribution of patches, puffs, or blobs of dense cytochrome oxidase (CO) expression in layer 3 of area 17, and are now known to differ from surrounding, non-blob cortex in thalamic, intrinsic, and extrastriate connections. Previous studies have also recognized a blob-like pattern of myelin-dense patches in layer 3 of area 17 of primates, and more recently the vesicular glutamate transporter (VGluT)-2 isoform of the VGluT family has been found to selectively distribute to layer 3 patches in a similar blob-like pattern. Here, we sought to determine if the blob-like patterns all identify the same modular structures in area 17 of primates by staining alternate brain sections cut parallel to the surface of area 17 of a prosimian primate (*Otolemur garnettii*) for CO, myelin, and VGluT2. By aligning the sections from the three preparations, we provide clear evidence that the three preparations all identify the same modular blob structures. The results

provide a further understanding of the functional nature of the blobs by demonstrating that their higher level of CO activity is related to thalamic inputs from the lateral geniculate nucleus that use VGluT2 as their main glutamate transporter, and via myelinated axons.

Introduction

The neocortex of mammals is structurally and functionally divided into areas and repeating modules or columns within areas (Kaas, 2012). Carroll and Wong-Riley (1984) were the first to recognize that the primary visual cortex (V1) of monkeys is subdivided into two types of modules by differences in the distribution of the cellular metabolic enzyme, cytochrome oxidase (CO) (Wong-Riley, 1994). Layer 3 of V1 is characterized by a pattern of small patches of dense CO expression that are regularly dispersed in a field of less dense CO expression. These patterns were originally called "puffs" (Wong-Riley, 1989; Wong-Riley, 1994), but the improbable name of "blobs", used by subsequent researchers (Livingstone and Hubel, 1984), came into common use. Blobs are found in V1 of all primates (Horton and Hubel, 1981; Preuss et al., 1993; Preuss and Kaas, 1996), but not in close relatives of primates, such as tree shrews and rodents. Therefore, the blob modules in V1 likely evolved with the first primates (Kaas, 2012). Evidence also suggests that certain carnivores, such as cats, have blobs, but they likely have a different structure that evolved independently of the primate lineage (Murphy et al., 1995). Consistent with the high level of the metabolic enzyme CO, neurons in blobs have higher firing rates than neurons outside blobs, and neurons in blob modules are more selective for color and less selective for stimulus orientation than neurons in interblob regions (Livingstone and Hubel, 1984; Hendrickson, 1985; Felleman, 2008; Lu and Roe, 2008; Economides et al., 2011).

Blobs and interblobs are also distinguished by differences in intrinsic V1 connections, and extrinsic connections with other visual thalamic and cortical areas (Livingstone and Hubel, 1984; Casagrande, 1994a). For example, the blobs, unlike layer 4, selectively receive inputs from the koniocellular layers of the lateral geniculate nucleus (Lachica and Casagrande, 1992; Casagrande et al., 2007). Therefore, CO blobs appear to identify an important component of the primate visual system, and other histological ways of recognizing them would be useful. If other histological markers with similar distribution patterns are found to colocalize with CO blobs, it will be possible to discuss and identify further differences in blob and interblob function.

In this regard, two other histological markers have revealed blob-like patterns in primate V1. Myelin stains reveal a blob-like pattern of myelin-dense patches in V1 of monkeys (Tootell et al., 1983), and a similar pattern of myelin-sparse holes in a myelin-dense background (Krubitzer and Kaas, 1989; Wong and Kaas, 2010). These two different patterns seem to relate to different sublayers of layer 3, so that both the myelin patches and holes may reflect columns containing blobs. More recently, the vesicular glutamate transporter (VGluT)-2 isoform of the vesicular glutamate-transporter family has been found to identify a blob-like pattern in V1 of galagos (Wong and Kaas, 2010) and Old World macaque monkeys (Bryant et al., 2012; Balaram et al., 2013; Garcia-Marin et al., 2013). The distribution patterns of the myelin-dark patches, the myelin-light holes, and the VGluT2-dense patches all suggest that they reveal different features of the same modular division of V1, the modules that densely express CO.

To address this possibility, we processed alternate sections from the cerebral cortex of prosimian galagos for CO, myelin, or VGluT2. Galagos are specifically relevant to a study of blobs, as they have well-developed koniocellular layers of the lateral geniculate nucleus that are known to project to the blobs (Lachica and Casagrande, 1992), and yet they lack blue (S) cones

(Wikler and Rakic, 1990; Jacobs et al., 1996). Brain sections were cut parallel to the surface of V1, and CO-, myelin-, and VGluT2-stained sections were aligned and compared through the depth of V1. The alignment of CO blobs with myelin-dense patches and VGluT2 puffs indicates that all these markers identify the same cortical column.

Materials and Methods

The alignment of CO, myelin, and VGluT2 distributions was studied in four adult galagos (*Otolemur garnettii*). Experimental procedures were all approved by the Vanderbilt Institutional Animal Care and Use Committee and followed the guidelines published by the US National Institutes of Health.

Tissue acquisition and histology

Each animal was given a lethal overdose of sodium pentobarbital (80 mg/kg) and perfused transcardially with phosphate-buffered saline, followed by 4% paraformaldehyde in 0.1M PB, and then 4% paraformaldehyde and 10% sucrose in phosphate-buffered saline. The brain was removed from the skull, bisected, post-fixed for 2 – 4 hours in 4% paraformaldehyde and 10% sucrose in PB, and cryoprotected in 30% sucrose. The subcortical structures were removed from the cortices, and one cortical hemisphere in each animal was manually flattened via the opening of sulci. Only one hemisphere from each case was used, due to other laboratory experiments requiring tissue (left, n = 2, right, n = 2). The flattened cortices were then cut tangentially on a freezing microtome at 40 µm and saved in three series.

Histochemistry

One series of sections from each case was processed for myelin using the Gallyas (1979) silver procedure, which is based on the binding of colloidal silver to myelin for viewing by light microscopy. A second series of sections was processed for cytochrome oxidase (Wong-Riley, 1979) to identify the original CO blobs. Stained sections were then mounted and dehydrated in an ascending series of ethanols (70% for 20 minutes, 95% for 10 minutes, 100% for 10 minutes), cleared in xylene, and cover-slipped using Permount™ (Thermo Fisher Scientific, Waltham, MA, USA).

Immunohistochemistry

One series from each case was immunohistochemically labeled for VGluT2 protein using commercial antibodies against VGluT2 and previously described immunohistochemical techniques (Balaram et al., 2011). In brief, sections were incubated in a primary antibody solution of 1:5000 goat mouse anti-VGluT2 (EMD Millipore, Billerica, MA, USA), incubated in 1:500 peroxidase anti-goat immunoglobulin G in blocking solution (Vector Laboratories, Burlingame, CA, USA), amplified using an avidin–biotin conjugate kit (Vector Labs), and visualized using a diaminobenzidine reaction with nickel enhancement. The primary antibody against VGluT2 has been previously characterized in galago tissue (Wong and Kaas, 2010; Balaram et al., 2011; Baldwin et al., 2012). Sections were then dehydrated, cleared in xylene, and cover-slipped using the methods described in the previous paragraph.

Light microscopy

Processed sections were viewed using a Nikon (Tokyo, Japan) E800 microscope, and digital photomicrographs of visual area structures were captured using a Nikon DXM2200

camera. The images were adjusted for contrast and brightness using Adobe Photoshop (Adobe Systems, San Jose, CA. USA), but they were not otherwise altered. Cortical borders were apparent even at low magnification in CO, myelin, and VGluT2 stains, making the location of the V1/V2 border easily visible when viewed under a high-powered light microscope.

Stain comparisons by case

As previously mentioned, one hemisphere per galago was analyzed. CO-, myelin-, and VGluT2-staining patterns were all visible throughout V1, but it was difficult to identify large regions of V1 where all three stains were distinct and measurable. Additionally, only a few sections in each case would contain blobs, given the thickness of layer 3 in V1. Due to these complexities of tissue reconstruction, tissue was typically only processed for two of the three stains (except for case 4). Therefore, comparisons in each case are only between two types of preparation. In case 1, CO and myelin blobs were analyzed (n = 74). In case 2, CO and VGluT2 blobs were analyzed (n = 21). In case 3, VGluT2 and myelin blobs were analyzed (n = 100). Case 4 consisted of all three stains, and both the CO and VGluT2 blobs (n = 29) and CO and myelin blobs (n = 40) were analyzed. However, the myelin and VGluT2 comparison was excluded from case 4, since there was a lack of tissue visible in which both these blobs appeared and could be measured reliably.

Identification and anatomical reconstruction of cytochrome oxidase blobs

Images were cropped in Adobe Photoshop at the V1/V2 border, which was identifiable by the abrupt change in reactivity for each stain. The V1/V2 border was visible in all CO-, myelin-, and VGluT2-stained sections (Fig. 6.1). Multiple cortical layers were often visible in the same section due to the curvature of the cortex; therefore, transitions between layers are

visible in some sections (Fig. 6.1). It is not currently possible to find the exact areas of blobs in primate visual cortex, as their boundaries are expressed as a gradual change in CO reactivity (Fig. 6.2A). Therefore, the borders of blobs and interblobs were estimated by visual inspection after adjusting for contrast in Photoshop. Conservative estimates of blob boundaries were generated by preliminarily outlining regions of dense CO, myelin, or VGluT2 staining using the paint tool in Photoshop (Fig. 6.2B), and the inner border of this outline was redrawn for final area measurements in ImageJ (National Institutes of Health, Bethesda, MD, USA) (Fig. 6.2C).

Fig. 6.1 **Patchy staining pattern of area 17.** Cytochrome oxidase (CO)-rich regions, or CO blobs, are observed in area 17 of the galago neocortex. **(A)** CO-, **(B)** myelin-, and **(C)** vesicular glutamate transporter (VGluT)-2 stained section cut parallel to the surface of a manually flattened cerebral hemisphere. Dashed lines show the approximate location of the cortical border between primary visual cortex (V1) and secondary visual cortex (V2). The star marks the transition from layer 3 to layer 4, with the blobs residing in the former. Scale bar = 1 mm.

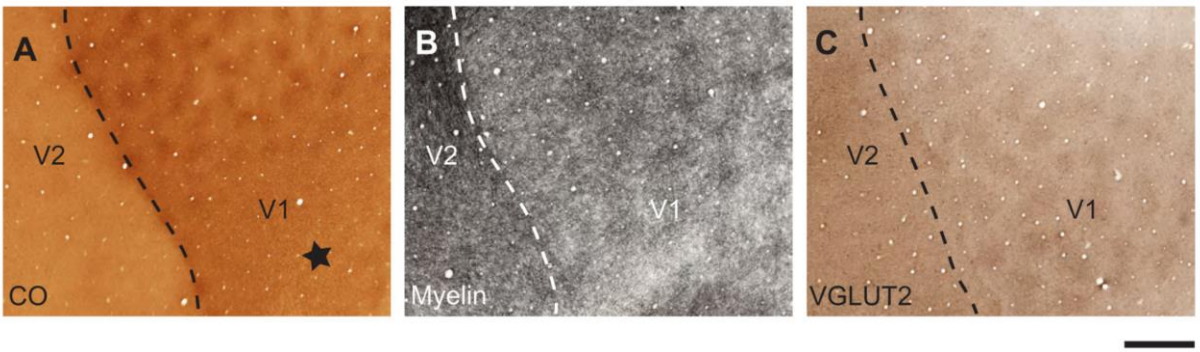

Fig. 6.2 **Identification of cytochrome oxidase (CO) blobs. (A-C)** are of the same CO section to demonstrate the outline technique. **(A)** Arrowheads indicate the outlines of one individual blob. CO blobs are observed in area 17 of the galago neocortex. **(B)** Blue outlines indicate the first outline drawn around individual blobs in Photoshop, while red lines indicate the conservative inner boundary drawn second in Photoshop. **(C)** The red outlines were used in all statistical analyses. Scale bar = 1 mm.

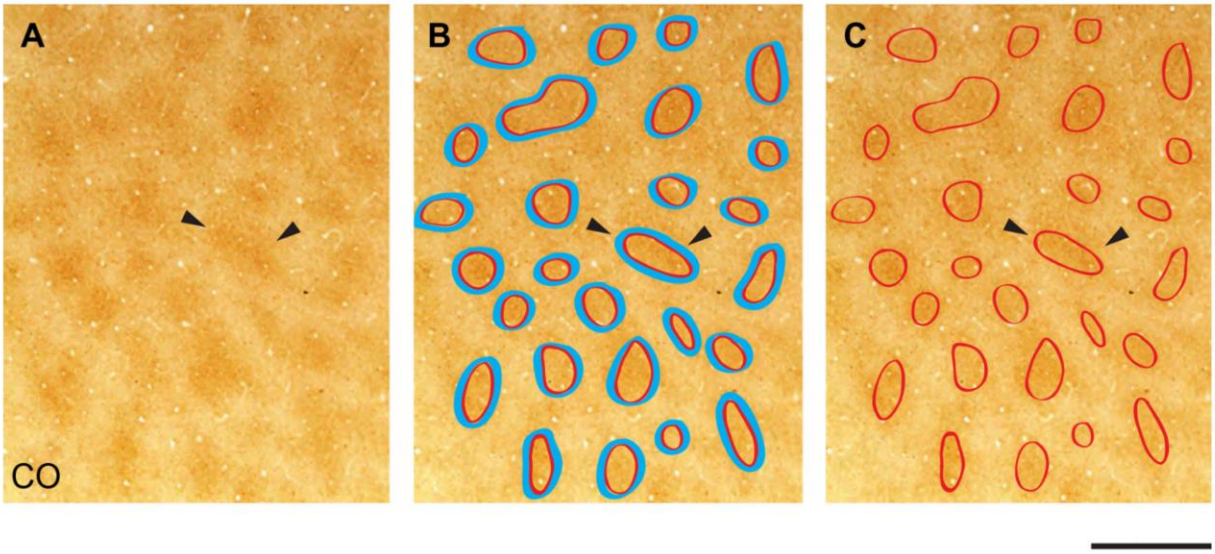

Since the depth of layer 3 spread throughout consecutive sections, there were often a few CO, myelin, or VGluT2 blobs outlined, which represented the same blob once sections were aligned. When layer 3 was reconstructed (see Fig. 6.3) and it was apparent that two outlined blobs of the same stain were a representation of the same blob, an average of these outlines was drawn (see Fig. 6.4). For example, if all the CO blobs are outlined in layer 3, and layer 3 is visible in two separate sections, the alignment of both layer 3 CO sections will reveal multiple outlined CO blobs on top of one another, necessitating an average outline of that CO blob. It has been reported that blob borders can be estimated by using the filtering software from ImageJ and

Photoshop, but a comparison of these two methods does not favor one technique over the other, which provides further evidence that this is an accurate and trustworthy method (Baldwin et al., 2012). Accordingly, all data were collected with the manual method using subjective estimates of blob borders.

Fig. 6.3 **Alignment of adjacent CO, VGluT2, and myelin sections.** Blue lines in **(A)** indicate outlines of CO blobs. Red lines in **(B)** indicate outlines of VGluT2 patches. Yellow lines in **(C)** indicate outlines of myelin blobs. Arrowheads indicate blood vessels used for alignment, and dashed lines demonstrate how sections were layered on top of one another (with blob outlines hidden during actual alignment). **(D)** Relationship between CO, VGluT2, and myelin blobs are section alignment. Scale bar = 1 mm.

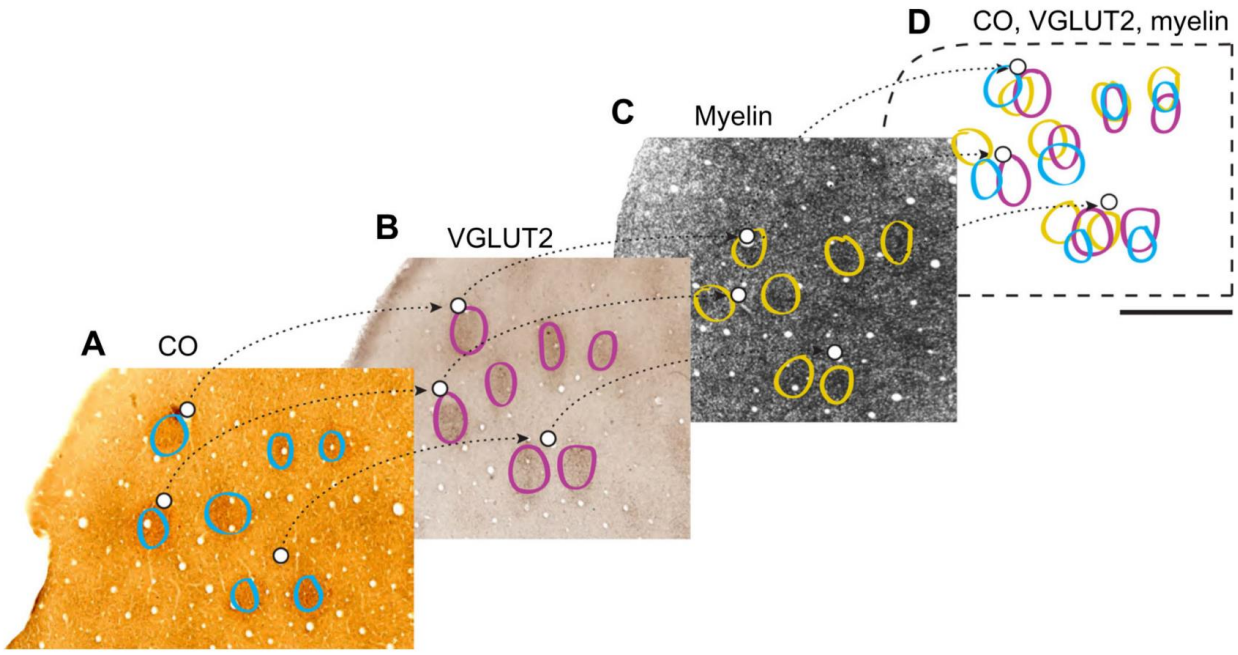

Fig. 6.4 **Randomization of blobs versus measured overlap percentages.** Dashed lines indicate tissue that does not contain both types of blobs, and is therefore excluded from analysis. Black arrowheads indicate an example of cytochrome oxidase (CO)/myelin blobs with near 100% overlap scores. Blue arrowheads indicate an example of CO/myelin blobs with near 0% overlap scores. Red arrowheads indicate an example of CO/myelin blobs in which multiple blobs in one stain appear to correlate with a single blob in the other stain, necessitating an average drawing of those two blobs. **(A)** Aligned overlap of CO (blue) and myelin (red) from part of V1 in case 1. **(B)** Random assortment of overlapping blobs, which is achieved from rotating the myelin section by 180°.

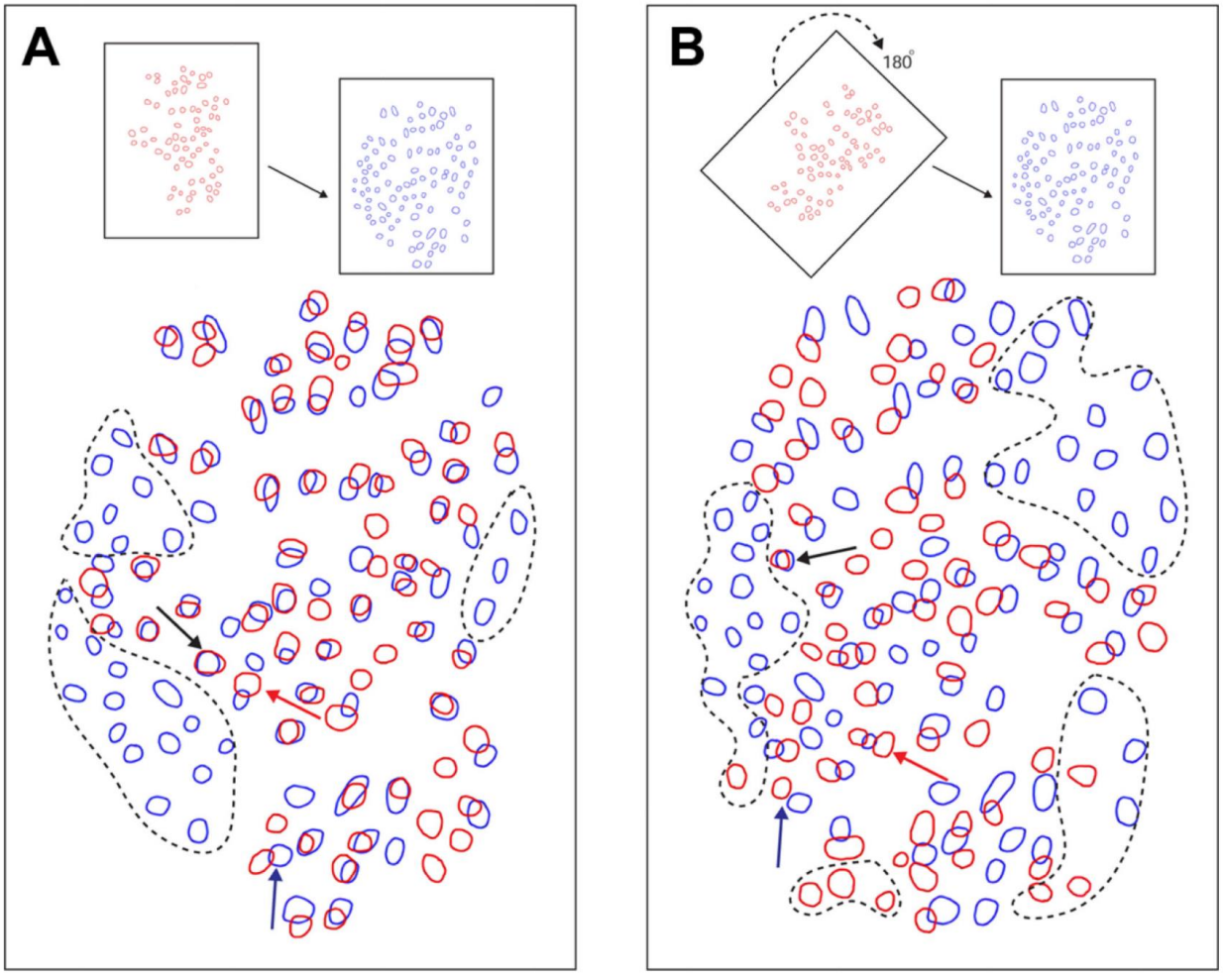

It is important to address the bias associated with using a manual measure to identify blobs in the cortex. While previous studies have reported that this method can be just as accurate as computerized methods that examine density changes across images of stained sections, there is the concern that outlining could be biased toward what we expect to find. However, this assumption is highly unlikely, given that blob outlines were individually marked on separate sections, and were not visible when adjacent tissue sections were aligned. After tissue sections were aligned, blob outlines were made visible again for area measurement. Therefore, our methods were accurate in identifying an unbiased, constant, and conservative estimate of each individual blob in V1.

Adjacent tangential V1 sections in each series were aligned in Photoshop, using at least three blood vessels to reconstruct superficial layer 3. Layer 3 in each series was aligned using blood vessels in each section (Fig. 6.3). Differential tissue shrinkage and expansion within each section, from variations in histological and immunohistochemical techniques, required V1 then to be divided into groups in Photoshop for local tissue alignment. The size of these groups differed, based on identifiable surrounding blood vessels and the degree of tissue distortion. Each case typically had four to nine groups containing anywhere from five to 28 blobs per group.

Data acquisition

The degree of overlap when two blob regions were aligned was computed using the measurement tool in ImageJ, with relative areas and percentage of overlap rather than exact areas. For all blob alignments, the individual areas of both blobs were computed, and then the area of overlap was measured to determine the percentage overlap between the blobs (Fig. 6.4A). Note that the percentage overlap of blob 1 in blob 2 can be computed, or conversely the

percentage overlap of blob 2 in blob 1 can be computed, which will yield a slightly different percentage-overlap number. It is more relevant to compute how much myelin or VGluT2 overlaps with CO blobs, and for comparisons between myelin and VGluT2, the percentage overlap of VGluT2 in myelin was computed. The converse distributions of percentage-overlap scores and confidence intervals are reported for all three types of comparisons (i.e., CO/VGluT2, CO/myelin, and myelin/VGluT2) (Fig. 6.5), but they were not significantly different from their counterparts. The comparisons between VGluT2 and CO had more variable spreads (Fig. 6.5B), but this was likely due to the low sample number of blobs for this comparison (total n = 50, from case 2 and case 4), and will not be discussed further. In case 1, the percentage overlap for myelin blobs in CO blobs was computed. In case 2, the percentage overlap for VGluT2 blobs in CO blobs was computed. In case 3, the percentage overlap for VGluT2 blobs in myelin was computed. In case 4, since all three types of stain were present, the percentage overlaps for myelin in CO as well as VGluT2 in CO were computed.

Analysis

To analyze overlapping blob distributions between blobs of two different stains, the total overlap percentages for each type of comparison (i.e., VGluT2/CO, myelin/CO, and VGluT2/myelin) were compared against a random alignment of blobs. The myelin sections from case 1 were rotated 180° to create a random pattern of aligned blobs at chance levels (n = 65) (Fig. 6.4B). The control percentage-overlap score was calculated between the randomly aligned myelin and CO blobs. A box plot shows the distribution of percentage overlap scores in the random case, as well as the percentage-overlap scores in the myelin/CO comparisons (case 1 and case 4), VGluT2/CO comparisons (case 2 and case 4), and the VGluT2/myelin comparisons (case 3) (Fig. 6.6).

Fig. 6.5 **Box plot comparing the percent-overlap comparisons and converse computations (A)** Distribution of percentage-overlap scores for myelin blobs in cytochrome oxidase (CO) blobs in light green (0.444 – 0.570), and distribution of percentage-overlap scores for CO blobs in myelin blobs in dark green (0.445 – 0.570). **(B)** Distribution of percentage-overlap scores for vesicular glutamate transporter (VGluT)-2 blobs in CO blobs in light red (0.455 – 0.600), and distribution of percentage-overlap scores for CO blobs in VGluT2 blobs in dark red (0.554 – 0.762). **(C)** Distribution of percentage-overlap scores for VGluT2 blobs in myelin blobs in light blue (0.455 – 0.566), and distribution of percentage overlap scores for myelin blobs in VGluT2 blobs in dark blue (0.457 – 0.566). The myelin and CO comparisons combine case 1 and case 4 (n = 114), the VGluT2 and CO comparisons combine case 2 and case 4 (n = 50), and the VGluT2 and myelin comparisons are for case 3 (n = 100).

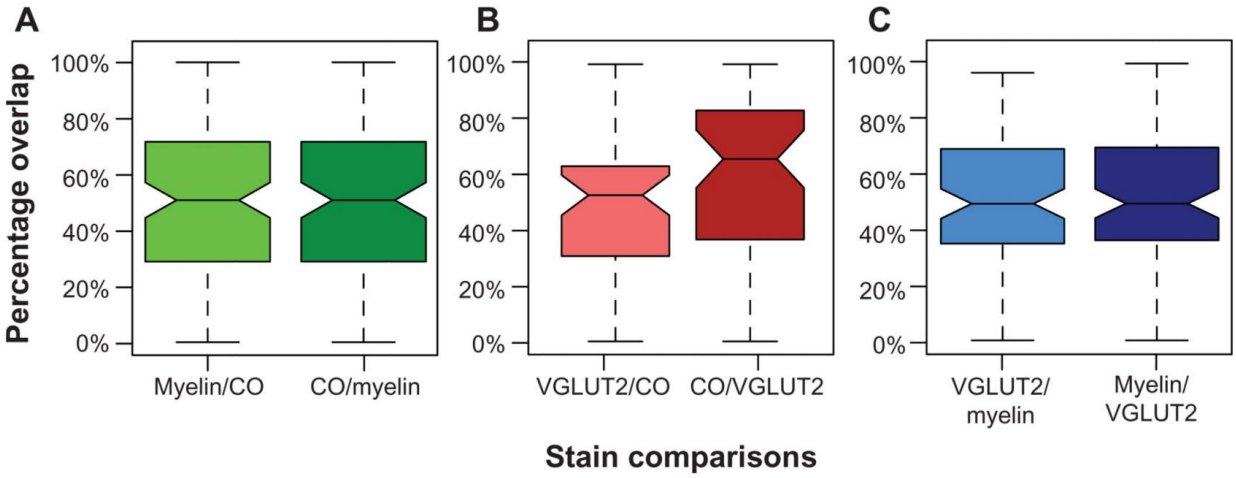

Fig. 6.6 **Box plot comparing random overlap score versus stain comparisons.** The bars indicate the spread of overlap scores, while the notches indicate the 95% confidence interval. The distributions of percentage-overlap scores of myelin blobs in cytochrome oxidase (CO blobs; green [0.444 – 0.570]), vesicular glutamate transporter (VGluT)-2 blobs in CO blobs (red [0.455 – 0.600]), and VGluT2 blobs in myelin blobs (blue [0.455 – 0.566]) are expressed. The experimental groups have a spread ranging from 0% to 100%, while the random group has a spread ranging from 0% to 57% with an outlier at 100%. The non-overlapping 95% confidence intervals indicate that there was significant difference between the random group and the three experimental groups. The myelin/CO comparisons combine case 1 and case 4 (n = 114), the VGluT2/CO comparisons combine case 2 and case 4 (n = 50), and the VGluT2/myelin comparisons are for case 3 (n = 100).

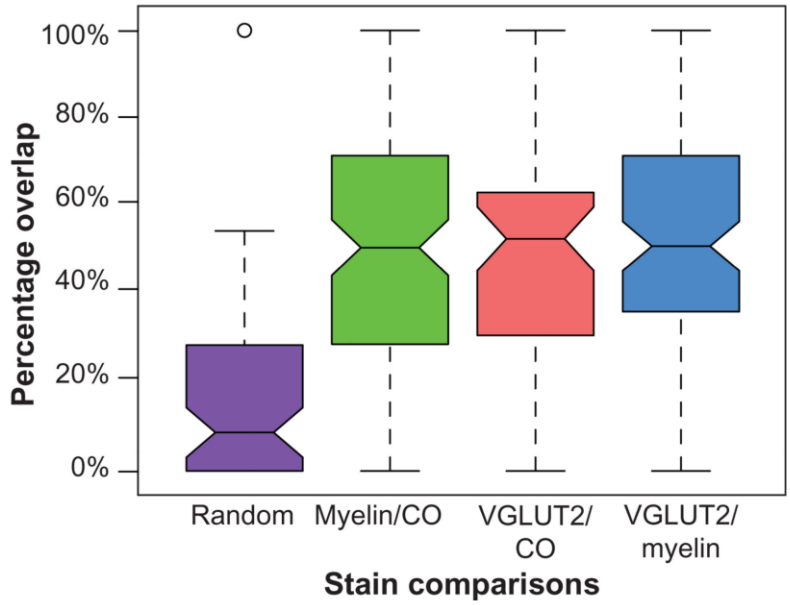

Results

The goal of this study was to determine whether the myelin-rich and VGluT2-rich blobs aligned with CO blobs in the primary visual cortex, since visual inspection of VGluT2 or myelin

blobs in comparison to CO blobs indicated that all patches likely identified the same blobs, or varying profiles of the same blob structures. The present results provide evidence that darkly stained patches of myelin and VGluT2 correspond with CO blobs in the superficial layers of V1.

Patterns of CO, myelin, and VGluT2 staining in V1

CO, myelin, and VGluT2 patterns were all visually similar in flattened tissue preparations of galago visual cortex (Fig. 6.1). CO blobs in layer 3 appeared as dark, oval patches spread in a regular pattern across V1. In VGluT2 preparations of V1, VGluT2-rich blobs were surrounded by VGluT2-poor regions throughout layer 3. Myelin-stained sections revealed a similarly patchy pattern, with dark myelinated blobs surrounded by a lighter, myelin-poor background. Identification of blobs in CO and VGluT2 sections was easier than in myelin sections, as the myelin blobs appeared to transition more gradually into interblob tissue. Despite that difference, myelin-dense blobs were still detectable in each case. Generally, blobs in all three stains appeared more circular in central areas of V1 tissue, while those located in more peripheral regions took on an elongated, noncircular appearance. Additionally, all blobs were generally evenly spaced and seemed to align in rows, consistent with prior descriptions of CO-staining patterns in V1 (Wong-Riley, 1989). Coronal sections of V1 (Fig. 6.7) stained for CO, myelin, or VGluT2 also show evenly distributed patches of dense and light labels throughout layer 3.

Fig. 6.7 **Laminar characteristics of area 17 at low magnification.** Coronal sections from the occipital cortex were processed for **(A)** cytochrome oxidase (CO), **(B)** myelin, and **(C)** vesicular glutamate transporter (VGluT)-2. The arrowheads in **(A–C)** indicate the locations of CO blobs in layer 3. Scale bar = 1 mm.

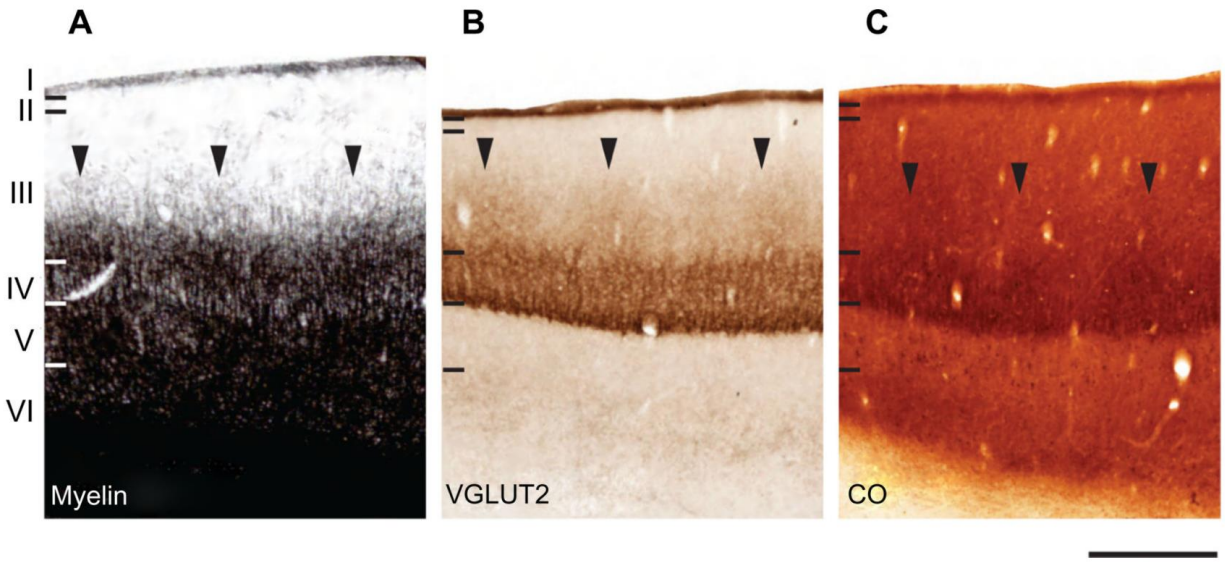

In layer 4, all three stains showed dense, homogeneous staining, which made layer 3 easily distinguishable by irregular staining immediately dorsal to layer 4. This dense labeling pattern for CO, myelin, and VGluT2 was consistent with previous results in galagos (Wong and Kaas, 2010; Balaram et al., 2011), and likely reflects the dense thalamocortical projections that terminate in this layer (Glendenning et al., 1976; Casagrande and De Bruyn, 1982; Florence et al., 1983; Diamond et al., 1985; Florence and Casagrande, 1987; 1990; Lachica and Casagrande, 1992). Coronal sections through V1 (Fig. 6.7) delineated the boundaries of regular CO and VGluT2 staining in layer 4, and identified densely labeled patches in layer 3, as well as layers 5 and 6 in CO preparations (Livingstone and Hubel, 1982; Condo and Casagrande, 1990). Myelin-dense patches, however, appeared almost continuous from layer 3 through layer 5 of V1. For

data collection, we only used blob measurements in superficial layer 3, as it was not known whether visible blobs in deeper layers 5 and 6 corresponded to the same set of connections.

CO, myelin, and VGluT2 alignment

When aligned blob patterns were compared across adjacent sections, the number of blob-like structures in any local region of V1 was identical across CO, myelin, and VGluT2 preparations. The 95% confidence intervals for the medians of the myelin/CO (0.444 – 0.570) and VGluT2/CO (0.455 – 0.600) comparisons did not overlap with the control 95% confidence interval (0.033 – 0.014), signifying that both the myelin/CO and VGluT2/CO comparisons contained significantly higher percentage-overlap scores than the random alignment of blobs. This suggests that within layer 3, dark CO blobs were well aligned with dark VGluT2 patches, and that the CO-dense blobs and myelin-dense blobs identified the same cortical regions. Furthermore, the 95% confidence intervals for the VGluT2/myelin percentage-overlap scores (0.455 – 0.566) also yielded an equally significant result, which was expected, given how each of these two stains related to the CO blob distribution in V1. While the contrast between blobs and interblobs in the myelin sections was remarkably less prominent compared to CO and VGluT2 sections (see Fig. 6.1B), the blob regions outlined in individual myelin sections aligned well with those of the VGluT2- and CO-blob regions. Overall, all alignments consistently showed that CO blobs aligned with myelin-dense and VGluT2-rich patches, and that the CO interblobs likely overlapped with the myelin-pale and VGluT2-sparse regions as well. Lastly, coronal sections of CO, myelin, and VGluT2 revealed vertical laminar specificity and high overlap of CO blobs with myelin and VGluT2 patches in V1 (Fig. 6.7).

Discussion

The primary aim of this study was to characterize and align the patchy distributions of CO, myelin, and VGluT2 labeling across the striate cortex in galagos, to determine how these patterns might relate to the functional roles of V1. We found that myelin and VGluT2 had patchy distribution patterns throughout layer 3 of cortex V1 and homogeneous distribution patterns across layer 4, which were identical to CO-staining patterns in these layers. Further analysis of aligned sections indicated that the blob-like structures visualized in myelin and VGluT2 stains colocalized with CO-dense blobs in V1. When the blob-like structures were aligned across sections, the percentage overlap was high. However, there was variability in how well blobs overlapped, as some overlapped perfectly while others were adjacent with no overlap. The overlap percentages were not expected to be perfect, because each stain likely revealed different functional profiles of blobs. However, it is important to point out that these comparisons provide convincing evidence that each stain identified the same larger blob structure. Furthermore, laminar differences seen within myelin and VGluT2 preparations revealed a vertical columnar structure that included blobs, which is consistent with a modular organization of V1 in primates.

The differences in CO, myelin, and VGluT2 expression in blobs and interblobs reflected the anatomical and functional differences between those two regions of V1. Anatomical data suggested that there was a modular organization of geniculate projections in the galago visual cortex, and blobs and interblobs contributed to separate transformations of geniculate inputs within V1. Besides having different levels of metabolic activity, blobs and interblobs also differ in their efferent and afferent connections (Livingstone and Hubel, 1987; Casagrande, 1994a; 1994b) The major thalamic input to V1 in galagos and other primates arises from the dorsal LGN, and terminates in layers 1, 3, 4, and 6 (Kaas et al., 1978). The magnocellular (M)

geniculate cells predominantly project to layer 4α of V1 and parvocellular (P) cells to 4β, while koniocellular (K) cells terminate directly within CO blobs in layers 3 (Jones and Hendry, 1989; Lachica and Casagrande, 1992; Lachica et al., 1993; Hendry and Yoshioka, 1994; Johnson and Casagrande, 1995; Ding and Casagrande, 1997; Goodchild and Martin, 1998). K-cell inputs to layer 3 terminate in clusters that are surrounded by corticocortical projections and intrinsic laminar connections, including those from layer 4 (Carey et al., 1979; Casagrande and De Bruyn, 1982; Diamond et al., 1985; Lachica and Casagrande, 1992), thus strongly linking the CO blobs to the K-geniculate pathway in V1 (Casagrande et al., 2006). CO blobs also receive indirect information from M and P geniculate inputs via respective projections from layers 4α and 4β of V1. Because of these indirect connections, CO blobs are in a special position to integrate information from all three pathways of the LGN. The interblob regions receive indirect projections from the LGN M pathway via layer 3C, but in general, interblobs seem to receive more restricted information (Lachica et al., 1993). There are also numerous intrinsic connections across V1 layers (Casagrande, 1994a), but these projections are not discussed here. Given the numerous vertical connections within V1, the functional blob unit most likely spreads throughout all layers.

Previous research examining the distribution of VGluT2 in the cortex shows that VGluT2 is abundant throughout layer 4 of the primary visual cortex (Glendenning et al., 1976; Diamond et al., 1985; Wong and Kaas, 2010), and our results are consistent with this pattern, which strongly suggests that VGluT2 is associated with predominantly feed-forward or driving projections. These findings confirm that VGluT2 staining typically reveals glutamatergic geniculocortical and not corticocortical terminations (Kaneko and Fujiyama, 2002; Kaneko et al., 2002; Wong and Kaas, 2010; Balaram et al., 2013). Since all K-cell projections from the galago

LGN contain glutamate (Ding and Casagrande, 1998) and express VGluT2 messenger ribonucleic acid (mRNA) (Balaram et al., 2011), it makes sense that VGluT2 terminations form a patchy pattern in layer 3 of V1 that colocalize with K inputs to CO blobs. Given that VGluT2 connections identify feed-forward pathways, the VGluT2 input to blobs suggests that the K layers form driving projections as well. Since blobs in layer 3 also get input from sublayers of layer 4 in V1, these feed-forward inputs may contribute to some of the CO or VGluT2 reactivity found in blob structures.

Previous research concerning the relationship between CO and myelin has produced varied results, as there has been considerable debate over whether CO-dense blobs are densely or lightly myelinated. The results of myelin studies suggest that the patterns of myelin staining found in the visual cortex can vary according to the choice of technique. It was previously reported using Luxol fast blue that CO-dense blobs were densely myelinated (Tootell et al., 1983), but this led others to conclude that Luxol fast blue stains differently than the traditional Gallyas silver stain (Krubitzer and Kaas, 1989). In this study, though, it was apparent that the Gallyas pattern in V1 was related to the CO blob/interblob pattern (Horton and Hocking, 1997). Some evidence suggests that CO-light interblobs are more densely myelinated than the CO-dense blobs in squirrel monkeys (Krubitzer and Kaas, 1989) and galagos (Wong and Kaas, 2010). The present results indicate that the blobs do have a denser distribution of myelin than the surround, and this was revealed by the Gallyas silver procedure (Gallyas, 1979). The myelin-poor blob-like pattern could reflect a pattern in a cortical sublayer just above or below the CO blobs that was not revealed in the present study. However, the tissue examined in this study reveals myelin-dense blobs surrounded by myelin-poor interblobs in layer 3. While CO-dense blobs appear most prominently in layer 3B in galagos (and other primates), there is periodic weaker staining across

infragranular layers 5 and 6, as well as in the upper layers directly above the blobs (Horton, 1984).

There are several possible hypotheses for the coincidence of myelin-dense regions with CO blob regions in V1. First, as blobs and interblobs each have different specialized functions (Livingstone and Hubel, 1988), then the neurons sub-serving blob functions may require denser myelination than their surrounding interblob counterparts. Or, as a related hypothesis, the greater myelination of blobs could relate to the high levels of neuronal activity within blobs (Wong-Riley, 1994). Alternatively, the dense myelination found in blob regions in layer 3 could reflect the density of VGluT2 labeling from lateral geniculate inputs, as described in previous reports of blob and interblob projections in galagos (Florence and Casagrande, 1987; Lachica and Casagrande, 1992). Layer 4 of V1 also receives dense inputs from the lateral geniculate nucleus (Casagrande, 1994a) and shows dense myelin reactivity (Wong and Kaas, 2010), which again suggests that dense myelin labeling in layer 3 is related to the large quantity of afferent terminations in these structures. Further studies will undoubtedly reveal whether the dense myelination of CO blobs is related more to the afferent or efferent projections in these structures. For now, we can conclude that myelin-dense patches definitively align with VGluT2- and CO-dense blobs in V1 of galagos. It is also likely that myelin and VGluT2 identify CO blobs in V1 of other primates, including monkeys, apes, and humans.

REFERENCES

Balaram P, Hackett TA, Kaas JH (2013) Differential expression of vesicular glutamate transporters 1 and 2 may identify distinct modes of glutamatergic transmission in the macaque visual system. J Chem Neuroanat 50-51:21-38.

Balaram P, Takahata T, Kaas JH (2011) VGLUT2 mRNA and protein expression in the visual thalamus and midbrain of prosimian galagos (Otolemur garnetti). Eye Brain 2011:5-15.

Baldwin MK, Kaskan PM, Zhang B, Chino YM, Kaas JH (2012) Cortical and subcortical connections of V1 and V2 in early postnatal macaque monkeys. J Comp Neurol 520:544-569.

Bryant KL, Suwyn C, Reding KM, Smiley JF, Hackett TA, Preuss TM (2012) Evidence for ape and human specializations in geniculostriate projections from VGLUT2 immunohistochemistry. Brain Behav Evol 80:210-221.

Carey RG, Fitzpatrick D, Diamond IT (1979) Layer I of striate cortex of Tupaia glis and Galago senegalensis: projections from thalamus and claustrum revealed by retrograde transport of horseradish peroxidase. J Comp Neurol 186:393-437.

Carroll EW, Wong-Riley MT (1984) Quantitative light and electron microscopic analysis of cytochrome oxidase-rich zones in the striate cortex of the squirrel monkey. J Comp Neurol 222:1-17.

Casagrande V, De Bruyn E (1982) The galago visual system: aspects of normal organization and developmental plasticity. In: Lesser Bushbaby as an Animal Model (Haines, D., ed), pp 107-135 Boca Raton (FL): CRC.

Casagrande V, Khaytin I, Boyd J (2006) The evolution of parallel visual pathways in the brains of primates. In: Evolution of Nervous Systems (Preuss, T. and Kaas, J., eds), pp 87-108 Waltham (MA): Academic Press.

Casagrande VA (1994a) The afferent, intrinsic, and efferent connections of primary visual cortex in primates. In: Cerebral Cortex (Peters, A. and Rockland, K. S., eds), pp 201-259 New York: Plenum.

Casagrande VA (1994b) A third parallel visual pathway to primate area V1. Trends Neurosci 17:305-310.

Casagrande VA, Yazar F, Jones KD, Ding Y (2007) The morphology of the koniocellular axon pathway in the macaque monkey. Cereb Cortex 17:2334-2345.

Condo GJ, Casagrande VA (1990) Organization of cytochrome oxidase staining in the visual cortex of nocturnal primates (Galago crassicaudatus and Galago senegalensis): I. Adult patterns. J Comp Neurol 293:632-645.

Diamond IT, Conley M, Itoh K, Fitzpatrick D (1985) Laminar organization of geniculocortical projections in Galago senegalensis and Aotus trivirgatus. J Comp Neurol 242:584-610.

Ding Y, Casagrande VA (1997) The distribution and morphology of LGN K pathway axons within the layers and CO blobs of owl monkey V1. Vis Neurosci 14:691-704.

Ding Y, Casagrande VA (1998) Synaptic and neurochemical characterization of parallel pathways to the cytochrome oxidase blobs of primate visual cortex. J Comp Neurol 391:429-443.

Economides JR, Sincich LC, Adams DL, Horton JC (2011) Orientation tuning of cytochrome oxidase patches in macaque primary visual cortex. Nat Neurosci 14:1574-1580.

Felleman DJ (2008) Functional maps in visual cortex: topographic, modular, and column organizations. In: The Senses (Masland, R. and Albright, T., eds), pp 577-593 London: Elsevier.

Florence SL, Casagrande VA (1987) Organization of individual afferent axons in layer IV of striate cortex in a primate. J Neurosci 7:3850-3868.

Florence SL, Casagrande VA (1990) Development of geniculocortical axon arbors in a primate. Vis Neurosci 5:291-309.

Florence SL, Sesma MA, Casagrande VA (1983) Morphology of geniculo-striate afferents in a prosimian primate. Brain Res 270:127-130.

Gallyas F (1979) Silver staining of myelin by means of physical development. Neurol Res 1:203-209.

Garcia-Marin V, Ahmed TH, Afzal YC, Hawken MJ (2013) Distribution of vesicular glutamate transporter 2 (VGluT2) in the primary visual cortex of the macaque and human. J Comp Neurol 521:130-151.

Glendenning KK, Kofron EA, Diamond IT (1976) Laminar organization of projections of the lateral geniculate nucleus to the striate crotex in Galago. Brain Res 105:538-546.

Goodchild AK, Martin PR (1998) The distribution of calcium-binding proteins in the lateral geniculate nucleus and visual cortex of a New World monkey, the marmoset, Callithrix jacchus. Vis Neurosci 15:625-642.

Hendrickson AE (1985) Dots, stripes and columns in monkey visual cortex. Trends Neurosci 8:406-410.

Hendry SH, Yoshioka T (1994) A neurochemically distinct third channel in the macaque dorsal lateral geniculate nucleus. Science 264:575-577.

Horton JC (1984) Cytochrome oxidase patches: a new cytoarchitectonic feature of monkey visual cortex. Philos Trans R Soc Lond B Biol Sci 304:199-253.

Horton JC, Hocking DR (1997) Myelin patterns in V1 and V2 of normal and monocularly enucleated monkeys. Cereb Cortex 7:166-177.

Horton JC, Hubel DH (1981) Regular patchy distribution of cytochrome oxidase staining in primary visual cortex of macaque monkey. Nature 292:762-764.

Jacobs GH, Neitz M, Neitz J (1996) Mutations in S-cone pigment genes and the absence of colour vision in two species of nocturnal primate. Proc Biol Sci 263:705-710.

Johnson JK, Casagrande VA (1995) Distribution of calcium-binding proteins within the parallel visual pathways of a primate (Galago crassicaudatus). J Comp Neurol 356:238-260.

Jones EG, Hendry SH (1989) Differential Calcium Binding Protein Immunoreactivity Distinguishes Classes of Relay Neurons in Monkey Thalamic Nuclei. Eur J Neurosci 1:222-246.

Kaas JH (2012) Evolution of columns, modules, and domains in the neocortex of primates. Proc Natl Acad Sci U S A 109 Suppl 1:10655-10660.

Kaas JH, Huerta MF, Weber JT, Harting JK (1978) Patterns of retinal terminations and laminar organization of the lateral geniculate nucleus of primates. J Comp Neurol 182:517-553.

Kaneko T, Fujiyama F (2002) Complementary distribution of vesicular glutamate transporters in the central nervous system. Neurosci Res 42:243-250.

Kaneko T, Fujiyama F, Hioki H (2002) Immunohistochemical localization of candidates for vesicular glutamate transporters in the rat brain. J Comp Neurol 444:39-62.

Krubitzer LA, Kaas JH (1989) Cortical integration of parallel pathways in the visual system of primates. Brain Res 478:161-165.

Lachica EA, Beck PD, Casagrande VA (1993) Intrinsic connections of layer III of striate cortex in squirrel monkey and bush baby: correlations with patterns of cytochrome oxidase. J Comp Neurol 329:163-187.

Lachica EA, Casagrande VA (1992) Direct W-like geniculate projections to the cytochrome oxidase (CO) blobs in primate visual cortex: axon morphology. J Comp Neurol 319:141-158.

Livingstone M, Hubel D (1988) Segregation of form, color, movement, and depth: anatomy, physiology, and perception. Science 240:740-749.

Livingstone MS, Hubel DH (1982) Thalamic inputs to cytochrome oxidase-rich regions in monkey visual cortex. Proc Natl Acad Sci U S A 79:6098-6101.

Livingstone MS, Hubel DH (1984) Anatomy and physiology of a color system in the primate visual cortex. J Neurosci 4:309-356.

Livingstone MS, Hubel DH (1987) Connections between layer 4B of area 17 and the thick cytochrome oxidase stripes of area 18 in the squirrel monkey. J Neurosci 7:3371-3377.

Lu HD, Roe AW (2008) Functional organization of color domains in V1 and V2 of macaque monkey revealed by optical imaging. Cereb Cortex 18:516-533.

Murphy KM, Jones DG, Van Sluyters RC (1995) Cytochrome-oxidase blobs in cat primary visual cortex. J Neurosci 15:4196-4208.

Preuss TM, Beck PD, Kaas JH (1993) Areal, modular, and connectional organization of visual cortex in a prosimian primate, the slow loris (Nycticebus coucang). Brain Behav Evol 42:321-335.

Preuss TM, Kaas JH (1996) Cytochrome oxidase 'blobs' and other characteristics of primary visual cortex in a lemuroid primate, Cheirogaleus medius. Brain Behav Evol 47:103-112.

Tootell RB, Silverman MS, De Valois RL, Jacobs GH (1983) Functional organization of the second cortical visual area in primates. Science 220:737-739.

Wikler KC, Rakic P (1990) Distribution of photoreceptor subtypes in the retina of diurnal and nocturnal primates. J Neurosci 10:3390-3401.

Wong-Riley M (1979) Changes in the visual system of monocularly sutured or enucleated cats demonstrable with cytochrome oxidase histochemistry. Brain Res 171:11-28.

Wong-Riley M (1994) Primate visual cortex: dynamic metabolic organization and plasticity revealed by cytochrome oxidase. In: Cerebral Cortex, vol. 10 (Peters, A. and Rockland, K. S., eds), pp 141-200 New York: Plenum.

Wong-Riley MT (1989) Cytochrome oxidase: an endogenous metabolic marker for neuronal activity. Trends Neurosci 12:94-101.

Wong P, Kaas JH (2010) Architectonic subdivisions of neocortex in the Galago (Otolemur garnetti). Anat Rec (Hoboken) 293:1033-1069.